Used Fuel Degradation: Experimental and Modeling Report

Fuel Cycle Research & Development

(FCRD-UFD-2013-000404)

Prepared for
U.S. Department of Energy
Used Fuel Disposition Campaign

David C. Sassani, Carlos F. Jové Colón, Philippe Weck
(Sandia National Laboratories)

James L. Jerden Jr., Kurt E. Frey, Terry Cruse, William L. Ebert (Argonne National Laboratory)

Edgar C. Buck, Richard S. Wittman
(Pacific Northwest National Laboratory)

October 17, 2013

SAND2013- 9077P

Prepared by:

Sandia National Laboratories

Albuquerque, New Mexico 87185

U.S. DEPARTMENT OF ENERGY

Sandia National Laboratories

Revision 2
12/20/2012

APPENDIX E
FCT DOCUMENT COVER SHEET [1]

Name/Title of Deliverable/Milestone/Revision No.	Used Fuel Degradation: Experimental and Modeling Report (M2FT-13SN0806062)
Work Package Title and Number	DR Generic Engineered Barrier System Evaluations – SNL, FT-13SN080606
Work Package WBS Number	1.02.08.06
Responsible Work Package Manager	Carlos F. Jove Colon (Name/Signature)

Date Submitted: 10/17/2013

Quality Rigor Level for Deliverable/Milestone[2]	☒ QRL-3	☐ QRL-2	☐ QRL-1 Nuclear Data	☐ Lab/Participant QA Program (no additional FCT QA requirements)

This deliverable was prepared in accordance with   Sandia National Laboratories
                                                                              (Participant/National Laboratory Name)

QA program which meets the requirements of
    ☒ DOE Order 414.1   ☐ NQA-1-2000   ☐ Other

This Deliverable was subjected to:

☐ Technical Review	☐ Peer Review
Technical Review (TR)	**Peer Review (PR)**
Review Documentation Provided	**Review Documentation Provided**
☐ Signed TR Report or,	☐ Signed PR Report or,
☐ Signed TR Concurrence Sheet or,	☐ Signed PR Concurrence Sheet or,
☒ Signature of TR Reviewer(s) below	☐ Signature of PR Reviewer(s) below

Name and Signature of Reviewers
Yifeng Wang

NOTE 1: *Appendix E should be filled out and submitted with the deliverable. Or, if the PICS:NE system permits, completely enter all applicable information in the PICS:NE Deliverable Form. The requirement is to ensure that all applicable information is entered either in the PICS:NE system or by using the FCT Document Cover Sheet.*

NOTE 2: *In some cases there may be a milestone where an item is being fabricated, maintenance is being performed on a facility, or a document is being issued through a formal document control process where it specifically calls out a formal review of the document. In these cases, documentation (e.g., inspection report, maintenance request, work planning package documentation or the documented review of the issued document through the document control process) of the completion of the activity, along with the Document Cover Sheet, is sufficient to demonstrate achieving the milestone. If QRL 1, 2, or 3 is not assigned, then the Lab / Participant QA Program (no additional FCT QA requirements) box must be checked, and the work is understood to be performed and any deliverable developed in conformance with the respective National Laboratory / Participant, DOE or NNSA-approved QA Program.*

AKNOWLEDGEMENTS

SUMMARY

The contributions presented in this report are being accomplished via a concerted effort among three different national laboratories: SNL, ANL and PNNL. This collaborative approach to the used fuel degradation and radionuclide mobilization (UFD&RM) activities includes experimental work, process model development (including first-principles approaches) and model integration—both internally among developed process models and between developed process models and PA models. Figure S-1 depicts a summary schematic of the major models, experimental studies, and their primary handoffs to each other, as well as the major outputs that currently would feed performance assessment (PA) models as a result of the integrated execution of this work.

The primary outputs of these cumulative UFD&RM activities provide two connections into the PA models. The primary output connection is the fractional degradation rate (FDR) of the used fuel matrix. Within the current PA models, this parameter is sampled from a distribution of reported values in the literature, but may now be generated directly from these process-based models (both the radiolysis model and the mixed potential model are used to evaluate this result). In addition, a second output has been generated to represent the instant release fractions (IRF) of radionuclides that are released virtually instantaneously upon breach of the cladding. As indicated in Figure S-1, two sets of distributions are recommended, a set of uniform distributions that are parameterized as a function of burnup and a set of triangular distributions that have no functional dependencies. Both of these sets of IRF distributions capture uncertainties in their parameterization. Sampling of these IRF distributions can be done directly within the PA model at the initial time of UF degradation for each fuel rod represented as having a breach in its cladding.

Within the process models, the radiolysis model (RM) and the mixed potential model (MPM) may be used separately to evaluate (a) the generation rate of radiolytic oxidants in a water film on the surface of a used fuel pellet, and (b) the degradation rate of used fuel at the pellet-water film interface for a given generation rate of radiolytic oxidant, respectively. In addition, these two model tools can be used to evaluate the degradation of used fuel of a given burnup under post-closure conditions where decay and thermal evolution occur. These two models operate on very different time scales. The RM evaluates multiple coupled reactions that occur in miniscule fractions of a second and that reach steady state in minutes to hours. The MPM generally evaluates timesteps of months to years to hundreds of years. The feedback between these two models has been implemented by hand to this point, but progress has been made in developing detailed coupling strategies for merging these two process models into a single coupled module.

Underpinning these continuum modeling approaches are experimental studies and first principles models of uranium dioxide and the major corrosion products expected. As well as providing conceptual guidance to the modeling approaches, the experimental programs at both ANL and PNNL have provided validation data for the conceptual models and parametric constraints for improving the modeling tools. Detailed mechanistic processes have also been investigated using first principles molecular scale modeling for UO_2 and some of its common corrosion products. Such work also provides methods for predicting thermochemical properties where data are lacking, and can provide insight and validation for processes evaluated in detailed electrochemical experiments where multiple mechanisms are all possible.
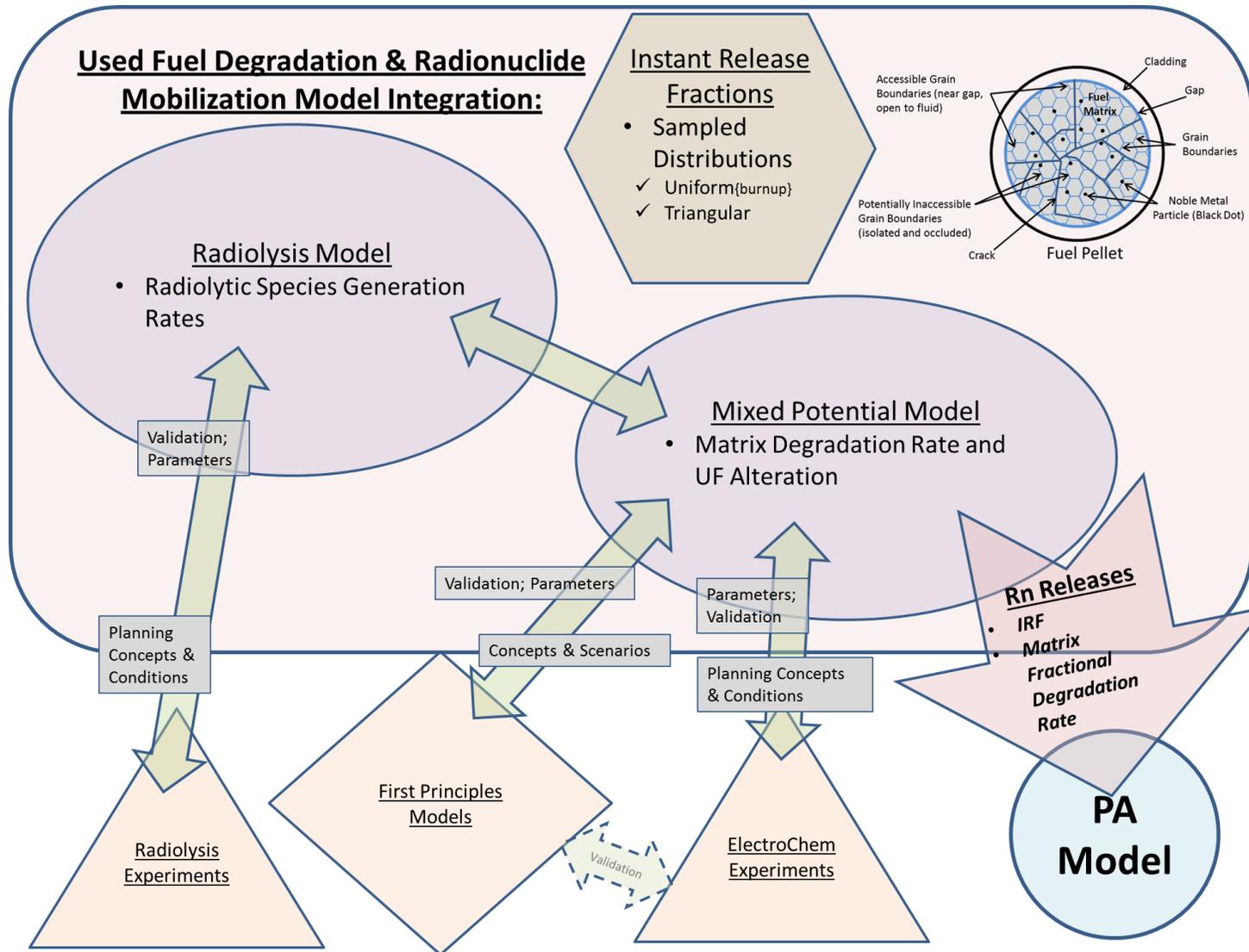
Figure ES-1. Schematic diagram of the integration among activities for used fuel degradation and the connection to a performance assessment model. Experimental work (triangles) and first principles models (diamond) shown as underpinning process models.

The main accomplishments of these activities are summarized as follows:

- Developed an idealized strategy for integrating used fuel degradation process models with PA models to analyze generic disposal environments. This strategy includes parametric connections/couplings needed for direct incorporation into PA models (Section 1.2.2). However, it is an ongoing task to delineate in the implementation specifics of how these process models will couple to other EBS process submodels within the PA model for generic disposal environment evaluations of a safety case. Additional more simplified coupling options are outlined that have fewer open constraints on implementation specifics and provide flexible options for incorporating additional coupling detail as needed.

- Delineated constraints for the instant release fractions (IRF –Section 1) from used nuclear fuel. The constraints are implemented in two sets of distributions: (a) triangular distributions representing minimum, maximum, and mean (apex) values for LWR UF with BU at or below 50 MWd/KgU, and (b) uniform distributions as a function of BU representing instantaneous radionuclide releases for UF with BU up to 75 MWd/KgU. In future work, additional data may allow delineation of the accessible grain boundaries (and pellet fractures) from inaccessible grain boundaries (and pellet fractures) to better delineate constraints on the IRF. Currently, all grain boundaries (and pellet fractures) are considered accessible.

- Developed and implemented a radiolysis model (RM - Section 2) using a comprehensive set of coupled radiolysis kinetic reactions to better account for potential solution compositions to be encountered in repository environments (Wittman and Buck, 2012). Radiolytic species are generated at a rate that is based on the dose rate induced by the used fuel radiation field deposited in the water film on the fuel pellet. The current model covers the H_2O system and allows for dissolved carbonate by considering heterogeneous $CO_{2\ (aq)}$ speciation including HCO^-_3. Comparisons of modeling results are in good agreement with those reported in other studies. The model inputs are the reaction rate constants, the temperature and dose rate, the generation rates of radiolytic species, and the initial concentrations of species in the system. In these idealized systems, hydrogen peroxide is the primary oxidizing species generated in the radiolytic process. The conditional generation rate for H_2O_2 production is the primary output provided to the model for matrix degradation rate (i.e., the mixed potential model).

- Implemented and verified/validated the Canadian mixed potential model for UO_2 fuel corrosion in the initial mixed potential model (MPM - Jerden et al., 2013). The objective of the MPM (Section 3) is to calculate the used fuel degradation rates for a wide range of disposal environments to provide the source term radionuclide release rates for generic repository concepts. The fuel degradation rate is calculated for chemical and oxidative dissolution mechanisms using mixed potential theory to account for all relevant redox reactions at the fuel surface, including those involving oxidants produced by solution radiolysis. This MPM is based on the fundamental electrochemical and thermodynamic properties described by interactions at the fuel – fluid interface and captures key processes such as hydrogen oxidation and the catalysis of oxidation/reduction reactions by noble metal (epsilon) particles on the fuel surface. If

radiolytic oxidants are exhausted by reaction with hydrogen in the EBS (e.g., supplied from corrosion processes), then the degradation rate becomes controlled by UO_2 solubility constraints (chemical dissolution) and the degradation rate is affected directly by the rate of transport of uranium away from the used fuel. If oxidative dissolution is the dominant process, then the MPM directly calculates the rate of used fuel matrix degradation. Jerden et al. (2013) provides an archived version of Rev 01 of the MPM. Additional computational capability to address the role of epsilon particles in reducing radiolytic oxidants is added to the current version (Section 7). The MPM was developed to account for the following key phenomena (Jerden et al. 2013):

- o Rate of oxidative dissolution of the fuel matrix as determined by interfacial redox reaction kinetics (quantified as corrosion potential) occurring at the multiphase fuel surface (phases include UO_2 and the fission product alloy or epsilon phase).
- o Chemical (or solubility-based) dissolution of the fuel matrix.
- o Complexation of dissolved uranium by carbonate near the fuel surface and in the bulk solution.
- o Production of hydrogen peroxide (the dominant fuel oxidant in anoxic repository environments) by alpha-radiolysis.
- o Diffusion of reactants and products in the groundwater away from and towards the reacting fuel surface.
- o Precipitation and dissolution of a U–bearing corrosion product layer on the fuel surface.
- o Diffusion of reactants and products through the porous and tortuous corrosion layer covering the reacting fuel surface.
- o Arrhenius-type temperature dependence for all interfacial and bulk reactions.

- Advanced strategies for coupling the RM and MPM into a single fuel matrix degradation (FMD) module (Section 4) for use in analyzing the matrix degradation rate (fractional and absolute) of used fuel. Parameters needed to couple the codes and four strategies for implementing the coupling of the two process models are described in detail (Section 4). Different options have advantages and disadvantages based on the extent of coding that would be required and the ease of use of the final product. The four approaches for implementing coupling are:

  - o Option 1: Add radiolysis model as subroutine within mixed potential model code. This would involve re-coding the RM from Fortran into MATLAB or alternatively recoding the MPM into Fortran so that the two models would run as part of the same program.

    - Pros: full RM code included in integrated model, not limited to abstracted form of the RM, seamless transfer of information.

    - Cons: relatively large amount of time and effort required to support recoding.

  - o Option 2: Represent radiolysis model as an analytical expression within mixed potential model code. This would involve minimal coding in MATLAB, but would require significant effort to define an analytical form that captures the full range of conditional dependencies accounted for in the RM.

- Pros: coding work is streamlined and simplified, seamless transfer of information.

- Cons: uncertainty of success of approach, it is not clear that a single analytical expression can capture all of the relevant conditional dependencies accounted for in the full RM.

  o Option 3: Provide radiolysis model results as look-up table of conditional generation values produced by running the RM over the full range of relevant conditions. This generation value look-up table would be treated by the MPM as part of the parameter database.

  - Pros: little to no coding work needed, seamless transfer of information.

  - Cons: relatively large amount of time and effort to produce exhaustive table that considers all relevant conditions,

  o Option 4: Maintain radiolysis model and mixed potential model as separate codes that call each other during a fuel degradation model run.

  - Pros: little to no coding work needed, not limited to abstracted version of the RM.

  - Cons: uncertainty of success of approach, it is not clear that the Fortran and MATLAB codes and pass the needed information back and forth as they currently exist. Even if possible this approach may dramatically increase computing time needed to run the FDM.

  The last of these four options is closest to the approach to the sensitivity analyses for the MPM implemented within DAKOTA presented in Section 4.3.1. However, integration of the RM into this implementation has not been completed at this point and would require either a dynamic link library to implement, or additional coding within the DAKOTA environment to manage parameter hand-offs between the MPM and RM.

- Completed computational first-principles studies of the structures of the uranyl peroxide hydrates studtite and metastudtite (Weck et al., 2012) and of the bulk and surface chemistry of UO_2 (Weck et al., 2013). The structures of the uranyl peroxide hydrates obtained from total energy calculations using density functional theory are in very good agreement with those characterized by experimental X-ray diffraction methods. Such work tests this computational tool to predict thermodynamic properties of fuel corrosion products (e.g., uranyl peroxide hydrates) for used with similar studies of UO_2 bulk and surface chemistry (Weck et al., 2013).

Conclusions and future development

Our general strategy for integrating process models with each other, and within the performance assessment models, is to identify initially the major feeds among the process models (Section 4) and from the process models to performance assessment models (Section 1). For coupling into performance assessment models, our approach begins by using the existing interface connections in the PA model and progresses to adding further connections as the process models develop and become more highly coupled. The ultimate objective is to support the PA models with a single coupled process model for analyzing the fractional

degradation rate of used fuel. Note that even after coupling, the radiolysis model (RM) and the mixed potential model (MPM) can still be used individually for detailed sensitivity and uncertainty analyses as well.

Currently, the MPM has been coupled with DAKOTA to perform parametric sensitivity analyses for major input variables such as radiation flux, temperature, and chemical species variability. The DAKOTA code provides one possible means of handshaking or coupling the MPM with the RM. Within any coupling implementation, identifying the essential parameters to be exchanged is the primary step. One of these is the conditional generation rate of hydrogen peroxide (G_{cond}) as a function of energy deposition in the water film on the used fuel pellet surface. The value of G_{cond} is calculated in the RM and handed off to the MPM. Within the MPM, the G_{cond} is used to calculate the spatial generation of [H_2O_2] from the dose rate as affected by surface reactions with the fuel and diffusive flux of the species.

The coupling of the RM and MPM is implemented currently by running the models separately because the MPM uses time steps on the order of years, whereas the RM uses time steps on the order of seconds. An alternative to actively linking the RM and MPM (perhaps within DAKOTA) is to develop an analytic expression that determines G_{cond} for a given set of conditions. The analytic expression could be coded directly into the MPM via the MATLAB implementation, and thus run directly within the MPM. However, this simplification does not establish a true working link and the full capabilities of RM would be lost without further work. Furthermore, the determination of analytical expressions for the full ranges of environments may prove to be onerous.

Currently the only radiolytic species in the MPM is H_2O_2. Other radiolytic species will need to be added to the MPM for it to be applicable to the full range of relevant geologic and EBS environments. The radiolytic species that need to be added can be determined by sensitivity runs using the RM (which evaluates a more detailed set of compositional components) for the range of relevant solution compositions for sites of interest. The focus of RM sensitivity runs is on radiolytically active species (for example: Cl^-, Br^-, NO_3^-, CO_3^{2-}, SO_4^{2-}) and can be used to determine concentration thresholds above which radiolytic species other than H_2O_2 significantly impact fuel oxidation.

Density functional theory (DFT) calculations of the thermodynamic properties of crystalline studtite, $(UO_2)O_2(H_2O)_4$, and metastudtite, $(UO_2)O_2(H_2O)_2$, were carried out within the generalized gradient approximation to derive both their isochoric and isobaric thermal properties. Further experimental work is needed to assess our theoretical predictions for these SNF corrosion phases. This methodology will be applied in a systematic way to other possible metastable corrosion phases and other NS and EBS models to expand the applicability of this data set to more realistic systems. In addition, polymorphism in stoichiometric dehydrated schoepite, $UO_2(OH)_2$, was investigated using computational approaches that go beyond standard DFT. The results show that standard DFT is sufficient for this system. The three $UO_2(OH)_2$ phase structures optimized with standard DFT will be used in future calculations of the thermodynamic stability and phase transitions in this compound.

For the UFD&RM process models and/or coupled modules, the primary connection into the performance assessment models is the fractional degradation rate (FDR) parameter, which is currently sampled from a distribution. This primary connection has been the focus for developing more process-based models that are able to supplant the FDR distribution by supplying that

parameter directly as a result of the process model. In addition, a second connection within the PA model could be generated to represent the instant release fractions. Sampling of the IRF distributions within the PA model would be done similar to the current sampling of the FDR distribution and would describe the fast/instant release fraction radionuclides that are mobilized instantly at the time of cladding breach. The distributions for the IRF would only need to be sampled at the initiation of UF degradation for each fuel rod represented as having a breach in its cladding.

TABLE OF CONTENTS

FIGURES

TABLES

ACRONYMS AND ABBREVIATIONS

ANL	Argonne National Laboratory
ATM	Approved Testing Material
CV	Cyclic Voltammetry
DOE	Department of Energy (US DOE)
DR	Dissolution rate
EBS	Engineered Barrier System
EC	European Commission
EIS	Electrochemical Impedance Spectroscopy
FACSIMILE	A computer program for modeling the kinetics of chemical systems
FEPs	Features, events, and processes
FCRD	Fuel Cycle Research and Development
FCT	Fuel Cycle Technology
FDR	Fractional Degradation Rate
FGR	Fission gas release
FIRST	Fast / Instant Release of Safety Relevant Radionuclides (EC project)
HBS	High burnup structure
HLW	High Level Waste
IRF	Instant release fraction
IRM	Instant Release Model
LWR	Light water reactor
LPR	Linear Polarization Resistance
MOX	Mixed oxide fuel (e.g., U and Pu oxides)
MPM	Mixed potential model
NMP	Noble Metal Particle
NS	Natural System
OC	Open Circuit Corrosion
PA	Performance assessment
PD	Potentiodynamic
PNNL	Pacific Northwest National Laboratory
PS	Potentiostatic
PWR	Pressurized water reactor

R&D	Research and Development
RADFUEL	Radiolytically-aged doped (RAD) synthetic nuclear fuels
RN	Radionuclide
RM	Radionuclide mobilization
ROK	Republic of Korea

S_A	Surface area (m^2)
SA	Safety Assessment
SEM	Scanning Electron Microscopy
SNF	Spent Nuclear Fuel
SNL	Sandia National Laboratories

THCM	Thermal-hydrologic-chemical-mechanical (processes)

UF	Used Fuel
UNF	Used Nuclear Fuel
UFD	Used Fuel Disposition
UFDC	Used Fuel Disposition Campaign
UOX	Uranium oxide fuel

WP	Work package

MINERAL NAMES AND CHEMICAL FORMULAE

Meta-schoepite $[(UO_2)_4O(OH)_6](H_2O)_5$
Meta-studtite $UO_4 \cdot 2H_2O$
Schoepite $[(UO_2)_8O_2(OH)_{12}](H_2O)_{12}$
Studtite $[(UO_2)O_2(H_2O)_2](H_2O)_2$

UNITS

μm	micrometer
g	grams
Gy	Grays (100 Rads)
Kg	kilograms
Kg	kilograms uranium
M	molarity, mole/liter
Mbq	millibequerels
mg	milligram
MTU	Metric ton uranium
MWd	megawatt-days

1.   MODEL OVERVIEW AND INTEGRATION

1.1   Introduction

Within the Used Fuel Disposition Campaign (UFDC) of the United States Department of Energy Office of Nuclear Energy (DOE-NE), we have investigated used fuel (UF) degradation and radionuclide mobilization (UFD&RM) and implemented/produced a set of models encompassing radiolytic processes, UF matrix degradation, instant release fractions (IRF) of key radionuclides, and first-principles atomistic models for UO_2 and its potential corrosion products. The goals of this collaborative effort (among three different national laboratories: Argonne National Laboratory [ANL]; Pacific Northwest National Laboratory [PNNL]; and Sandia National Laboratories [SNL]) are to enhance the understanding of UF degradation processes and the technical bases for safety analyses in a range of generic disposal environments. In addition to these modeling efforts, integrated experimental studies are being conducted at both ANL and PNNL to evaluate and validate (and ultimately expand) process models for radiolytic phenomena and UF matrix degradation in various geologic disposal conditions. Integration/coupling of these process models into performance assessment models is one focus of SNL efforts within the generic analyses of the Engineered Barrier System (EBS) for various repository environments. As discussed below, the present work has produced a set of models for evaluation of used fuel degradation as an initial step towards an enhanced coupled model of source-term processes.

1.1.1   Coupling the Mixed Potential and Radiolysis Models for Used Fuel Degradation

The primary purpose of this report is to describe the strategy for coupling three process level models to produce an integrated Used Fuel Degradation Model (FDM). The FDM, which is based on fundamental chemical and physical principals, provides direct calculation of radionuclide source terms for use in repository performance assessments. The matrix degradation model is used to calculate UO_2 degradation rates by chemical and oxidative dissolution mechanism based on electrochemical theory in the mixed potential model (MPM) (Jerden et al. 2013). The radiolysis model (RM) is used to calculate steady state concentrations of radiolytic species (Wittman and Buck, 2012) that participate in redox reactions modeled in the matrix degradation model. The FDM source term includes radionuclides released from gap and grain boundaries as quantified using an instantaneous release model (IRM) (Sassani et al. 2012). The programmatic context for the work described in this report is shown in Figure 1.1. The FDM uses input properties of the fuel waste forms and disposal environment to calculate the rate of fuel degradation as the conditions at the fuel surface evolve over time. Radionuclides in the fuel are mobilized at the same rate and made available for transport away from the waste package. The FDM model provides the source term concentrations for radionuclides used in reactive transport models of the disposal system.

Engineered Barrier System (EBS)		Geosphere	Biosphere
Waste Form: Used Oxide Fuel	Waste Package / EBS Buffer (e.g., backfill, liner, seals)	Host Rock and Other Geologic Units	Surface and Biosphere
Coupled Thermal-Hydrologic-Chemical-Mechanical-Biological-Radiological Processes			
Waste Form Degradation, Radionuclide Release / *Radionuclide Transport*			
Source Term	EBS Environment	Geosphere Environment	Biosphere Environment and Dose Factors

Figure 1.1. Components of a generic disposal system for used oxide fuel (adapted from Freeze et al. 2010). The red circle identifies the processes covered by the models described in this report.

Additionally, an overview of the strategy for incorporating the FDM into performance assessment models is also described in this first section. The strategy is given as part of the of the model development in each area given as context summarizing the connections among all the modeling activities.

1.2 Background and Overview of Models

The Used Fuel Disposition Campaign (UFDC) supports the Fuel Cycle Technology (FCT) Program established by the United States Department of Energy Office of Nuclear Energy (DOE-NE). The mission of the UFDC is to identify alternatives and conduct scientific research and technology development to enable storage, transportation and disposal of used fuel (UF) and wastes generated by existing and future nuclear fuel cycles. This article covers research activities on engineered barrier system (EBS) model development in the UF degradation and radionuclide mobilization (UFD&RM) activities in support of the generic EBS analyses, tool development, and model integration into performance assessment (PA) model (Sassani et al., 2012).

Currently, performance models for four generic disposal environments (i.e., repositories in salt, granite, and clay/shale, and deep borehole disposal in various media) include constraints on radionuclide release from UF based on sampled distributions for the general ranges of fractional degradation rates taken from the literature. These generic models further constrain radionuclide mobilization away from the UF using published solubility-limited radionuclide concentrations for those radioelements expected to be reprecipitated under local conditions within the EBS. The potential instant release fractions (IRF) of key radionuclides have not been directly incorporated into these four generic approaches, which are currently being subsumed into performance assessment models.

For the next stage of performance assessment (PA) model development, the current UFD&RM work provides process-model-based fractional degradation rates for UF that account more directly for the effects of the major chemical variables in the source-term model (Sassani et al., 2012). Investigating UFD&RM has led to implementation of process models for (a) UF matrix degradation rates (the Mixed Potential Model - MPM) and (b) UF radiolytic processes and the major radiolytic species production (the Radiolysis Model – RM). In addition, constraints for the IRF of key radionuclides have been provided for use in PA, and first-principles atomistic models for UO_2 and its potential corrosion products have been developed. The MPM and the RM are to be coupled for use within performance assessment model evaluations of the source term in the post-closure environment. Implementation of these process models into performance assessment models facilitates enhanced coupling to chemical variables, and expected thermal and pressure variations, as well as more explicit treatment of phase evolution. Moreover, two sets of distributions providing constraints for the fast/instant release fraction of radioelements (Cs, I, Tc, Sr, C and Cl) based on literature values are provided for sampling within the performance assessment models. Furthermore, first-principles models for the bulk chemical properties and surface chemistry of UO_2, as well as for the structures of studtite and metastudtite, provide a rigorous methodology for evaluating/validating continuum scale models of UF degradation, and facilitate the enhanced mechanistic analysis of processes governing fuel degradation.

1.2.1   Used Fuel degradation processes within the engineered barrier system

The generic EBS analyses (Jové Colón et al., 2012) entail the evaluation, tool development, and integration with performance assessment models, including the study of used nuclear fuel degradation. The latter ultimately determines calculated radionuclide releases beyond the confines of the nuclear fuel and waste container. Integration of EBS models with performance assessment models is an effort that evolves in parallel with PA and safety assessments (SA), and repository barrier processes (and sub-processes) model development. More advanced analysis of generic disposal concepts requires the accurate understanding of processes leading to radionuclide releases from the EBS, specifically at the barrier interface between fuel assemblies and containment structures. Multilayered EBS concepts and related materials evaluated by the UFDC seek to provide the necessary level of confidence to ensure safe and robust long-term waste isolation.

However, it is sensible to anticipate that waste containment failure would affect some canisters, therefore exposing fuel to interactions with subsurface fluids and eventually leading to radionuclide release. Given the importance of such processes to long-term disposal system performance, the main objectives (Sassani et al., 2012) of the FY2013 UFD&RM effort are:

- Data analysis and generation of statistical distributions to represent the IRF of radionuclides from the nuclear fuel.

- Implementation/development of a rigorous and comprehensive RM to evaluate the $U-H_2O-CO_2$ system (expanding to other chemical components as needed, e.g., Cl for salt systems).

- Implementation/development of a predictive model capability for used nuclear fuel matrix degradation rates based on electrochemical and thermodynamic principles (i.e., the mixed potential model, or MPM).

- Use of computational methods and approaches based on first principles to study the structures of uranium-bearing oxides and their degradation products (Weck et al., 2012; 2013).

- Strategy for coupling the RM and MPM into used fuel degradation model (FDM) and preliminary development of an integrated framework strategy for passing information between EBS process models and the performance assessment models (Sassani et al.,. 2012; 2013).

1.2.1.1   *Engineered Barrier System Interfaces*

The generic evaluation of EBS performance in geologic repositories requires an all-inclusive analysis of key processes (and sub-processes) affecting the isolation capacity of engineered barrier domains emplaced within the considered host media. Jové-Colón et al. (2012) described the importance of the analysis of Thermal-Hydrological-Mechanical-Chemical processes common to different EBS design concepts for various materials, local environment, and specific interactions as illustrated in Figure 1.2. Also depicted in this figure are the connections from UF degradation and radionuclide mobilization (UFD&RM) processes to the EBS. Used fuel degradation represents a set of coupled processes defined mainly by interactions between nuclear fuel and fluids in the EBS that ultimately provides the radionuclide source-term.

It should be noted that fuel cladding is currently treated as the interface between the UFD&RM and EBS. The task of integrating process models to describe cladding evolution/degradation with those of the UF degradation will be a growing focus of the UFD&RM tasks once the current models are integrated into performance assessment models. A summary report (Sassani, 2011) provided an overview of the modeling and experimental tasks for FY2011 in UFD&RM and outlined the goals of this work for FY2012. A more recent report (Sassani et al., 2013) describes the current model implementations and provides a conceptual framework for coupling and integration of those models within the performance assessment models. The major conceptual approach for these modeling efforts is described in the next section.
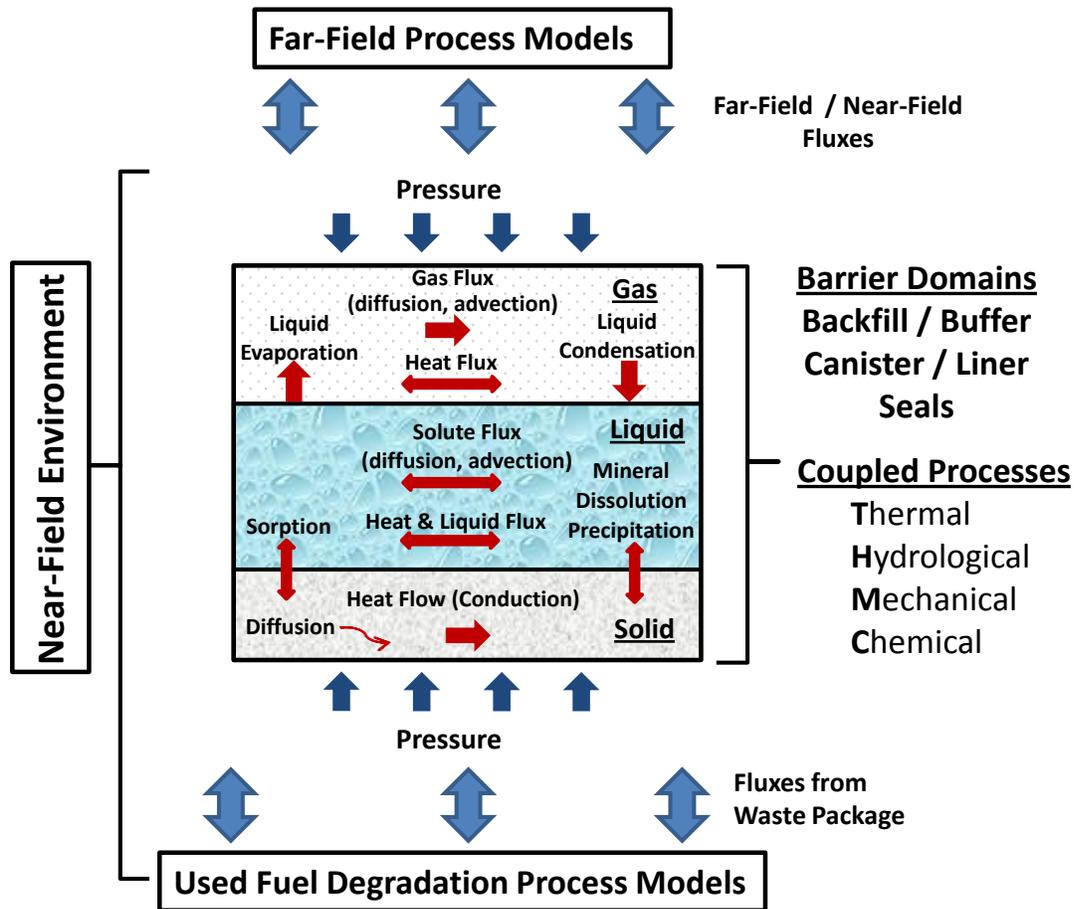
Figure 1.2. EBS coupled process phenomena (center) and interrelations between process models from other domains (from Fig. 1.1-1 in Sassani et al., 2012).

1.2.2   Used Fuel Degradation and Radionuclide Mobilization Concepts and Models

Once the cladding around UF is breached in a failed waste package, the UF will be exposed to ingress of water and/or humid air. The radionuclide mobilization from such exposed UF can depend on the type of cladding breach and on the progression of cladding degradation following the initial cladding breach. Several hypothetical scenarios for the evolution of the state of a fuel rod following breach of its cladding are plausible. In one case, the corrosion of the fuel and precipitation of alteration products in a breached fuel rod could quickly lead to axial splitting, or "unzipping," of the cladding. Another case is that the precipitating alteration phases will fill the gap and fracture openings and, as a result, limit the rate of further fuel degradation and radionuclide release. A further possibility is that cladding corrosion from the fuel-side will cause additional cladding degradation and exposure of the fuel pellet fragments (Cunnane et al., 2003). Because the specific effects of cladding failure are planned to be evaluated and integrated into the models of UF degradation in the future, this work focuses on an idealized case where the breached cladding does not influence the fuel matrix degradation or radionuclide mobilization.

Because some radionuclides are dissolved in the UO_2 matrix grains, their releases are controlled by the degradation rate of the UF matrix itself (e.g., Pu, Np). In addition to these solid solution radionuclides, some other radionuclide releases may be controlled, in part, by the matrix degradation rate. These include fission products present in the *inaccessible* grain boundaries (i.e., those grain boundaries occluded to fluid until the fuel matrix alters enough to provide fluid access). Some fission products occur as discrete phases (e.g., the five-metal alloy particles, or epsilon phase) in both the matrix grains and in the inaccessible grain boundaries. These portions of the inventory are referred to collectively as the "matrix inventory" because matrix degradation is required prior to release of these radionuclides. The matrix inventory does not include radionuclides located within the *accessible* grain boundaries (see below). Note that the epsilon phase particles seem to corrode slower than the fuel matrix (Sassani, 2011; Sassani et al., 2012), and therefore release of radionuclides from these noble metal phases may lag the degradation of the matrix itself.

Other than the radionuclide inventories whose releases are controlled by UF matrix degradation, there are portions of the inventories of fission gases and of more volatile radioelements (e.g., cesium, iodine, and technetium) that are released virtually instantaneously upon cladding breach (i.e., the instant, or fast, release fractions-IRF). This IRF is mostly fission products that have migrated out of the matrix during in-reactor operations and accumulated as gases or minor condensed phases along the fuel gap (i.e., the interface between the pellets and the cladding), the rod plenum regions, and in the readily accessible pellet fractures and grain boundaries (this includes epsilon phase particles). Within this work, these locations are collectively referred to as the "gap region" that contains the inventory of radionuclides that are released independently of the UF matrix degradation rate.

On the basis of the above discussion, the radionuclide inventory in UF can be subdivided in this manner:

- The *IRF* inventory (includes fission gases) comprised of radionuclides located in

    – The rod plenum regions (e.g., Kr and Xe)

    – The fuel gap (between pellet & cladding; Figure 1.3)

    – The accessible grain boundaries/pellet fractures (Figure 1.3)

- The *matrix* inventory (Figure 1.3) that includes the UF matrix itself and radionuclides located within

    – The matrix grains as solid solutions

    – The inaccessible grain boundaries and fractures

    – The epsilon phase particles both (a) enclosed in the matrix and (b) within the inaccessible grain boundaries (NOTE: the epsilon particles undergo their own degradation rate once exposed by matrix degradation)

These inventories, the major rate limiting processes (e.g., matrix degradation, noble metal particle degradation), and radionuclide mobilization processes and models for each of these fractions are summarized below.

Instant Release Fractions

Within the grain-boundary region of the fuel pellet, radionuclides may be readily releasable (accessible grain boundary inventory), or may be inaccessible (the inaccessible grain boundary inventory – see Figure 1.3). This latter portion would remain unreleased until degradation of the UF matrix occurs to the point where these grain boundaries are now exposed to fluids. Mobilization of the inaccessible grain-boundary inventory requires prior degradation of the matrix grains to make accessible these initially inaccessible grain boundaries in the UF. Degradation of the grain boundaries may occur due to the effects of helium production from α-particle decay on the mechanical stability of the grain boundaries (Ferry et al., 2006) or from preferential corrosion at/along the grain boundaries. Although this is straightforward in concept, delineation of the accessible grain boundaries from the inaccessible ones is not a simplistic task and methods of measuring the grain boundary inventories (e.g., grinding of samples) tend to capture the total rather than discriminate between the two (BSC, 2004; Roudil et al., 2007). Similar complications of discrimination apply also to the accessible versus inaccessible fractures within a used fuel pellet.

Because the initial fraction of inaccessible grain boundaries and the progression of the grain boundary corrosion within geologic disposal systems are not well understood, it has been common for the entire grain boundary inventory to be conservatively assumed to be released instantaneously (i.e., as part of the IRF) upon water ingress into the breached fuel rods (BSC, 2004; Johnson et al., 2005). Additional empirical data obtained from long-term fuel corrosion testing indicates that oxidative dissolution of the fuel matrix is a general corrosion process and does not exhibit substantial preferential corrosion along the grain boundaries (Une and Kashibe, 1996; BSC, 2004). This suggests that the inaccessible grain boundary inventory would be mobilized at a rate similar to radionuclides within the fuel matrix, and could

therefore be released in proportion to the matrix degradation. Further data for distribution of inaccessible grain boundary radionuclide inventory and advanced understanding of grain boundary degradation in UF would facilitate this approach, particularly for high burnup (BU) UF, which has additional structural changes/complexity as BU increases (Figure 1.4).
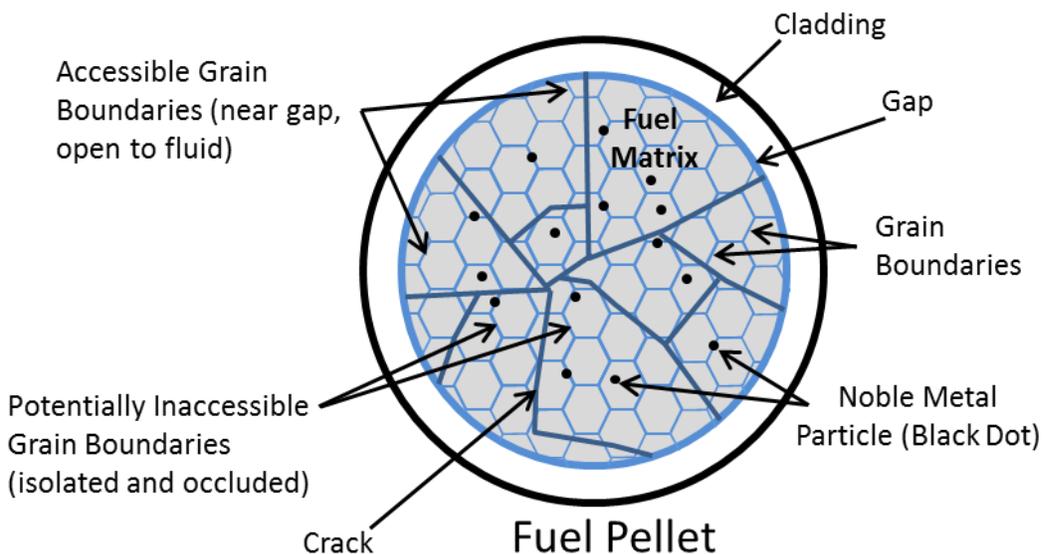
Figure 1.3. Schematic of a fuel pellet cross section showing the relative locations of radionuclide inventories for the gap, grain boundaries, fuel matrix, and noble metal particles. Also shown schematically are the general locations of accessible and inaccessible grain boundaries.

For the purposes of this work, a transition point to high BU UF is defined as occurring at 45 MWd/kgU such that any UF that has a BU >45 MWd/kgU is referred to as high BU. This is in part based on the observation that the amount of fission gas release (FGR; e.g., Kr and Xe) for LWR UF depends more strongly on the magnitude of BU for fuels above 45 MWd/kgU (e.g., see Figure 1 in Johnson et al., 2012). Besides containing more fission products, such high BU UF exhibits distinct structural changes at the pellet rim that are driven by locally increased ^{239}Pu content. The increased ^{239}Pu causes elevated local BU (factor of 2 to 3) that results in a finer-grained structure with higher closed-porosity (containing fission gases) that occurs as a rim layer (Johnson et al., 2005; Serrano-Purroy et al., 2012). This rim layer of high-BU structure (Figures 1.1-1.4) is noticeable in UF starting around a BU of 40 MWd/kgU (Johnson et al., 2005). The rim region grows progressively thicker as BU increases (and with increase in other irradiation history parameters De Pablo et al., 2009) and is separated by a transitional region from a core lacking high-BU structure (Serrano-Purroy et al., 2012).

Models that have been developed (BSC, 2004; Johnson et al., 2005) for mobilization of the gap and grain-boundary inventories assume conservatively that they are instantaneously released (i.e., the IRF) when groundwater contacts the UF through the breached cladding for even a pinhole failure. As UF BU increases, fission products are more abundant and FGR is observed to increase, so IRF models are either correlated (Johnson et al., 2005) to BU and FGR, or at

least account for a substantial range (BSC, 2004) of these parameters. One set of IRF model values (for Sr, I, Cs, and Tc; BSC, 2004) covers a UF FGR range of 0.59 to 18% FGR. The IRF distributions generated for that model simply span the entire range of FGR evaluated, which represents a BU values up to about 50 MWd/KgU, and include the variability across the range to capture conceptual uncertainty in this parameter. It is recommended that the BSc (2004) distributions be used to analyze IRF in PA with consideration of the uncertainty for fuels of BU below about 50 MWd/KgU. As discussed in that work, comparison to additional literature data indicates that the distributions for Sr and Tc release may not be conservative (BSC, 2004). However, BSC (2004) also noted that both Tc and Sr are radioelements that can be affected strongly by matrix dissolution within testing data, such that the values may be inadvertently high in some studies. Using the BSC (2004) distributions for fuels above 50 MWd/KgU is not recommended because they are not demonstrably conservative compared to the pessimistic estimate model values from Johnson et al. (2005 - discussed below) for higher BU values.
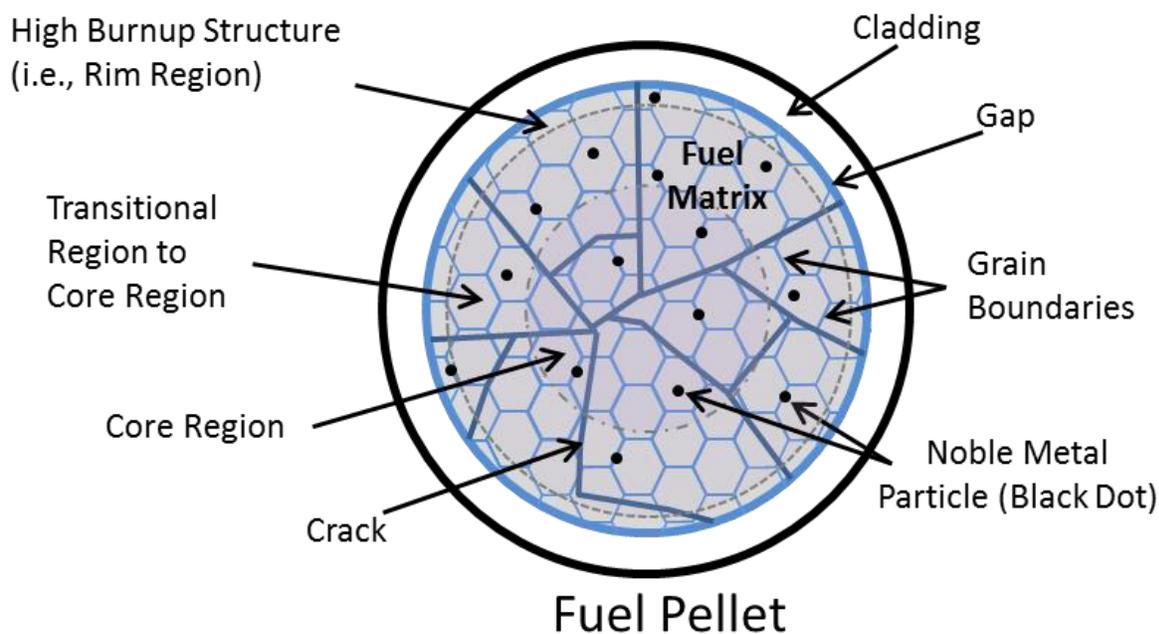
Figure 1.4. Schematic of a fuel pellet cross section for high BU UF showing the rim region high-BU structure, transitional region, and core region (after Fig. 1, Serrano-Purroy et al., 2012).

An extensive evaluation of IRF for UO_2 (and mixed oxide - MOX) fuels by Johnson et al. (2005) has been conducted based on correlations of fission product (e.g., Cs, Sr, I, Tc, and C) leaching data with FGR (e.g., Xe). Johnson et al. (2005) combined those measurements with FGR correlations as a function of BU to extrapolate IRF data for value estimates to higher BU. Johnson et al. (2005) produced best estimate and pessimistic estimate IRF values for UF as a function of the fuel BU. These estimates are indicated to be reliable for low to moderate BU UO_2 fuels, and less certain for the higher BU fuels for which experimental leaching data are

sparse (Johnson et al., 2005). However, additional studies of high BU fuels, some explicitly analyzing the UF rim regions and cores separately (Roudil, et al., 2007; De Pablo et al., 2009; Serrano-Purroy et al., 2012) suggest that these model values may be conservative estimates of the IRF (especially Tc).

Because of the need to evaluate the variability of UF BU in the source-term of performance assessment, it is recommended that the best- and pessimistic-estimate values of Johnson et al. (2005) be used to define the minimum and maximum values, respectively, for uniform distributions at each BU for which they are listed. This will allow evaluating the major BU variation for UF up to 75 MWd/KgU. Linear interpolation between listed BU values should be used to generate distributions for intermediate BU levels, but extrapolation beyond the maximum BU given by Johnson et al. (2005) should not be performed.

Johnson et al. (2005) utilized direct consideration of both FGR and BU for constructing their model values. In addition, Johnson et al. (2012) pointed out that high FGR in some fuels (specifically 11% and 18% in ATM-106 with BUs of 46 and 50 MWd/KgU, respectively) is not due to higher BU, rather it is likely due to original lower density of the manufactured fuel providing higher open porosity. This would mean that simply using estimates dependent solely on FGR could lead to overestimates of the IRF in such cases. Mobilization models for the IRF (which estimate the fraction of the inventory of key radionuclides that are instantly released upon cladding breach) could be parameterized to include changes that may occur over time throughout the post-closure period as a result of additional migration of radionuclides within the UF structure (Johnson et al., 2005; Poinssot et al., 2005). These effects are currently viewed as second order and are probably captured by the more conservative values recommended above.

Matrix Degradation Rate

The major elemental components comprising the matrix of the UO_2 and MOX UF are U and Pu. Minor elemental constituents (e.g. Pd and other noble metal fission products) may also influence the corrosion of the fuel matrix, for example by catalyzing cathodic reactions. When the fuel matrix is corroding, the inherent corrosion potential of the primary mass of the oxide grains (UO_2 and MOX) controls and buffers the electrochemical conditions at and near the corroding surface. Many of the radioelements in UF (e.g. U, Pu, Np, Tc, I) are multivalent elements. The valence of the ions produced in the corrosion process depends on the corrosion conditions (e.g., potential and pH) at the surface of the corroding UF matrix. Because oxidation and dissolution of U and Pu produces high valence cations (oxidation states higher than 4), following their dissolution these ions undergo extensive hydrolysis and precipitate to form rind layers on the UF. Other multivalent radionuclides may only be present in their lower oxidation states during the fuel matrix corrosion process if the corrosion potential of the fuel matrix in its disposal environment is sufficiently low. Consequently, the radionuclides mobilized in lower valence (and less soluble) states may be retained in the rind layer unless they are subsequently oxidized to a higher oxidation state and dissolved into the bulk solution.

The oxidation of the UF surface within reduced disposal environments may be driven by radiolytically generated oxidizing species. Species such as H_2O_2 may be the dominant oxidant produced by alpha radiolysis at long times (Sassani et al., 2012; Wittman and Buck, 2012). However, in these environments; generation of hydrogen gas from metal corrosion with water may provide a source of reductants for reaction with such oxidants. It is possible that such

reactions may protect the UF surface from oxidative dissolution and may be facilitated by the cathodic and/or catalytic behavior of epsilon phase particles in the UF itself (Jerden et al., 2013). For such a case, simple solubility-driven dissolution of the UF would provide much slower degradation of this waste form in reduced disposal environments. Quantification of these processes and implementation/extension of process models to account for them has been a focus of the UFD&RM activities (Sassani et al., 2012; Wittman and Buck, 2012; Jerden et al., 2013). These models are summarized here for the context of incorporating them into PA models, with detailed descriptions of the process models given in Sections 2 and 3, and the strategy for coupling them given in Section 4.

Radiolytic products exert strong effects on UO_2 dissolution at the solid-aqueous interface. Therefore, the effects of radiolysis on solution redox speciation at this interface need to be considered within UO_2 corrosion models. Initial RM implementation (Wittman and Buck, 2012) is based on the kinetics of Christensen and Sunder (2000). Within the water system, H_2O_2 becomes the dominant radiolytically generated oxidant. Uncertainty in model parameters and reaction mechanisms was analyzed to quantify the sensitivity of dissolution rate to RM parameters and to identify the largest uncertainties. The RM has been verified using additional reaction sets from Poinssot et al. (2005) and Pastina and LaVerne (2001). Additionally, experiments are being performed to reduce model uncertainties and validate model concepts (Sassani et al., 2012). These experiments include studies of radiolytic H_2O_2 production and thermal degradation rates in solution and studies using synthetic fuels to evaluate future alpha radiolytic conditions in disposal systems (Sassani, 2011; Sassani et al., 2012). Such testing will provide validation studies for the RM and/or parameter values to the UFD&RM process models. The RM is being expanded to include heterogeneous environments consisting of solid-water layer-gas phase, and to include chloride for evaluating a generic salt environment.

The overall objective of this work was to implement a predictive model for the degradation of used uranium oxide fuel that is based on fundamental electrochemical and thermodynamic principles. This objective was achieved (Sassani et al., 2012; Jerden et al., 2013) by the initial MPM implemented in the form of a computational tool that is based on the Canadian-mixed potential model for UO_2 fuel dissolution (King and Kolar, 1999; 2003; Shoesmith et al., 2003). This initial implementation extends the Canadian version to include hydrogen oxidation at the UF surface with provisions to include reactions catalyzed by noble metal particles present at the fuel surface. The MPM was verified by reproducing published results from the Canadian model and sensitivity analyses[1] were used to determine which model parameters and input variables have the largest effect on degradation rate. As part of the work at ANL, experimental methods have been developed to measure electrochemical and reaction kinetic parameters to support modeling investigations and to quantify epsilon particle effects on matrix degradation for inclusion in an updated MPM (for details see Jerden et al., 2012, FCRD-UFD-2012-000169 and Jerden et al., 2013 FCRD-UFD-2013-000057; and Sassani et al., 2012 for general discussion).

In addition to the process model developed for matrix degradation, studies of the mechanistic behavior of the corrosion products of UO_2 and the energetics of UO_2 bulk and surface reactions have been performed to compliment the continuum model for matrix degradation. A computational first-principles study of the structures of the uranyl peroxide hydrates studtite and metastudtite documents their structures obtained from total energy calculations using

density functional theory (Weck et al., 2012). These computational results are in very good agreement with those characterized by experimental X-ray diffraction methods. Such work tests this computational tool to quantify their thermodynamic properties for use in similar studies of UO_2 bulk and surface chemistry (Weck et al., 2013). Such first-principles studies will serve to provide parameter constraints for process models of UF degradation and to supply validation comparisons.

1.2.3   Integration into the performance assessment models

Performance assessment models provide a common conceptual and computational framework for the simulation of coupled thermal-hydrologic-chemical-mechanical-biological-radiological processes that govern the behavior of nuclear waste disposal systems (Freeze and Vaughn, 2012). Within the common performance assessment models framework, a range of disposal system alternatives (combinations of inventory, EBS design, and geologic setting) can be evaluated using appropriate model fidelity that can range from simplified reduced-dimension representations running on a desktop computer to complex coupled relationships running in a high-performance computing environment (see e.g., Fig. 2.1-1 in Sassani et al., 2012). It should be noted that used fuel degradation and related EBS processes are part of the PA model integration structure envisioned in the Generic Disposal System Modeling (GDSM) and Advanced Disposal System Modeling (ADSM) (Freeze et al., 2013). For example, Figure 1.5 shows the "Source Term and EBS Evolution" (top-left) box delineating waste form (WF) degradation as part of the breakdown of key source term and EBS coupled processes within the PA integration scheme.

The EBS is represented with a number of major barriers of various types depending on disposal environment, as well as with various waste forms, including UF that is the primary topic of this article. Most of the models implemented currently in the performance assessment models for EBS are more idealized than fully coupled, but the plan is to augment or replace those simpler models with more comprehensively coupled process models as the work progresses. The models for UF degradation processes are expected to be some of the earliest augmentations.

Consideration of the context in the evolution of the post-closure environment is needed when applying the process models for used fuel degradation either on their own, or within the PA models. Temporal evolution of both the natural and engineered barriers in the system will have thermal, hydrologic, chemical, and mechanical changes driven by the system conditions as well as by the placement of the waste forms in that system. A stylized example of the chronological evolutions of such system conditions is shown in Figure 1.6 for an argillite (clay/shale) disposal environment. This figure is based on a similar chronological description for THMC coupled processes in an argillite repository for the TIMODAZ project described in Yu et al. (2010). The thermal evolution is driven primarily by the radioactive decay of the used fuel and provides coupled effects within the three other process areas (e.g., drying of the immediate vicinity). Note that the chemical conditions are those imposed from the evolution of the natural system and the engineered barriers excluding the waste form itself. The models discussed within this report are those that would evaluate additional chemical aspects of the fuel either generated from the radiolytic effects of the used fuel on any water (relevant only once there is a breach of both waste package and cladding) or vapor, as well as bulk chemical changes due to the dissolution/degradation of the fuel itself. In general, the point in time of these failures will be out in time after the thermal perturbation of the system has decreased. This is just one

example of such temporal changes for one possible generic disposal system and the process models in this report are developed to be able to address the range of possible conditions, focusing primarily on the dominant conditions expected for fuel degradation during post closure.
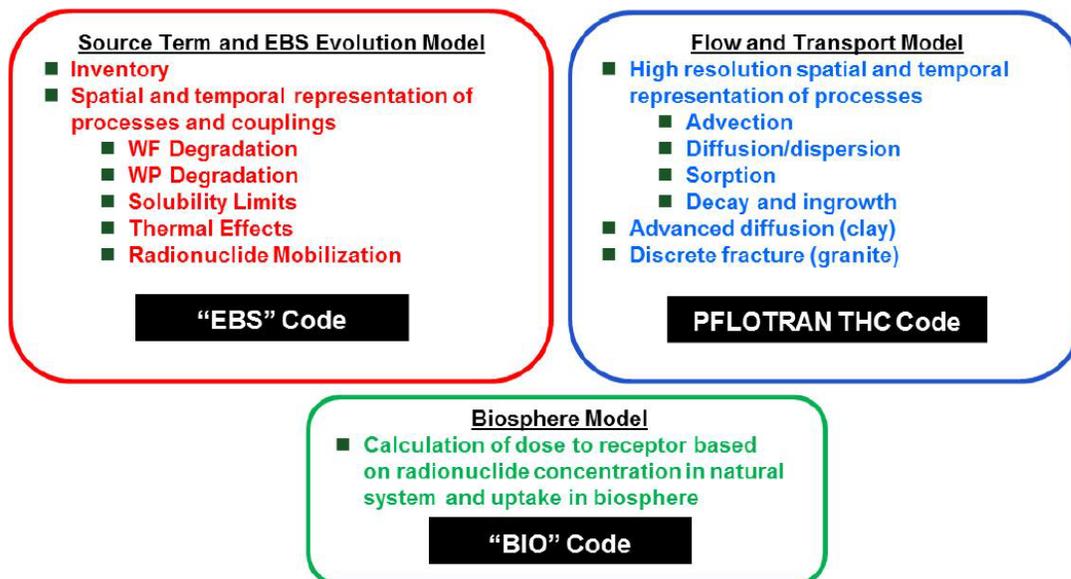
Figure 1.5. Disposal system integrated process models (Freeze et al. 2013).

		Cell Closure	Repository Closure			Post-Closure Period	

Years	1	10	100	1000	10000	100000	1E+06
Temperature (T)	Thermal Pulse		Temperature Decrease			Site Geothermal Gradient	
Hydrological (H)	Dryout Period	Swelling Clay Plug 0% ~90%	>90%	High RH After 1000 years >97%		~90 - ~100%	
	Dryout Period	Concrete Plug 0% >90%	>90%	High RH After 1000 years >97%		~90 - ~100%	
	Dryout Period	Drift Wall / Liner 0% <70%	~80 - <97%	High RH After 1000 years >97%		~90 - ~100%	
	Dryout Period	Clay Outer Barrier 0% <70%	~80 - <97%	Moderate RH After 1000 years ~80 - ≤97%		~80 - ~100%	
	Dryout Period	Clay Inner Barrier 0% <70%	~80 - <97%	Moderate RH After 1000 years ~80 - ≤97%		~80 - ~100%	
	No water contacting WPs					WP Breach Water in Contact with WPs	
	Micro-cracked Argillites	70% ~80%	~80%	~80% - ~100%		~100%	~100%
Chemical (C)	Oxidizing Conditions	Mildly Reduced	Reducing Conditions				
	Outer Metal Sleeve Corrosion		Overpack Corrosion				
			Hydrogen Production from Corrosion				
			Primary Package Corrosion				
			Glass Dissolution				
	Plug / Concrete Degradation						
	Alkaline Plume in Near-Field Bentonite / Cement Plug						
	Wasteform Degradation, RN Release Sorption, Colloid Formation/Transport						
Mechanical (M)	Variation in Argillite Creep Rates in the Near-Field			Liner Rupture		Overpack & Canister Rupture	

Figure 1.6. Schematic example of an idealized chronological evolution of the thermal, hydrologic, mechanical, and chemical (THMC) conditions for a generic argillite (clay/shale) disposal environment. Percentages in the hydrological part of the diagram represent percent of water saturation in the media.

For the source-term models of the four generic disposal environments, the implementations are generally simplified. For example, in Clayton et al. (2011) the generic salt source-term model is described as follows:

> *Waste form degradation is assumed to release radionuclides into a large uniformly mixed container representative of the source-term water volume. The source-term water volume is obtained by multiplying the source-term bulk volume by its porosity. The dissolved concentrations of radionuclides in the source term mixing cell are then calculated based on the mass of radionuclides released from the waste form, the source-term water volume, and the radionuclide solubility. ... As the model matures and information becomes available, more realistic representations of the processes will replace this initial simplified approach.*

Within that generic salt source-term model, two components relate directly to the degradation of UF: (a) waste form degradation, and (b) solubility of key radioelements for the performance assessment models analyses. This UFD&RM work is focused currently on providing augmented process models for part (a), specifically for UF as a waste form. The salt source-term representation of the waste form degradation in Clayton et al. (2011) includes the source-term, degraded waste form, and primary engineered barriers components. These two simplified aspects of that approach could be updated based on the models in this work. Such update would mean that instead of the generic source term having "No gap/grain boundary fraction" and simply sampling a distribution for "Fractional Degradation Rate", there would be an instant release fraction included (sampled based on the distributions described above) and the fractional degradation rate could be calculated using the model instead of sampled.

The primary connection into the current performance assessment models for the UFD&RM models is the fractional degradation rate (FDR) parameter, which is currently sampled from a distribution as indicated above. This primary coupling allows for development of more process-based models that are able to supplant the FDR distribution by supplying that parameter directly as a result of the process model. This is the initial connection that is needed for implementation of the UF MPM described above. In addition, a second connection could be generated to represent the instant release fraction. Sampling of the IRF distributions within the PA model would be done similar to the current sampling of the FDR distribution to describe the fast/instant release fraction radionuclides that are mobilized instantly at the time of cladding breach. The distributions for the IRF would only need to be sampled at the initiation of UF degradation for each fuel rod represented as having a breach in its cladding.

A coarse connection to chemical environment (defined in the performance assessment models and needed as input to the UFD&RM models) exists currently in the form of the four generic disposal environments. At present this is sufficient as the UFD&RM models discussed herein are developed for granitic reducing environments and explicit coupling to chemistry variation is expected to be an ongoing enhancement, with a primary target of extending the model applicability into clay/shale and deep borehole environments (expansion to specific brine environments appropriate to salt systems will be undertaken in the future if needed). This is also the case for thermal and pressure dependencies that will be further incorporated into the UFD&RM models and will capture essential environment and temporally-changing conditional parameters. It is expected that as these enhanced models are incorporated into the performance assessment models, expanding explicit environment/chemical variability coverage within the models will become more efficient.

Our general strategy for integrating process models with each other, and within the performance assessment models, is to identify initially the major feeds among the process models (given in detail in Section 4) and from the process models to performance assessment models (see below for discussion of connections). For coupling into performance assessment models, our approach begins with the direct, though idealized, interface connections that exist, with further couplings added as the process models themselves become more highly coupled. The ultimate tool for connection with the PA models in intended to be a single coupled process model, or fuel degradation model FDM – see Section 4), for analyzing the fractional degradation rate of used fuel within the PA Models. Note that even after coupling, the RM and MPM process models can be used individually for sensitivity and uncertainty analyses as well.

One more simplistic approach to coupling to the PA models would be to use the RM and MPM (or even the FDM) process models to generate a set of histories based on radiation and thermal output of the fuel through time. This could be done initially for each generic disposal chemical environment (e.g., granitic groundwater or clay/shale), and simply directing the PA model to select the appropriate set of histories to sample depending on which environment was being analyzed.

Such a unidirectional coupling may only be an initial stage of coupling the FDM with PA models and the approach could progress to the direct incorporation of the coupled process model into the PA models. Such a thorough coupling would entail passing water compositional parameters (potentially from other internal chemistry models) to the FDM, which would analyze the UF degradation in this environment and provide the fractional degradation rate for those specific water compositions. This would be a bidirectional coupling example. Further coupling of the FDM into the PA model with a full suite of coupled thermo-hydro-chemical processes would allow a fully coupled feedback where, in addition to the fractional degradation rate being provided to the performance assessment models, the change to water composition based on the UF degradation could be supplied as well. The potential connections between the FDM and the other PA model subsystems are shown in Figure 1.7. Such a staged developmental strategy facilitates incorporation of process-level detail as it is available and permits an evolving level of complexity to be incorporated in a deliberate manner.
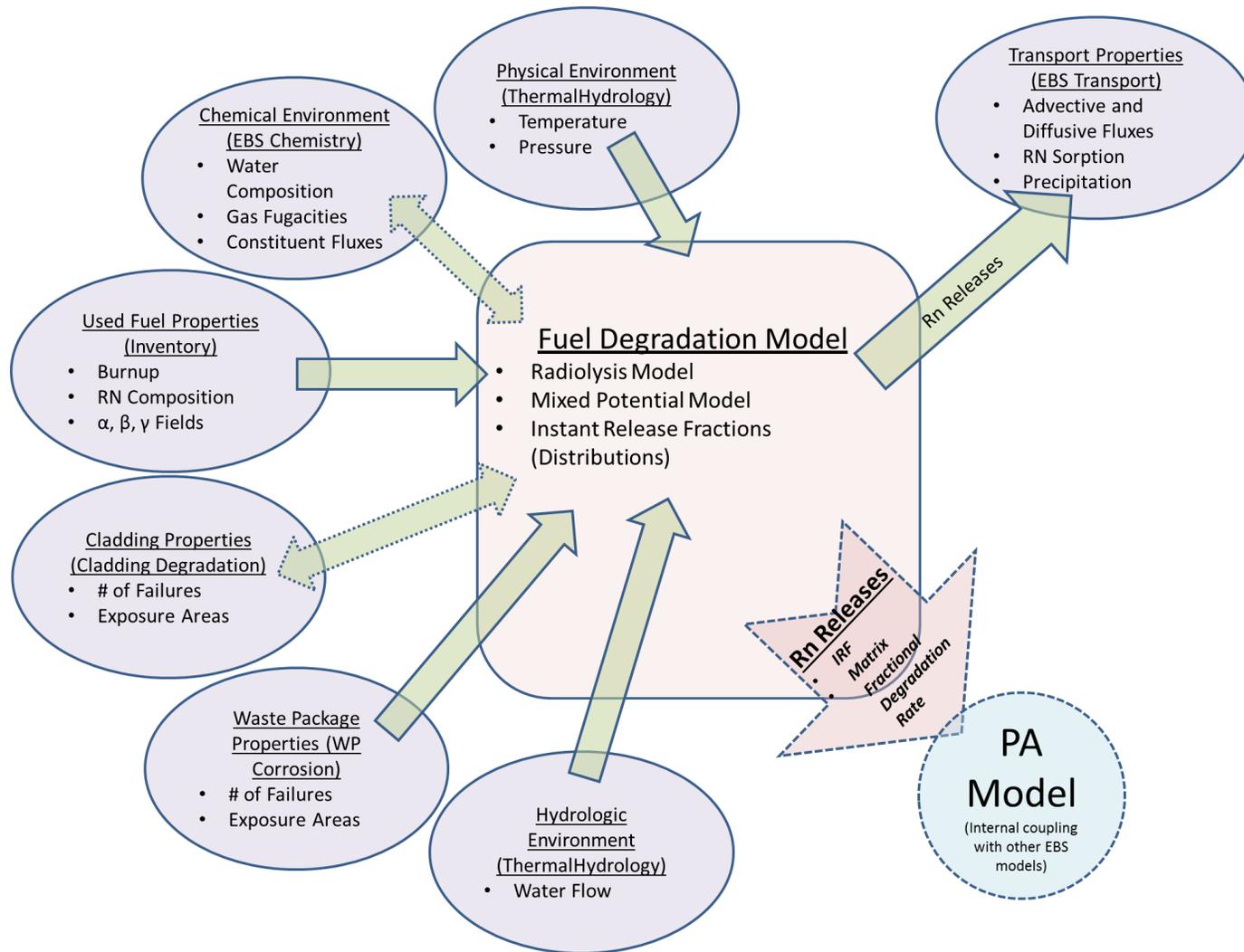
Figure 1.7. Schematic of potential parameter connections for fully embedded coupled fuel degradation model with a performance assessment (PA) model. Solid arrows unidirectional connections, whereas dotted arrows indicate bidirectional couplings between subsystem models within the PA model.

1.2.4   Summary

The contributions presented in this manuscript are being accomplished via a concerted effort among three different national laboratories: SNL, ANL and PNNL. This collaborative approach includes experimental work, process model development (including first-principles approaches) and model integration—both internally among developed process models and between developed process models and PA models. The main accomplishments of these activities are summarized as follows:

- Delineation of constraints for the IRF from the nuclear fuel implemented in two sets of distributions: (a) triangular distributions representing minimum, maximum, and mean (apex) values for LWR UF with BU at or below 50 MWd/KgU, and (b) uniform distributions as a function of BU representing instantaneous radionuclide releases for UF with BU up to 75 MWd/KgU.

- Computational development and implementation of a radiolysis model using a comprehensive set of radiolysis reactions to better account for potential solution compositions to be encountered in repository environments (Wittman and Buck, 2012). The current model (Section 2) allows for heterogeneous CO_2 speciation thus accounting for the presence of HCO_3^-. Comparisons of modeling results are in good agreement with those reported in other studies.

- Computational implementation and verification/validation of the Canadian mixed potential model for UO_2 fuel corrosion in the initial mixed potential model (MPM - Jerden et al., 2013). This MPM (Section 3) is based on the fundamental electrochemical and thermodynamic properties described by interactions at the fuel – fluid interface and captures key processes such as hydrogen oxidation and the catalysis of oxidation/reduction reactions by noble metal particles on the fuel surface (epsilon phases).

- A computational first-principles study of the structures of the uranyl peroxide hydrates studtite and metastudtite (Weck et al., 2012). The structures obtained from total energy calculations using density functional theory are in very good agreement with those characterized by experimental X-ray diffraction methods. Such work tests this computational tool to predict the phase stability of UO_2 corrosion products and quantify their thermodynamic properties for use with similar studies of UO_2 bulk and surface chemistry (Weck et al., 2013).

- Development of an idealized strategy for model integration with PA approaches to analyze generic disposal environments (Section 1.2.2). However, it is an ongoing task to delineate in detail how these process models will couple to other EBS process submodels within the PA model for generic evaluations of the safety case.

- Advanced strategies for coupling the RM and MPM into a single tool for use in analyzing the matrix degradation rate (fractional and absolute) of used fuel (Section 4). Identification of parameters needed to couple the codes together as well as four strategies for implementing the coupling are given in detail in Section 4.

2.   SUMMARY OF RADIOLYSIS MODEL

The radiolysis model (RM) calculates the concentration of species generated at any specific time and location from the surface of the fuel (Wittman and Buck, 2012). The model will be used as a component in a total system model for assessing the performance of UNF in a geological repository. The total system model will account for time-dependent phenomena that may influence UNF behavior. One major difference between used fuel and natural analogues, including unirradiated UO_2, is the intense radiolytic field. The radiation emitted by used fuel can produce radiolysis products in the presence of water vapor or a thin-film of water (including hydroxide (•OH) and hydrogen (•H) radicals, oxygen ion (O_2^-), aqueous electron (e_{aq}), hydrogen peroxide (H_2O_2), hydrogen gas (H_2), and the secondary radiolysis product, oxygen (O_2)) that may increase the waste form degradation rate and change radionuclide behavior.

2.1   Objective

The radiolysis model developed for this analysis is formulated as a set of coupled kinetics equations for the reactions of aqueous species assumed to exist in the environment inside the Engineered Barrier System (EBS). Radiolytic species are generated at a rate that is based on the dose rate induced by the radiation field. Subsequent reactions of the radiolytic species are then computed based on the reaction kinetics. The model inputs are the reaction rate constants, the temperature and dose rate, the radiolytic G-values, and the initial concentrations of species in the system. The conditional G-value for H_2O_2 production, ($G_{i,cond}$), is provided to the MPM (see equation 2.3).

2.2   Physical Model

It is well known that the radiation emitted by used fuel will produce radiolysis products in the presence of water vapor or a thin-film of water (including OH• and H• radicals, O_2, e_{aq}, H_2O_2, H_2, and O_2). However, for these products to increase or change the rate of UNF degradation and result in the release of radionuclides requires understanding the processes that might occur in these interfacial regions.

The initial attempts of radiolysis model development concerned the production of radiolytic species with time. Developing codes that would provide values for time periods relevant to experimentation required modifying codes for stability. Diffusional terms were added to provide greater realism in the model. This enabled determination of a 'steady state' value for a particular radiolytic species or other chemical species distant from the fuel surface. These are the values that would be provided to the MPM. A further improvement to the model has been to capture the dose dependent radiolytic processes that would occur very close to the surface. This adaptation has made the RM more closely related to the MPM. The earlier versions assumed almost constant dose within the first 30 μm of the surface where most alpha energy would be deposited. However, it was realized that this was a poor representation of the system and this region was further sub-divided into zones where the dose was modeled to change with distance from the surface. The radiolysis model remains effectively a one-dimensional model of the surface of the fuel.
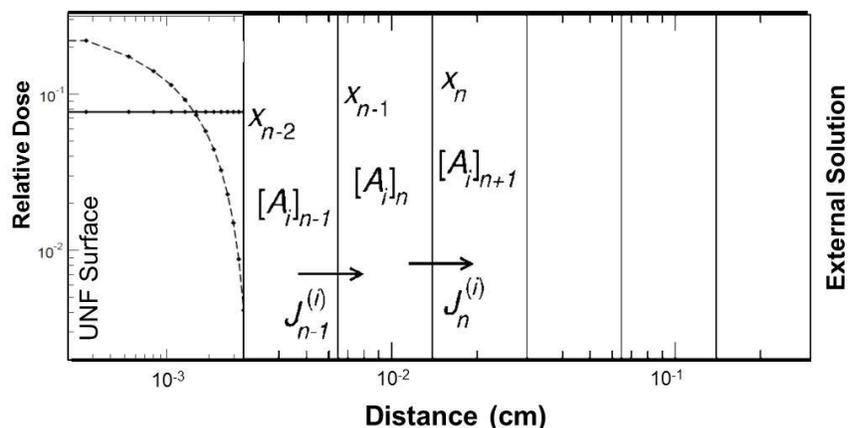
Figure 2.1. Radiolysis model showing generation modified with a dose dependence term in the irradiated zone and the diffusion zones across spatial regions.

The early versions of the radiolysis model were verified by using the reactions reported by Pastina and LaVerne (2001) and those of Poinssot et al. (2005) to reproduce their results, which had been done using FACSIMILE and MAKSIMA-CHEMIST kinetic software products, respectively.

Table 2.1 Alpha particle G-values (Pastina and LaVerne, 2001)

Species	*G-value at 5 MeV (molecules/100-eV)*
H^+	0.18
H_2O	-2.58
H_2O_2	1.00
$e_{(aq)}^-$	0.15
$\bullet H$	0.10
$\bullet OH$	0.35
$\bullet HO_2$	0.10
H_2	1.20

User-defined inputs

- Length of model diffusion grid (fuel surface to environmental boundary, default is 5 millimeters)
- Number of calculation nodes (points) in diffusion grid (default is 24) with 14 zones in the alpha penetration zone.
- Duration of simulation (days to reach steady state)

Parameters

- Alpha-particle penetration depth (35 µm)
- Generation value for H_2O_2 (G_{H2O2}) (moles per alpha energy deposited per time) (see Table 2.1 for H_2O_2 and other species)
- Rate constants *(function of temperature)* (taken from Pastina and LaVerne, 2001; Poinssot et al. 2005)
- Diffusion coefficients *(function of temperature)* (see Table 2.2)
- Activation energies for temperature dependencies (available for H_2O_2 only)

Constants (not explicit in model)

- pH of bulk solution (case dependent)
- Pressure (O_2, H_2 are set and tracked as dissolved concentrations)

Variables

- Dose rate
- Temperature
- Starting concentrations of oxidants and complexants: $[O_2]$, $[CO_3^{2-}]$, $[H_2]$

Calculated by model (output)

- Conditional G-value for H_2O_2
- Conditional G-values for all other species (not used in MPM)

2.3   Mathematical model

Concentrations in each region are coupled through diffusive currents and are expressed in Equations 2.1 and 2.2. The coupled kinetics rate equations for the solution species concentrations $[A_i]$ are:

$$\frac{d\,[A_i]_n}{dt} + \frac{J_n^{(i)} - J_{n-1}^{(i)}}{x_n - x_{n-1}} = G_i' \dot{d}_n + \sum_{r=1}^{N_r} k_{ir} \prod_{j_r=1}^{n_r} [A_{j_r}]_n^{O_{j_r}} \tag{2.1}$$

with rate constants k_{ir}, dose rate and radiolytic generation constants G_i, where the diffusive currents ($J^{(i)}$) and diffusion constants (D_i) appear in the discretized Fick's Law according to:

$$J_n^{(i)} = -2D_i \frac{[A_i]_{n+1} - [A_i]_n}{x_{n+1} - x_{n-1}}$$

(2.2)

for each component *i* in region *n*. Table 2.2 shows the values of diffusion constants used in the model. For brevity, the "sum-of-products" on right-hand side of Equation 2.1 expresses the sum of the product of reactant concentrations entering with reaction order O_{jr} where the multiplication-index j_r is over the n_r reactants for reaction *r*. The notation includes the final state order of component *i* produced by writing the rate constants k_{ir}, dependent on index *i*, but of course that dependence only amounts to an integer (which could be zero) multiplied by the reaction rate constants.

Table 2.2 Diffusion constants (Christensen and Sunder, 1996)

Species	$D_i (10^{-5} \cdot cm^2 \cdot s^{-1})$
$e_{(aq)}^-$	4.9
OH	2.3
O^-	1.5
H_2O_2	1.9
O_2	2.5
H_2	6.0
Others	1.5

2.3.1   Geometric scale

The length of the logarithmic grid of the model diffusion cell is adjustable but was set at 3 millimeters for all of the sensitivity runs performed to date (Figure 2.2). The number of calculation points along the diffusion grid can also be set by the user but has been adjusted to match the MPM.

We consider only the α-induced G-values (Table 2.1) because the near-field dose at the fuel surface is strongly dominated by α-dose for decay times greater than 30 years when the dose is ~160 rad/s for 50 GWd/MTU used nuclear fuel (Raduldescu, 2011). Consistent with α-decay radiation, the dose rate is assumed to be nonzero only in the nearest 35 μm to the fuel surface. Figure 2 shows the spatial regions modeled from near the fuel surface to the external solution boundary considered to be at 3.5 mm. The products of G-values with the dose rate act as generation term to the kinetics equations for each of the species and are represented in Figure 2.2. Concentrations in each region are coupled through diffusive currents and are expressed in Equations 2.1 and 2.2. Within the first 35 μm layer, the radiation dose will be greatest immediately close to the fuel surface and then drop off. The radiolysis model can either consider a constant average dose in this region, or consider the dose dependent production of radiolytic species. In Figure 2.3, the effect of including or excluding dose dependence is shown.

When the dose dependence is included, H_2O_2 production close to the fuel surface decreases. The conditional G-value ($G_{i,cond}$), is calculated from Equation 2.3 (see below) for each node within the alpha penetration zone :

$$\overline{G}_{i,\text{cond}} \equiv G_i + \frac{1}{x_d \rho \dot{d}} \int_0^{x_d} dx \left\{ \sum_{r=1}^{N_r} k_{ir} \prod_{j_r=1}^{n_r} [A_{j_r}]^{O_{j_r}} \right\}_{\text{Steady-State}} = \frac{1}{\rho \dot{d}} \left\{ \frac{J^{(i)}(x_d)}{x_d} \right\}_{\text{Steady-State}} \tag{2.3}$$

where ρ is the density, d, is the dose rate, and x_d is the radiation zone distance.
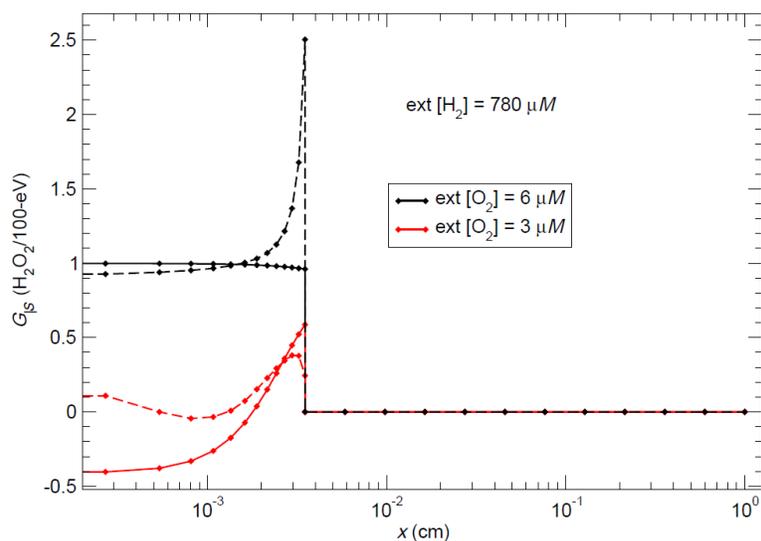
Figure 2.2. Predicted conditional G-values for H_2O_2 with distance from the fuel surface showing effect of external O_2 at a fixed H_2 concentration.

2.3.2   Time scale

The magnitude of each time step is determined by the total simulation time and the number of temporal calculation points specified. Both of these values are set by the user. The time steps are spaced logarithmically, with the finer spacing at the beginning of the run. For simulation runs of 1-10 days, optimal time steps range from 0.1 seconds early in the simulation to hours towards the end of the simulation.

The kinetics equations become unceasingly stiff as a dose rate of 137~rad/s is approached from below (Figure 2.4). At a dose rate of 138 rad/s, the solution transitions to a new steady state which is smaller in the H_2O_2 and O_2 concentrations - even though the dose rate is greater. The steady state solution is non-unique for this system. This is not surprising because of the many non-linear terms in the kinetics equations. Additionally, at least two steady state solutions exist above and below the critical dose rate, but only one is attained for a specific initial condition. The dashed curves in Figure 2.5 assume that the dose rate changes continuously after the previous steady state is attained in both the forward (red-dashed) and reverse (black-dashed)

direction. The dose change in the reverse (black-dashed) direction shows that two steady state solutions exist even below the critical dose rate.
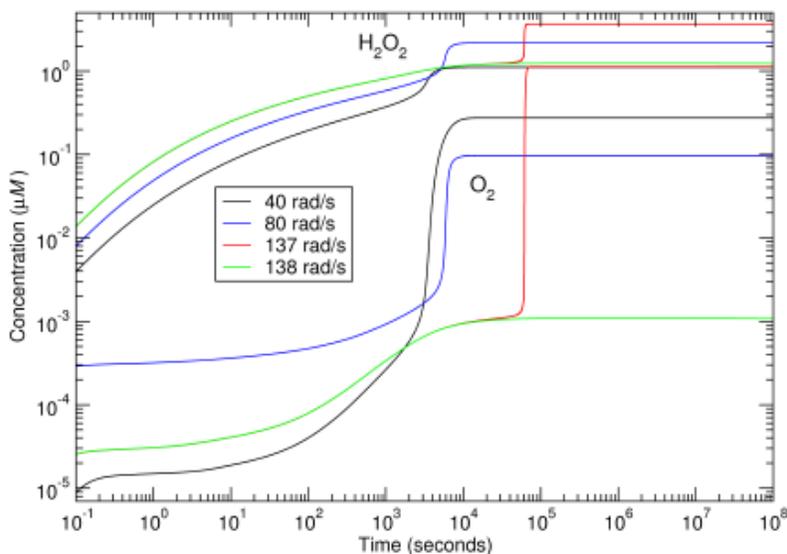
Figure 2.3. Time dependent concentration of H_2O_2 and O_2 at the surface with dose rates of 40 rad/s (black), 80 rad/s (blue), 137 rad/s (red), 138 rad/s (green).
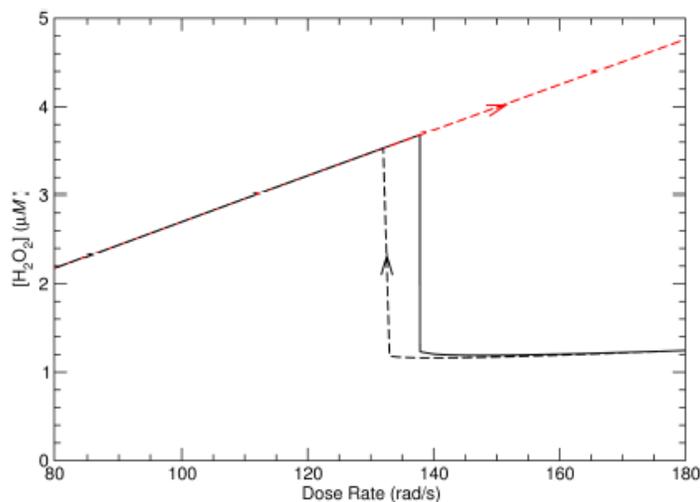
Figure 2.4. Steady-state concentrations of H_2O_2 at surface with dose rate for fixed initial conditions (black-solid), forward running steady-stated (red-dashed), reverse running steady-state (black-dashed).

Results from the radiolysis model including diffusional terms, suggests that steady state conditions under two conditions can lead to discrete jumps in concentrations. It has been observed, even at fixed dose rate that jumps in conditional G-values can occur.

3. SUMMARY OF MIXED POTENTIAL MODEL

3.1 Objective and Background

The objective of the mixed potential model (MPM) is to calculate the used fuel degradation rates for a wide range of disposal environments to provide the source term radionuclide release rates for generic repository concepts. The fuel degradation rate is calculated for chemical and oxidative dissolution mechanisms using mixed potential theory to account for all relevant redox reactions at the fuel surface, including those involving oxidants produced by solution radiolysis. The MPM was developed to account for the following key phenomena (Jerden et al. 2013):

- Rate of oxidative dissolution of the fuel matrix as determined by interfacial redox reaction kinetics (quantified as corrosion potential) occurring at the multiphase fuel surface (phases include UO_2 and the fission product alloy or epsilon phase).
- Chemical or solubility based dissolution of the fuel matrix.
- Complexation of dissolved uranium by carbonate near the fuel surface and in the bulk solution.
- Production of hydrogen peroxide (the dominant fuel oxidant in anoxic repository environments) by alpha-radiolysis.
- Diffusion of reactants and products in the groundwater away from and towards the reacting fuel surface.
- Precipitation and dissolution of a U–bearing corrosion product layer on the fuel surface.
- Diffusion of reactants and products through the porous and tortuous corrosion layer covering the reacting fuel surface.
- Arrhenius-type temperature dependence for all interfacial and bulk reactions.

Because the MPM is based on fundamental chemical and electrochemical principles, it is flexible enough to be applied to the full range of repository environments as well as shorter-term storage scenarios being considered as part of the UFD campaign. The Argonne Mixed Potential Model (MPM) was produced by implementing the Canadian mixed potential model for UO_2 fuel dissolution (King and Kolar, 1999, King and Kolar, 2003, Shoesmith et.al., 2003) using the numerical computing environment and programming language MATLAB. The implementation and testing of the Argonne MPM is discussed in the following reports: Jerden et al., 2012, FCRD-UFD-2012-000169 and Jerden et al., 2013 FCRD-UFD-2013-000057 and the integration of the MPM and RM with other process models being developed as part of the UFD program was discussed in Sassani et al., 2012, M2FT-12SN0806062. The MPM includes a simplified module for calculating the production of H_2O_2, which is the sole radiolytic species required in the current implementation for granitic environments. This is being replaced by the RM to take into account local variations in the concentrations of radiolytic species as affected by dose, chemical interactions in the groundwater, decay, and diffusion. Key aspects of the MPM affecting the integration of the RM, including the geometric and temporal scales of the models, are discussed below.

3.2   Physical model

The MPM consists of ten one-dimensional reaction-diffusion equations (see Jerden et al., 2013), that describe the mass transport, precipitation/dissolution and redox processes of the ten chemical species included in the model. Figure 3.1 shows the MPM spatial diffusion grid and the distribution of individual calculation nodes (shown as vertical lines).
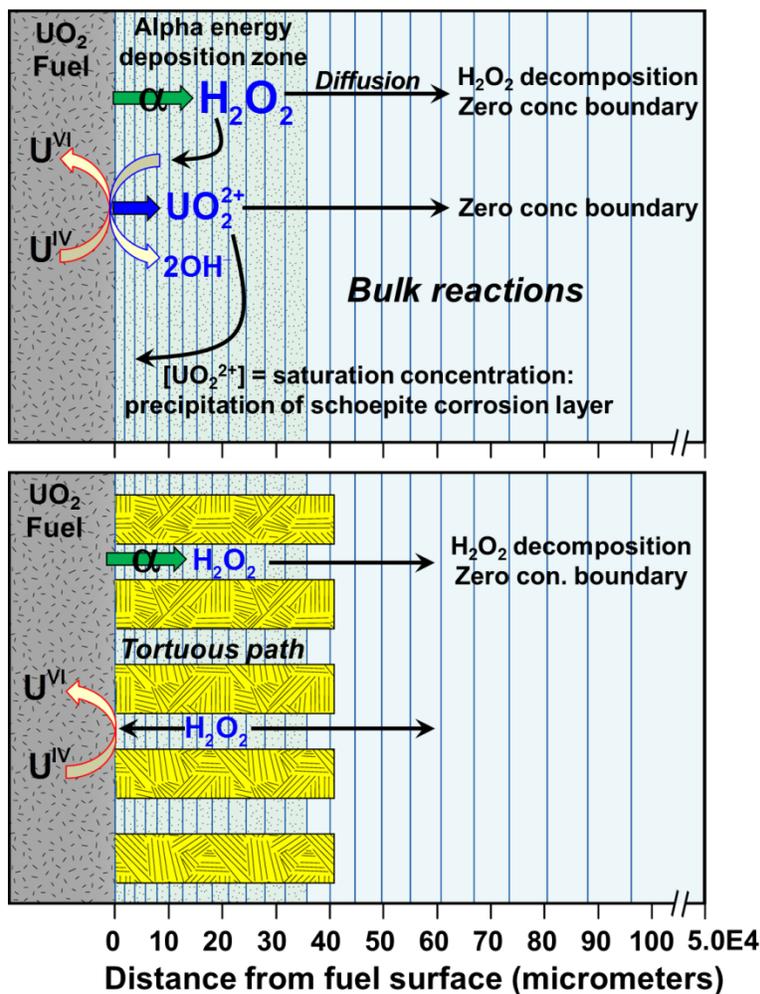
Figure 3.1. Spatial diffusion grid for MPM showing individual calculation nodes as vertical lines and summarizing key processes accounted for by the model (top image). Note the logarithmic distribution of calculation points at the fuel/solution interface. The baseline number of individual calculation nodes for the MPM is 200 (not all shown); however, this number can be increased by the modeler if higher spatial resolution is required. The bottom image focuses on how the presence of a U(VI) corrosion layer can influence the fuel degradation rate by blocking alpha energy from being deposited in solution and by moderating the diffusion of species towards and away from the reacting fuel surface.

Electrochemical rate expressions are used as boundary conditions for species that participate in the interfacial electrochemical reactions. These reactions, as well as key bulk reactions accounted for in the model are listed in Table 3.1.

Table 3.1. Surface electrochemical reactions and bulk solution reactions tracked in the MPM.

Reactions
Anodic reactions at fuel surface
$UO_2 \rightarrow UO_2^{2+} + 2e^-$
$UO_2 + 2CO_3^{2-} \rightarrow UO_2(CO_3)_2^{2-} + 2e^-$
$H_2O_2 \rightarrow O_2 + 2H^+ + 2e^-$
$H_2 \rightarrow 2H^+ + 2e^-$
Cathodic reactions at fuel surface
$H_2O_2 + 2e^- \rightarrow 2OH^-$
$O_2 + 2H_2O + 4e^- \rightarrow 4OH^-$
Homogeneous Bulk Reactions
$UO_2^{2+} + 2H_2O \rightarrow UO_3{:}2H_2O + 2H^+$
$UO_2(CO_3)_2^{2-} + 2H_2O \rightarrow UO_3{:}H_2O + 2CO_3^{2-} + 2H^+$
$UO_3{:}H_2O + 2CO_3^{2-} + 2H^+ \rightarrow UO_2(CO_3)_2^{2-} + 2H_2O$
$O_2 + 2H_2O + 4Fe^{2+} \rightarrow 4Fe(III) + 4OH^-$
$H_2O_2 + 2Fe^{2+} \rightarrow 2Fe(III) + 2OH^-$
$UO_2^{2+} + Fe^{2+} \rightarrow Fe(III) + U(IV)$
$UO_2(CO_3)_2^{2-} + Fe^{2+} \rightarrow Fe(III) + U(IV) + 2CO_3^{2-}$
$H_2O_2 \rightarrow H_2O + 0.5O_2$

The inclusion of alpha radiolysis in the MPM is essential because, at low concentrations of dissolved oxygen, the only oxidants within a repository system are radiolytic species (e.g., molecular hydrogen peroxide). Therefore, predicting an accurate rate of fuel matrix degradation in anoxic settings such as crystalline rock and clay/shale repository environments requires an accurate description of radiolysis.

Calculating the alpha dose rate (and thus H_2O_2 concentration) for corroding UO_2 fuel is complicated by the effects of U(VI) corrosion products (modeled as schoepite, $UO_3 \cdot 2H_2O$ in MPM). The U(VI) corrosion product layer has three effects on the rate of fuel degradation predicted by the MPM:

- Slows rate of oxidative dissolution by decreasing the reactive surface area of the fuel (blocking or masking reaction sites).

- Slows rate of oxidative dissolution by blocking alpha-particles from interacting with water and producing radiolytic oxidants (decreases total moles H_2O_2 produced near fuel surface). The magnitude of this effect is proportional to surface coverage of corrosion layer.

- Corrosion layer can slow the rate of oxidative dissolution by slowing the rate of diffusion of oxidants to the fuel surface: U(VI) layer is a tortuous porous mass of crystals (simulated in MPM by a parallel pores with constant tortuosity).

All three of these effects are modeled in the MPM by a radiolysis "sub-routine" that was recoded (for details see Jerden et al., 2013) from the original Canadian mixed potential model (King and Kolar, 1999). As in Canadian model, alpha-particles in the MPM are assumed to have a constant energy of 5.3 MeV and a solution penetration distance (α_{PEN}) of 35 µm. The modeler can set the penetration distance over the range of $\alpha_{PEN} = 45$ micrometers for ~6.0 MeV alpha-particles down to $\alpha_{PEN} = 10$ µm for ~2.3 MeV particles (King and Kolar, 1999). In the MPM, the default generation value for hydrogen peroxide produced by alpha-radiolysis is assumed to be 1.021E-4 mol/Gy/m^3 (Christensen and Sunder, 2000).

As stated above, the main objective of the current report is to present a strategy by which this simplified radiolysis "sub-routine" can be replaced by the more rigorous radiolysis model. To facilitate the discussion of this model integration effort, the geometry assumed for the MPM and the chemical processes that are taken into account are summarized below:

User-defined inputs

- Length of model diffusion grid (fuel surface to environmental boundary, default is 5 millimeters)

- Number of calculation nodes (points) in diffusion grid (default is 200)

- Duration of simulation

- Surface coverage of fission product alloy phase

Parameters

- Alpha-particle penetration depth

- Generation value for H_2O_2 (G_{H2O2}) (moles per alpha energy deposited per time). This will be replaced by the $G_{i,cond}$ which is calculated and passed from the RM to the MPM (defined in section 2.3 above).

- Charge transfer coefficients

- Rate constants *(function of temperature)*

- Standard potentials *(function of temperature)*

- Diffusion coefficients *(function of temperature)*

- Saturation con. U(VI) *(function of temperature)*

- Activation energies for temperature dependencies

- Porosity of schoepite (corrosion) layer

- Tortuosity of schoepite (corrosion) layer

- Resistance between UO_2 and fission product alloy (epsilon) phase

Constants (not explicit in model)

- pH of bulk solution nominally 9.5 (pH implicit in parameter values)

- Pressure (O_2, H_2 are set and tracked as dissolved concentrations)

Variables

- Dose rate

- Temperature

- Starting concentrations of oxidants and complexants: $[O_2]$, $[CO_3^{2-}]$, $[H_2]$, $[Fe^{2+}]$

Parameters Calculated by model (output)

- Corrosion potential

- Current densities for interfacial redox reactions

- Flux of species from fuel surface

- Concentrations of all species at each node (point) in diffusion grid after each time step

- Corrosion layer thickness

3.3   Mathematical Model

The mathematical approach for the MPM is described in detail in Jerden et al., 2012 and Jerden et al., 2013. The key aspects of the approach are how oxidants that cause fuel degradation are treated. The two oxidants currently included in the MPM are (1) hydrogen peroxide, which is formed by alpha radiolysis of water, and (2) oxygen, which has two sources: the initial amount in the environment (set by modeler) and an amount formed by the decomposition of hydrogen peroxide at the fuel surface and in the bulk solution. The mass balance equations that track hydrogen peroxide and oxygen are shown as Equations 3.1 and 3.2 (applied at every node within the 5 mm diffusion grid).

$$\varepsilon \frac{\partial C_{O_2}}{\partial t} = \frac{\partial}{\partial x}\left(\tau_f \varepsilon D_{O_2} \frac{\partial C_{O_2}}{\partial x}\right) - \varepsilon k_3 C_{O_2} C_{Fe^{2+}} \tag{3.1}$$

$$\varepsilon \frac{\partial C_{H_2O_2}}{\partial t} = \frac{\partial}{\partial x}\left(\tau_f \varepsilon D_{H_2O_2} \frac{\partial C_{H_2O_2}}{\partial x}\right) + \varepsilon G_{H_2O_2} R_D - \varepsilon k_4 C_{H_2O_2} C_{Fe^{2+}} \tag{3.2}$$

where ε is the porosity of the schoepite corrosion layer (default value is 45%), C_i is concentration of species i (moles/L), t is time (years), x is the horizontal distance along diffusion grid (micrometers), τ is the tortuosity factor for pores in shoepite corrosion layer (default is 0.1), k_3,

k_4 are the rate constants for the reduction of oxygen and hydrogen peroxide by aqueous ferrous iron by the reactions given in Equations (3.3) and (3.4), G_{H2O2} is the radiolytic generation value of hydrogen peroxide (moles/(J/kg)/seconds), R_D is dose rate (Gy/second). Similar mass balance equations exist for all species included in the MPM.

$$O_2 + H_2O + 4Fe^{2+} \rightarrow 4\ Fe^{3+} + 4OH^- \tag{3.3}$$

$$H_2O_2 + 2Fe^{2+} \rightarrow 2Fe^{3+} + 2OH^- \tag{3.4}$$
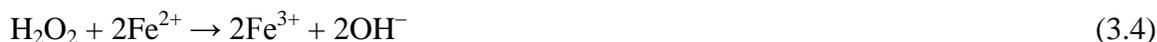
The thickness of the schoepite corrosion layer is determined by computing the integral of the mass per volume (moles/m^3) of schoepite for every grid point and using the molecular weight, mineral density and porosity to determine the x dimension of the layer.

The rate of generation of hydrogen peroxide is determined by the generation factor in mol/(J/kg)/m^3 multiplied by the dose rate (J/kg) and the radiolysis cutoff distance [g(x)] which is defined as the zone of solution irradiated by the fuel. In the current version of the MPM, the amount of energy absorbed by solution in the 35 micrometer irradiated zone is constant. The current model does not account for attenuation of the alpha particle energy away from the fuel surface, but this may be included with the RM.

3.3.1   Geometric Scale

The length of the logarithmic grid of the model diffusion cell is adjustable but has been set at 5 millimeters (as shown in Figure 3.1) for all of the sensitivity runs performed to date. The number of calculation points along the diffusion grid can also be set by the user. Based on the simulations with times greater than 1000 years we have performed to-day, 200 grid points provides a good balance between the amount of time required to run the model and the spatial resolution of component concentrations within the grid.

3.3.2   Time Scale

The magnitude of each time step is determined by the total simulation time and the number of temporal calculation points specified. Both of these values are set by the user. The time steps are spaced logarithmically, with the finer spacing at the beginning of the run. For simulation runs of 10000 years or more, optimal time steps range from 0.1 years early in the simulation to 1000 years towards the end of the simulation.

3.4   Example of MPM Calculations

Figure 3.2 shows examples of results from MPM simulations of reaction for ten thousand years with hydrogen peroxide generation values from 1.0E-4 moles/(J/kg)/m^3 (theoretical value from Christensen and Sunder, 2000) to 1.0E-5 moles/(J/kg)/m^3 (arbitrarily chosen to study model sensitivity). For this model run the temperature and dose rate within the model diffusion grid were held constant at 25°C and 0.1 Gy/s respectively, the initial oxygen concentration was 1.0E-6 moles/L and the background concentrations of carbonate, iron and hydrogen were set to zero.

To give a sense of the temporal resolution of the model for the default settings of 200 grid points and 100 time steps, results for each time step are shown as individual data points in Figure 3.2. The top plot shows that the rate of oxidative dissolution of the fuel decreases by a factor of

approximately 2 due to the precipitation of the schoepite corrosion layer, which physically prevents alpha particles from irradiating the solution at the surface of the fuel. Because the corrosion layer is modeled as a set of uniform parallel pores, the amount of fuel area masked is determined by its porosity (default is 50%). The oxidative dissolution rate is also predicted to decrease by a factor of 8 due to this lower production rate of hydrogen peroxide from the order of magnitude decrease in the G_{H2O2}. The dissolution rate does not decrease further because the background concentration of oxygen supports oxidative dissolution of the fuel.

The middle diagram of Figure 3.2 shows the current densities for the dominant interfacial redox reactions. The kinetic balance of these cathodic and anodic reactions determines the corrosion potential from which the oxidative dissolution rate of the fuel is calculated. The bottom diagram shows the steady state diffusion profiles for hydrogen peroxide over the diffusion grid. This plot highlights the effect of the schoepite corrosion layer in both blocking alpha-particles emitted from the fuel from irradiating the solution and in moderating the diffusion to and from the reacting fuel surface.
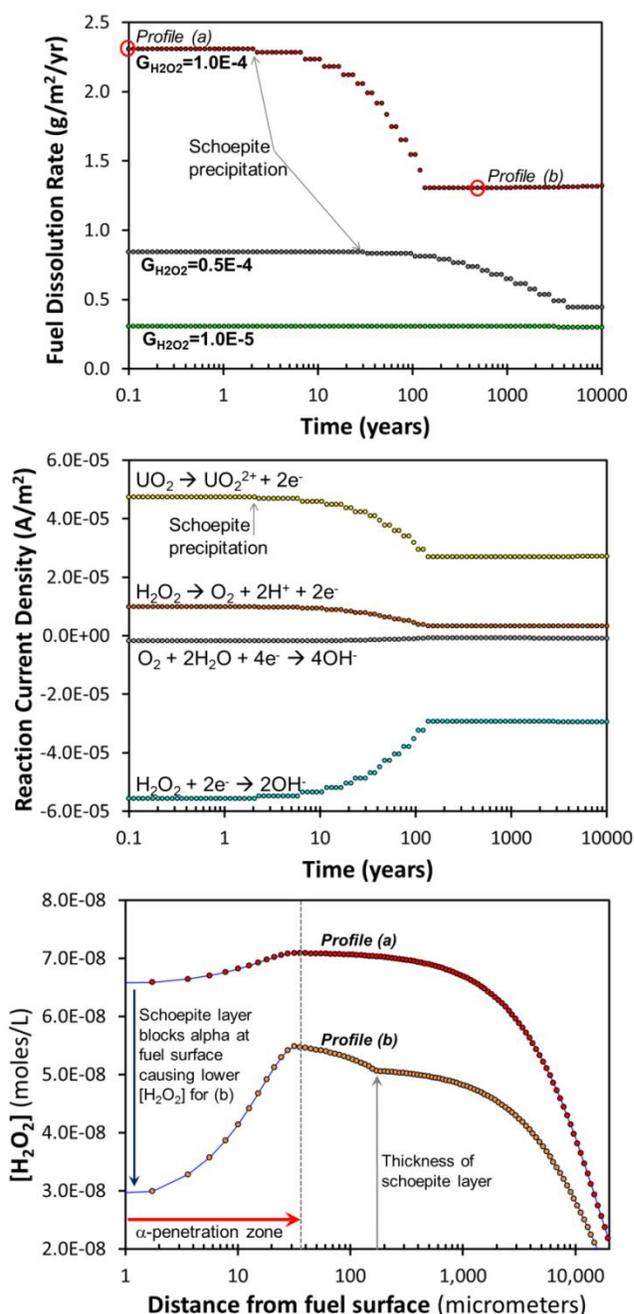
Figure 3.2. Results from recent MPM runs investigating the sensitivity of fuel degradation rate to changes in the G-value for H_2O_2 in mole/(J/kg)/second (top). Individual time steps are represented as single data points. The middle diagram shows the reaction current densities (G_{H2O2}=1.0E-5) for the redox reactions that determine the fuel corrosion potential and fuel degradation rate. The bottom diagram shows H_2O_2 concentration profiles for the two time steps identified in the top diagram.

4.   COUPLING MPM/RM MODELS

Coupling the RM and MPM will provide a scientifically rigorous predictive tool for calculating the degradation rate of used fuel. By combining the models, we ensure that the fuel degradation calculations used to determine performance assessment source terms account for all major radiolytic, electrochemical and corrosion processes that can influence radionuclide release. The conceptual approach for coupling the RM and MPM is summarized in Figure 4.1. This diagram shows that the integrated Fuel degradation model consists of three modules:

- The *Radiolysis Module* (green box), which provides a rigorous treatment of chemical processes associated with the absorption of ionizing radiation near the surface of the exposed fuel. Supplies concentrations used to calculate fuel matrix degradation.
- The *Mixed Potential Module* (blue process boxes), which provides the rate of fuel matrix degradation (accounts for both oxidative and chemical dissolution).
- The *Instant Release Fraction*, which provides the masses of key radionuclides that will be released from the fuel promptly after the time of exposure (release rate is more rapid than predicted matrix degradation rate).
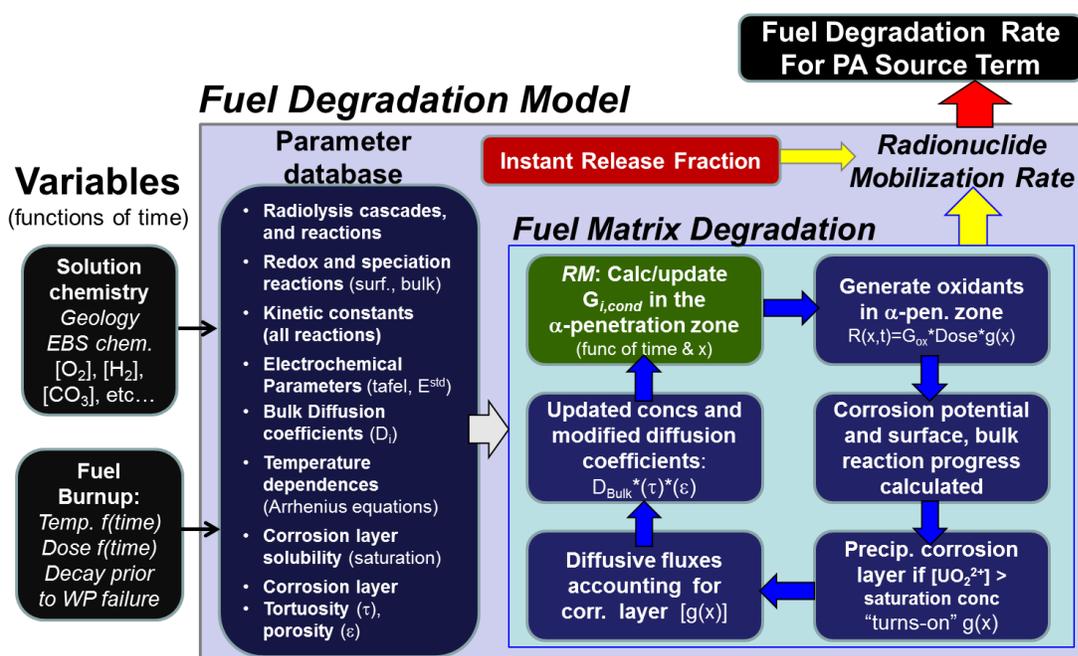
Figure 4.1. Summary information flow diagram highlighting the coupling of radiolysis, matrix, and instant release process modules within the FDM (MPM shown by blue boxes, RM by green box, and IRF by red box), and PA.

The strategy for development and implementation of the integrated Fuel Degradation Model (FDM) involves the flow of information both to and from other performance assessment level models. As shown in Figure 4.1, required inputs to the FDM include quantitative descriptions of the composition of the groundwater/in-package solution in contact with the fuel as well as information regarding the fuel being modeled, such as the changes in fuel temperature and dose rate with time. The temperature and dose information, which are directly used in the FDM, are

determined by the fuel burn-up as well as the decay or cooling time elapsed prior to fuel exposure to environmental solutions (e.g., time before repository emplacement + time after emplacement before waste package failure).

The initial conditions, temperature and dose rate functions will be combined with an extensive radiolysis-electrochemical-kinetic database and used by the FDM to produce a rate of fuel matrix degradation. The matrix degradation rate will be combined with inventory-specific instant release fraction calculation to yield a radionuclide mobilization rate source term on a per waste package basis for performance assessment calculations.

As shown in Figure 4.1, the key link between the RM and MPM is the conditional generation values for radiolytic species. Conditional generation values take into account the effects of shielding by alteration layers and chemical reactions in the evolving solution on the G values ($G_{i,cond}$). Coupling of the models involves the passing of spatial solution concentrations from the MPM to the RM and then the conditional generation values for relevant species from the RM to the MPM for use in the next time step of the MPM (Figure 4.1). For this exchange to work, the spatial calculation grid within the alpha penetration zone must be identical in each model (currently 14 nodes within 35 micrometers of the alpha source).

4.1   Parameter values provided by RM to MPM

The RM will provide conditional G-values for all oxidants capable of degrading the fuel (currently H_2O_2 and O_2) as well as hydrogen, which can protect the fuel from oxidative dissolution if its oxidation is catalyzed at the reacting surface. The conditional G-values will be supplied to the MPM for every calculation node located within the α-particle penetration zone (currently 14 nodes over the 35 μm α-particle penetration zone).

The conditional G-values calculated by the RM are more accurate that the theoretical G_{H2O2} used as a default in the MPM because the RM accounts for the diffusion of, and reactions between, intermediate radiolytic species such as e_{aq}^-, •H, •OH, •OH_2, and •CO_3^-. Examples of reactions that can lead to a decreased yield of hydrogen peroxide relative to the amount predicted in the MPM are:

$$H_2O_2 + e_{aq}^- \rightarrow OH\text{-} + \bullet OH \tag{4.1}$$

$$H_2O_2 + \bullet H \rightarrow H_2O + \bullet OH \tag{4.2}$$

$$H_2O_2 + \bullet OH \rightarrow H_2O + \bullet OH_2 \tag{4.3}$$

$$H_2O_2 + \bullet OH_2 \rightarrow H_2O + O_2 + \bullet OH \tag{4.4}$$

$$H_2O_2 + \bullet CO_3^- \rightarrow CO_3^{2-} + O_2^- + 2H^+ \tag{4.5}$$

4.2   Parameter values provided by MPM to RM

For the RM to calculate an accurate description of the generation values for relevant radiolytic species (e.g., H_2O_2) it needs the following information from the MPM:

- Concentrations of species that are radiolytically active (e.g., species such as CO_3^{2-} or Cl^- that produce reaction cascades when excited) or otherwise interact with radiolytic species (e.g., O_2, H_2, Fe^{II}).

- The modified diffusion coefficients for all relevant species (e.g., O_2, H_2, Fe^{II}, CO_3^2) at all calculation nodes present within the tortuous corrosion layer (see Figure 2 for visual explanation of assumed corrosion product geometry)

Matching/partitioning physical, chemical, radiolytic processes

Physical, chemical and radiolytic processes will matched by ensuring that the same spatial diffusion grid is used for both models. Diffusion depends on the spatial dimension of the grid, so a uniform 5 millimeter linear distance will be used for both models as a default; however, this value can be altered by the modeler. To ensure that the chemical and radiolytic processes match both models will contain the same number, and spacing of calculation nodes within the alpha penetration zone (default is 14 nodes). The key time and space dependent variables dose rate and temperature will also be matched in the two models.

Coordinating time scales

The RM calculations that produce the conditional G-values require short time steps relative to the MPM (kinetics on order of seconds). Therefore, the two models will not be time synchronized. Rather the RM will be run independently and the resulting conditional G-values will be handed off at a specific time point during a MPM simulation. There are three options for timing this hand-off:

- Option: Use RM to provide conditional G–value at each time step in MPM
- Option: Use RM to provide conditional G–value after a constant number of time steps in MPM
- Option: Use the RM to identify solution concentrations that have significant impact on $[H_2O_2]$ and conditional G-value

The best option in terms of model fidelity is for the RM to provide the conditional G-values at the beginning of each MPM time step. This will be the option pursued as we move forward with implementation of the coupled model.

Conditional G-factor

G_{cond} is defined as the steady state generation value (moles of species (i) per alpha energy deposited) averaged over the 35 micrometer alpha penetration depth adjacent to the fuel surface. The G_{cond} value is generated from Equation 2.3 for feeding into the MPM. The conditional G-value is dependent on the solution conditions and environment.

To accurately calculate G_{cond} for a solution generated by a given number of MPM time steps, the RM will need the following information:

- Dose rate.

- Temperature.

- Concentrations of reactive species $[O_2]$, $[H_2]$, $[CO_3^{2-}]$, and for application to other generic forms of geologic repository, terms for $[Cl^-]$, $[Br^-]$, $[SO_4^{2-}]$, and others will become important.

- Diffusion coefficients of relevant species at the last MPM step (these change in alpha penetration zone when a corrosion layer is present due to tortuosity factor.)

- Thickness of corrosion layer.

The dose rate and temperature are characteristics of the fuel and disposal system, and the other values are calculated or tracked in MPM. All are handed off to RM whenever it is determined that a new G_{cond} is needed for the next time step of the MPM run. The need for a new G_{cond} could be triggered by concentration thresholds determined to result in significant changes in the G-values from previous sensitivity runs (e.g., sets of H_2 and O_2 concentrations that favor the rapid decomposition of H_2O_2) (see Figure 2.3 and 2.4).

4.3   Interface Approaches

Several options being considered for coupling the RM and MPM are listed below. Different options have advantages and disadvantages based on the extent of coding that would be required and the ease of use of the final product.

Option 1: Add radiolysis module as subroutine within mixed potential module code. This would involve re-coding the RM from Fortran into MATLAB or alternatively recoding the MPM into Fortran so that the two models would run as part of the same program.

- Pros: full RM code included in integrated model, not limited to abstracted form of the RM, seamless transfer of information.
- Cons: relatively large amount of time and effort required to support recoding.

Option 2: Represent radiolysis module as an analytical expression within mixed potential module code. This would involve minimal coding in MATLAB, but would require significant effort to define an analytical form that captures the full range of conditional dependencies accounted for in the RM.

- Pros: coding work is streamlined and simplified, seamless transfer of information.
- Cons: uncertainty of success of approach, it is not clear that a single analytical expression can capture all of the relevant conditional dependencies accounted for in the full RM.

Option 3: Provide radiolysis module results as look-up table of conditional generation values produced by running the RM over the full range of relevant conditions. This G-value look-up table would be treated by the MPM as part of the parameter database.

- Pros: no coding work needed, seamless transfer of information.
- Cons: relatively large amount of time and effort to produce exhaustive table that considers all relevant conditions,

Option 4: Maintain radiolysis model and mixed potential module as separate codes that call each other during a fuel degradation model run.

- Pros: no coding work needed, not limited to abstracted version of the RM.
- Cons: uncertainty of success of approach, it is not clear that the Fortran and MATLAB codes and pass the needed information back and forth as they currently exist. Even if possible this approach may dramatically increase computing time needed to run the FDM.

4.3.1   Sensitivity Analysis: MPM (MATLAB) – DAKOTA Interfacing

4.3.1.1   Introduction

The source term is a very important element of repository performance assessment (PA) that describes the spatio-temporal variations in radionuclide releases in a disposal environment. Intrinsic geologic and geochemical complexities and their time-dependent interactions in the host medium can produce a large suite of scenarios for radionuclide releases and migration in the disposal environment. For this reason, uncertainty and sensitivity analyses are essential to the evaluation of process models and their responses to the disposal concept PA (Helton et al., 2006; Saltelli et al., 2000).

Sensitivity analysis (SA) methodologies are key to the evaluation of the simulation parametric responses affecting model behavior and their uncertainties, particularly in complex systems. SA permits the analysis of distinct input perturbations and their influence to model outputs where various approaches have been applied to a wide variety of process models, including those relevant to chemical systems (Helton et al., 2006; Saltelli, 2009; Saltelli et al., 2005, 2012; Saltelli et al., 2000; Saltelli et al., 2004). Saltelli et al. (2000) provides an example of the application of SA methods to the analysis of radionuclide migration in natural and engineered barriers on the basis of chemical mass transfer and reaction in a porous medium. Given the emphasized importance of SA to PA and also to model integration and analysis, SA of the used fuel corrosion model has been conducted based on variations of key environmental inputs. The next sections describe the approach entailing code coupling of the ANL Mixed Potential Model and the DAKOTA code suite for uncertainty quantification and optimization.

4.3.1.2   Sensitivity Analysis (SA): Approach Description

Sensitivity analyses of the Mixed Potential Model (MPM) were conducted by externally-coupling the MPM Matlab code with the DAKOTA toolkit in a Microsoft Windows 7 environment. DAKOTA is an open source multilevel parallel object-oriented framework developed at Sandia National Laboratories. The DAKOTA code suite contains a large collection of algorithms to conduct optimization, uncertainty quantification (UQ), and sensitivity analysis. The external coupling uses shell scripting commands to post-process MPM output responses that are input to DAKOTA. Figure 4.2 shows a generalized schematic diagram showing the information flow in the MPM-DAKOTA coupling.
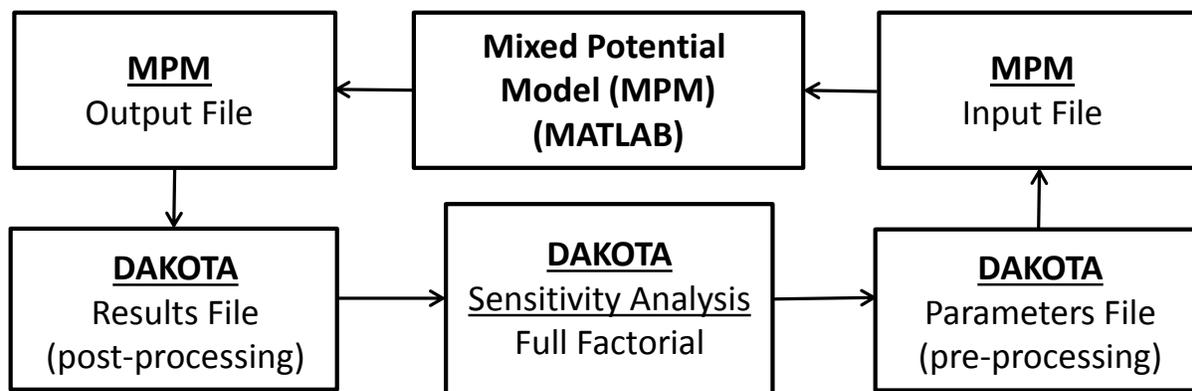
Figure 4.2. Schematic diagram depicting the information flow for the MPM (Matlab) – DAKOTA coupling.

The analysis was done using the multidimensional parameter (full-factorial) evaluation in DAKOTA where each input variable is partitioned in equally-spaced intervals for their continuous value ranges within their upper and lower bounds. The number of partitions is set to generate four data points (four DAKOTA-MPM iterations) for each input value. The MPM model inputs to be perturbed at each DAKOTA-MPM iteration are temperature, dose rate, and initial CO_3^- and O_2 concentrations. This partitioning coverage equals to four input evaluations for each of the four input parameters resulting in 4^4 or 256 DAKOTA-MPM iteration runs. The output responses to be sampled are the concentrations UO_2^{++}, UCO_3^{--}, and H_2O_2. The UO_2^{++} and UCO_3^{--} are considered as the total concentration of U released into the system. The bounds for the input variables (Table 4.1) were based on reasonable ranges of possible geochemical conditions in the disposal gallery and fuel surface but spaced a few orders of magnitude to capture a wide series of values. The sampled output responses are taken at 1097 years and at a surface distance of 31.6 microns. It should be noted that other sampled times and surface distances can be considered in the response sampling in the SA. The effect of considering uncertainties and other sampling strategies for the considered input factors was not evaluated in this SA and it may well be a topic of future work.

Table 4.1. Bounding constrains for input variables for DAKOTA.

Constraint[*]	Temperature (K)	Dose Rate (J/kg)/s	$[CO_3^-]$ (moles/m^3)	$[O_2]$ (moles/m^3)
Lower Bounds	298.15	0.001	0.01	1.0E-05
Upper Bounds	363.15	0.5	1.5	1.0E-02

[*] Partitioning between these bounding limits was set to produce four data points. For example, the resulting temperature values for this bounded range are 298.15, 319.8, 341.5, and 363.15 K.

Table 4.2. Simple DAKOTA Correlation Matrix among all inputs and outputs

Inputs/Outputs	Temperature (K)	Dose Rate ((J/kg)/s)	$[CO_3^{--}]$ (mol/m^3)	$[O_2]$ (mol/m^3)	$[UO_2^{++}]$ (mol/m^3)	$[UCO_3^{--}]$ (mol/m^3)	$[H_2O_2]$ (mol/m^3)
Temperature (K)	1.00E+00	-	-	-	-	-	-
Dose Rate ((J/kg)/s)	0.00E+00	1.00E+00	-	-	-	-	-
$[CO_3^{--}]$ (mol/m^3)	-4.24E-22	0.00E+00	1.00E+00	-	-	-	-
$[O_2]$ (mol/m^3)	0.00E+00	8.47E-22	8.47E-21	1.00E+00	-	-	-
$[UO_2^{++}]$ (mol/m^3)	6.79E-01	5.13E-01	-4.81E-02	3.57E-01	1.00E+00	-	-
$[UCO_3^{--}]$ (mol/m^3)	-6.39E-01	3.23E-01	3.23E-01	8.01E-02	-3.75E-01	1.00E+00	-
$[H_2O_2]$ (mol/m^3)	-5.64E-01	6.56E-01	-4.37E-02	1.67E-02	-1.20E-01	7.16E-01	1.00E+00

4.4   Discussion and Future Work

DAKOTA provide a matrix table of the outputs (256 MPM code runs) for all the sampled iterations. It also provides a simple correlation matrix given in Table 4.2. This correlation matrix is useful in delineating the parameter sensitivities to the input factors. Figures 4.3 and 4.4 show the resulting total U and H_2O_2 concentrations profiles as a function of temperature for the lower and upper bounds of initial CO_3^{--} and O_2 concentrations at the specified dose rates. Note that the main influence in U and H_2O_2 concentration profiles is the dose rate. For example, U and H_2O_2 concentrations are increased by about the same order of magnitude as the dose rate for the same initial CO_3^{--} and O_2 concentrations. The effects from the latter two have some influence, particularly O_2 concentration, but not as large as the dose rate. These observations lead to the conclusion that dose rates from radiolysis need to be closely integrated with the H_2O_2 production rates which in turn determines the U releases. However, conditions at the fuel surface and surrounding are expected to be largely reduced and the SA should consider lower O_2 concentrations. Still, the relative magnitude of the effect of CO_3^{--} and O_2 concentrations is not expected to greatly surpass that of the dose rate. The figures also show an overlapping band of the U and H_2O_2 concentration profiles at dose rates within approximately less than an order of magnitude for dose rates ranging from 0.167 to 0.5 (J/kg)/s.

This type of analysis is very useful in investigating model sensitivities but it can also be utilized for model verification and testing. Further, it provides the groundwork for expanding the analysis with other SA strategies towards the analysis of model uncertainties. The coupling of the MPM with the DAKOTA toolkit offers access to a large set of tools for optimization (e.g., regression analysis) and uncertainty quantification. For FY14, the analysis will be expanded to:

- Evaluate sampling strategies (e.g., Latin Hypercube Sampling or LHS) other than bounding constrains as done in a full-factorial design,
- Consider time dependencies in key variables to used fuel degradation such as radiolytic processes,
- Examine model responses to specific host media aqueous chemistry and related input uncertainties.
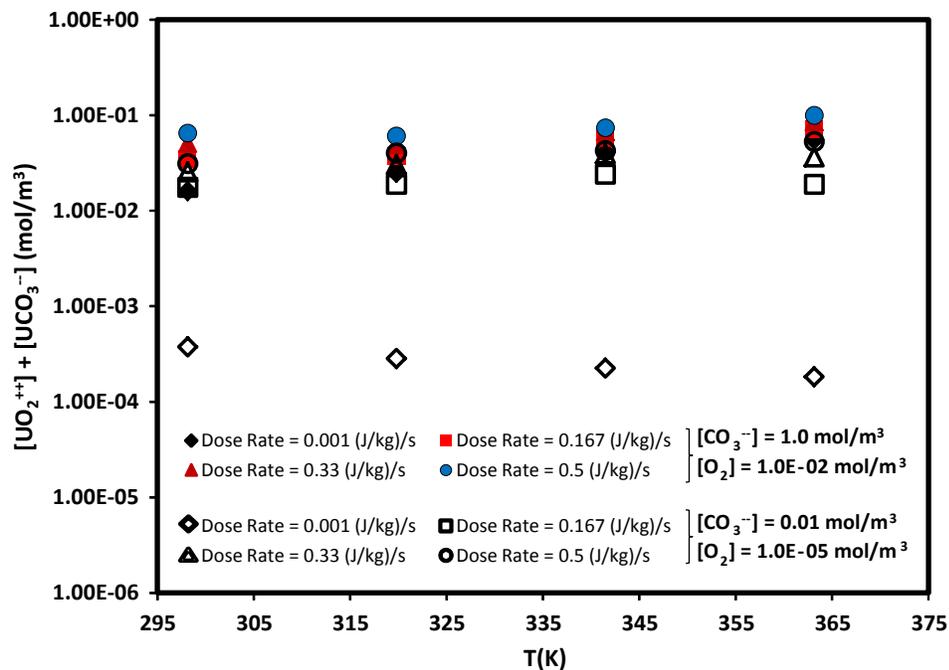
Figure 4.3. Concentration profile of U aqueous species computed by the MPM as a function of temperature, dose rate, CO_3^{--}, and O_2 concentrations.
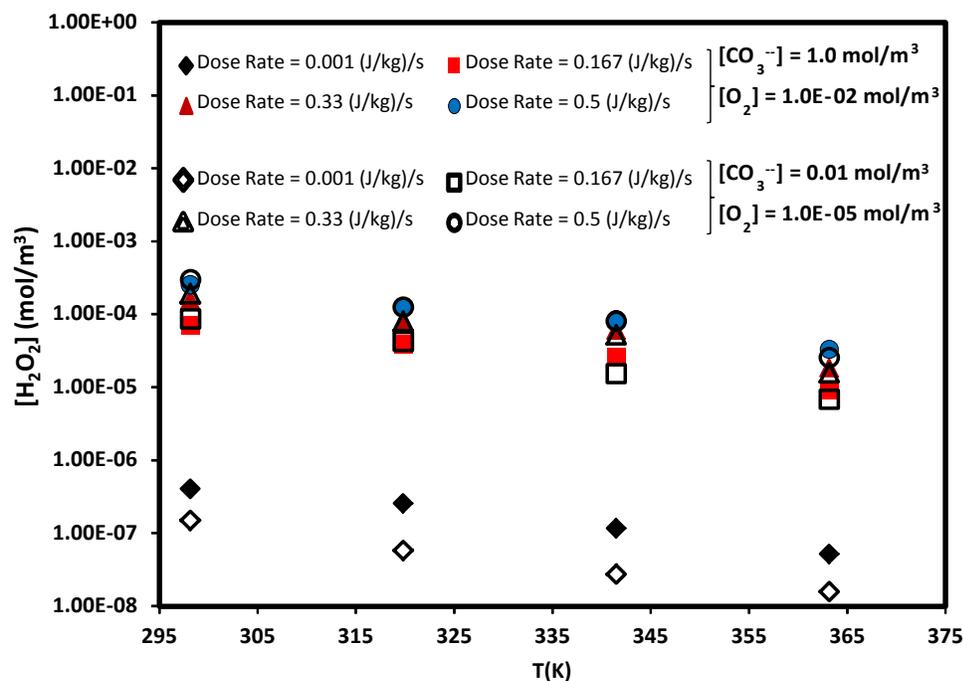
Figure 4.4. Concentration profile of H_2O_2 computed by the MPM as a function of temperature, dose rate, CO_3^{--}, and O_2 concentrations.

5.   CONCLUSIONS

The G_{cond} is calculated in the RM and handed off to the MPM, where it is used to calculate the spatial generation of $[H_2O_2]$ from the dose rate as affected by surface reactions with the fuel and diffusion. G_{cond} is defined as the steady state generation value (moles of species (i) per alpha energy deposited) averaged over the 35 μm alpha penetration depth adjacent to the fuel surface. It is useful though not entirely necessary that the total deposition depths are the same in the RM and MPM, and it may be valuable that they be discretized the same. This is because the H_2O_2 concentration is calculated at much shorter time scales within the RM compared to the MPM. When using the discretized case of the RM, G_{cond} becomes proportional to the diffusive flux of species (*i*) exiting the alpha penetration zone.

The coupling of the RM and MPM requires running the models separately because the MPM uses time steps on the order of years, while the RM uses time steps on the order of seconds. An alternative to actively linking the RM and MPM is to develop an analytic expression that determines G_{cond} for a given set of conditions. The analytic expression would be coded directly into MATLAB and run with the MPM. However, this does not establish a true working link and the full capabilities of RM would be lost. Furthermore, the determination of analytical expressions for the full ranges of environments may prove to be onerous.

Interfacing of the MPM with the DAKOTA code suite has been developed to conduct sensitivity analyses. The results of this analysis provide the necessary tools to feasibly evaluate model behavior in response to the variability of multiple parameters which is important to the determination of PA inputs. Such interfacing also provides a fertile ground to expand SA to other parameters and to conduct uncertainty quantification or parameter optimization if

necessary. Future work includes the consideration of other sampling strategies and the analysis of time dependencies (e.g., how a precipitating solid affects U concentration files with time).

Currently the only radiolytic species in the MPM is H_2O_2. Other radiolytic species will need to be added to the MPM for it to be applicable to the full range of relevant geologic and EBS environments. The radiolytic species that need to be added can be determined by sensitivity runs using the RM for the range of relevant solution compositions for sites of interest. The focus of RM sensitivity runs should be on radiolytically active species (for example: Cl^-, Br^-, NO_3^-, CO_3^{2-}, SO_4^{2-}) and should determine concentration thresholds above which radiolytic species other than H_2O_2 significantly impact fuel oxidation become important.

6.   REFERENCES (Sections 1 through 5)

BSC (2004). CSNF Waste Form Degradation: Summary Abstraction, ANL-EBS-MD-000015 REV02.

Christensen, H., Sunder, S. (1996). An evaluation of water layer thickness effective in oxidation of UO$_2$ fuel due to radiolysis of water, *Journal of Nuclear Materials* 238: 70-77.

Christensen, H., Sunder. S. (2000). Current state of knowledge of water radiolysis effects on spent nuclear fuel corrosion, Nuclear Technology, 131, p. 102-123.

Clayton D., Freeze, G., Hadgu, T., Hardin, E., Lee, J., Prouty, J., Rogers, R., Nutt, W. M., Birkholzer, J., Liu, H.H., Zheng, L., and Chu, S. (2011). Generic Disposal System Modeling—Fiscal Year 2011 Progress Report, FCRD-USED-2011-000184, pp. 443.

Cunnane, J.C., Fortner, J.A, and Finch, R. (2003). The behavior of light water reactor fuel after the cladding is breached under unsaturated test conditions, MRS Symposium Proceedings,757, p. 385–392.

De Pablo, J., Serrano-Purroy, D., Gonzalez-Robles, E., Clarens, F., Martinez-Esparza, A., Wegen, D. H., Casas, I., Christiansen, B., Glatz, J.-P., Gimenez, J. (2009). Effect of HBS Structure in Fast Release Fraction of 48 GWd/tU PWR Fuel, *Mater. Res. Soc. Symp. Proc.*, 1193, 613 doi:10.1557/PROC-1193-613.

Ferry, C., Poinssot, C., Cappelaere, C., Desgranges, L., Jégou, C., Miserque, F., Piron, J.P., Roudil, and D., Gras, J-M. (2006). Specific Outcomes of the Research on the Spent Fuel Long-Term Evolution in Interim Dry Storage and Deep Geological Disposal, Journal of Nuclear Materials, 352, p. 246-253.

Freeze, G., Mariner, P., Houseworth, J., Cunnane, J., and F. Caporuscio, F. (2010). *Used Fuel Disposition Campaign Features, Events, and Processes (FEPs): FY10 Progress Report*, August 2010.

Freeze, G. and Vaughn, P. (2012). Performance Assessment Framework Requirements for Advanced Disposal System Modeling, FCRD-UFD-2012-000227 (M3FT-12SN0808062), U.S. Department of Energy, Office of Nuclear Energy, Used Fuel Disposition Campaign, Washington, D.C.

Freeze, G., Gardner, P., Vaughn, P., Sevougian, S. D., Mariner, P., Mousseau, V. (2013). Performance Assessment Modeling of a Generic Salt Disposal System: Annotated Outline, DOE-NE Fuel Cycle R&D, FCRD-UFD-2013-000219, SAND2013-6183P, 21 pp.

Helton, J. C., Johnson, J. D., Sallaberry, C. J., and Storlie, C. B. (2006). Survey of sampling-based methods for uncertainty and sensitivity analysis: Reliability Engineering and System Safety, v. 91, no. 10, p. 1175-1209.

Helton, J. C., Johnson, J. D., Sallaberry, C. J., and Storlie, C. B. (2006). Survey of sampling-based methods for uncertainty and sensitivity analysis: Reliability Engineering and System Safety, v. 91, no. 10, p. 1175-1209.

Jerden, J., Frey, K., Cruse, T., and Ebert, W. (2012). *Waste Form Degradation Model Status Report: Electrochemical Model for Used Fuel Matrix Degradation Rate*. FCRD-UFD-2012-000169.

Jerden, J., Frey, K., Cruse, T., and Ebert, W. (2013). *Waste Form Degradation Model Status Report: ANL Mixed Potential Model, Version 1. Archive*. FCRD-UFD-2013-000057.

Johnson, L., Ferry, C., Poinssot, C., and Lovera, P. (2005). Spent fuel radionuclide source term model for assessing spent fuel performance in geological disposal. Part I: Assessment of the Instant Release Fraction, Journal of Nuclear Materials, 346, p. 66-77.

Johnson, L., Gunther-Leopold, I., Kobler Waldis, J., Linder, H. P., Low, J., Cui, D., Ekeroth, E. Spahiu, K., Evins, L. Z. (2012). Rapid aqueous release of fission products from high burn-up LWR fuel: Experimental results and correlations with fission gas release, Journal of Nuclear Materials, 420, p. 54-62.

Jové Colón, C. F., Greathouse, J. A., Teich-McGoldrick, S., Cygan, R. T., Hadgu, T., Bean, J. E., Martinez, M. J., Hopkins, P. L., Argüello, J. G., Hansen, F. D., Caporuscio, F. A., Cheshire, M., Levy, S. S., McCarney, M. K., Greenberg, H. R., Wolery, T. J., Sutton, M., Rutqvist, J., Steefel, C. I., Birkholzer, J., Liu, H. H., Davis, J. A., Tinnacher, R., Bourg, I., Holmboe, M., and Galindez, J. (2012). Evaluation of Generic EBS Design Concepts and Process Models: Implications to EBS Design Optimization, SAND2012-5083 P, 250 pp.

King, F. and Kolar, M. (1999). Mathematical Implementation of the Mixed-Potential Model of Fuel Dissolution Model Version MPM-V1.0, Ontario Hydro, Nuclear Waste Management Division Report No. 06819-REP-01200-10005 R00.

King, F. and Kolar, M. (2002). Validation of the Mixed-Potential Model for Used Fuel Dissolution Against Experimental Data, Ontario Hydro, Nuclear Waste Management Division Report No. 06819-REP-01200-10077-R00.

King, F. and Kolar, M. (2003). The Mixed-Potential Model for UO2 Dissolution MPM Versions V1.3 and V1.4, Ontario Hydro, Nuclear Waste Management Division Report No. 06819-REP-01200-10104 R00.

Pastina, B. and LaVerne, J. A. (2001). Effect of Molecular Hydrogen on Hydrogen Peroxide in Water Radiolysis, *Journal of Physical Chemistry* A105: 9316-9322.

Poinssot, C. Ferry, C. M. Kelm, B. Grambow, A. Martinez, A., Johnson, L., Andriamoloolona, Z., Bruno, J., Cachoir, C., Cavedon, J.M., Christensen, H., Corbel, C., Jegou, C., Lemmens, K., Loida, A., Lovera, P., Miserque, F. de Pablo, J., Poulesquen, A., Quinones, J. Rondinella, V., Spahiu, K., and D. H. Wegen, (2004). S*pent Fuel Stability under Repository Conditions: Final Report of the European Project*, European Commission, 5th EURATOM FRAMEWORK PROGRAMME, 1998-2002.

Poinssot, C., Ferry, C., Lovera, P., Jégou, C., Gras, J-M. (2005). Spent fuel radionuclide source term model for assessing spent fuel performance in geological disposal. Part II: Matrix alteration model and global performance, Journal of Nuclear Materials, 346, p. 66-77.

Radulescu, G. (2011). *Radiation Transport Evaluations for Repository Science*, ORNL/LTR-2011/294, LETTER REPORT, Oak Ridge National Laboratory, August, 2011.

Roudil, D., Jegou, C., Broudic, V. Muzeau, B., Peuget, S., and Deschanels, X. (2007). Gap and grain boundaries inventories from pressurized water reactor spent fuels, Journal of Nuclear Materials, 362, p. 411-415.

Sassani, D.C., Jové Colón, J. C., Weck, P., Jerden, J. L., Jr., Frey, K. E., Cruse, T., Ebert, W. L., Buck, E. C., Wittman, R. S., Skomurski, F. N., Cantrell, K. J., McNamara, B. K., and Soderquist, C. Z. (2012). *Integration of EBS Models with Generic Disposal System Models*, U.S. Department of Energy, Used Fuel Disposition Campaign milestone report: M2FT-12SN0806062, September, 7 2012

Sassani, D. C., Jové-Colón, C. F., and Weck, P. F. (2013). "Integrating Used Fuel Degradation Models into Generic Performance Assessment" for the *ANS 2013 International High-level Radioactive Waste Management Conference*, April 28 – May 3, 2013, Albuquerque, NM.

Saltelli, A. (2009). Special issue: Sensitivity Analysis: Reliability Engineering and System Safety, v. 94, no. 7, p. 1133-1134.

Saltelli, A., Ratto, M., Tarantola, S., and Campolongo, F. (2005) Sensitivity analysis for chemical models: Chemical Reviews, v. 105, no. 7, p. 2811-2827.

- (2012). Update 1 of: Sensitivity Analysis for Chemical Models: Chemical Reviews, v. 112, p. Pr1-Pr21.

Saltelli, A., Tarantola, S., and Campolongo, F. (2000). Sensitivity analysis as an ingredient of modeling: Statistical Science, v. 15, no. 4, p. 377-395.

Saltelli, A., Tarantola, S., Campolongo, F., and Ratto, M. (2004). Sensitivity analysis in practice: a guide to assessing scientific models, John Wiley & Sons.

Serrano-Purroy, D., Clarens, F., Gonzalez-Robles, E., Glatz, J.-P., Wegen, D. H., De Pablo, J., Casas, I., Gimenez, J., Martinez-Esparza, A. (2012). Instant release fraction and matrix release of high burn-up UO_2 spent nuclear fuel: Effect of high burn-up structure and leaching solution composition, Journal of Nuclear Materials, 427, p. 249-258.

Shoesmith, D.W., Kolar, M., and King, F. (2003). A Mixed-Potential Model to Predict Fuel (Uranium Dioxide) Corrosion Within a Failed Nuclear Waste Container, *Corrosion, 59*, 802-816.

Une, K., Kashibe, S., 1996, Corrosion behavior of irradiated oxide fuel pellets in high temperature water, Journal of Nuclear Materials, 232, p. 240-247.

Weck, P. F., Kim, E., Jové Colón, C. F., and Sassani, D. C., 2013, On the role of strong electron correlations in the surface properties and chemistry of uranium dioxide, DOI: 10.1039/C3DT32536A.

Wittman, R. S. and Buck, E. C. (2012). Sensitivity of UO_2 stability in a reducing environment on radiolysis model parameters, *Materials Research Society Proceedings Symposium*, 1444, 3-8.

Yu, L., Weetjens, E., Vietor, T., and Hart, J. (2010). Integration of TIMODAZ within the safety case and recommendations for repository design (D14), Final Report of WP6, European Commission Euratom Research and Training Programme on Nuclear Energy, 48 pp.

7. ANL MIXED POTENTIAL MODEL WITH EXPERIMENTAL RESULTS: IMPLEMENTATION OF NOBLE METAL PARTICLE CATALYSIS MODULE

7.1 Objectives and Context

The high level goal of this work is to develop a fundamentals-based computational tool for predicting the degradation rate of used fuel and establish a scientific basis for the radionuclide source terms used in the UFD generic performance assessment model. The approach has been to implement, optimize and extend an existing and well-tested corrosion model that is based on electrochemical mixed potential theory (the Canadian mixed potential model - MPM) to specific fuel degradation processes of interest and to couple this MPM with an equally robust radiolysis model (RM) (for conceptual discussion of model coupling see Buck et al., 2013). The coupled MPM – RM process model is being combined with a statistical treatment of radionuclide instant release fractions (IRF) to form the Fuel Degradation Model (FDM). Thus, the FDM consists of three primary components:

- The *Radiolysis Module (RM)*, which provides a rigorous treatment of chemical processes associated with the absorption of ionizing radiation near the surface of the exposed fuel. Supplies concentrations used to calculate fuel matrix degradation.
- The *Mixed Potential Module (MPM)*, which provides the rate of fuel matrix degradation (accounts for both oxidative and chemical dissolution).
- The *Instant Release Fraction (IRF)*, which provides the masses of key radionuclides that will be released from the fuel promptly after the time of exposure (release rate is more rapid than predicted matrix degradation rate).

The relationship between the FDM and generic performance assessment models is summarized in Figure 7.1. More details on the information flows involved in the coupling of the process modules is shown in Figure 4.1.

System Level Model *(Performance Assessment)*
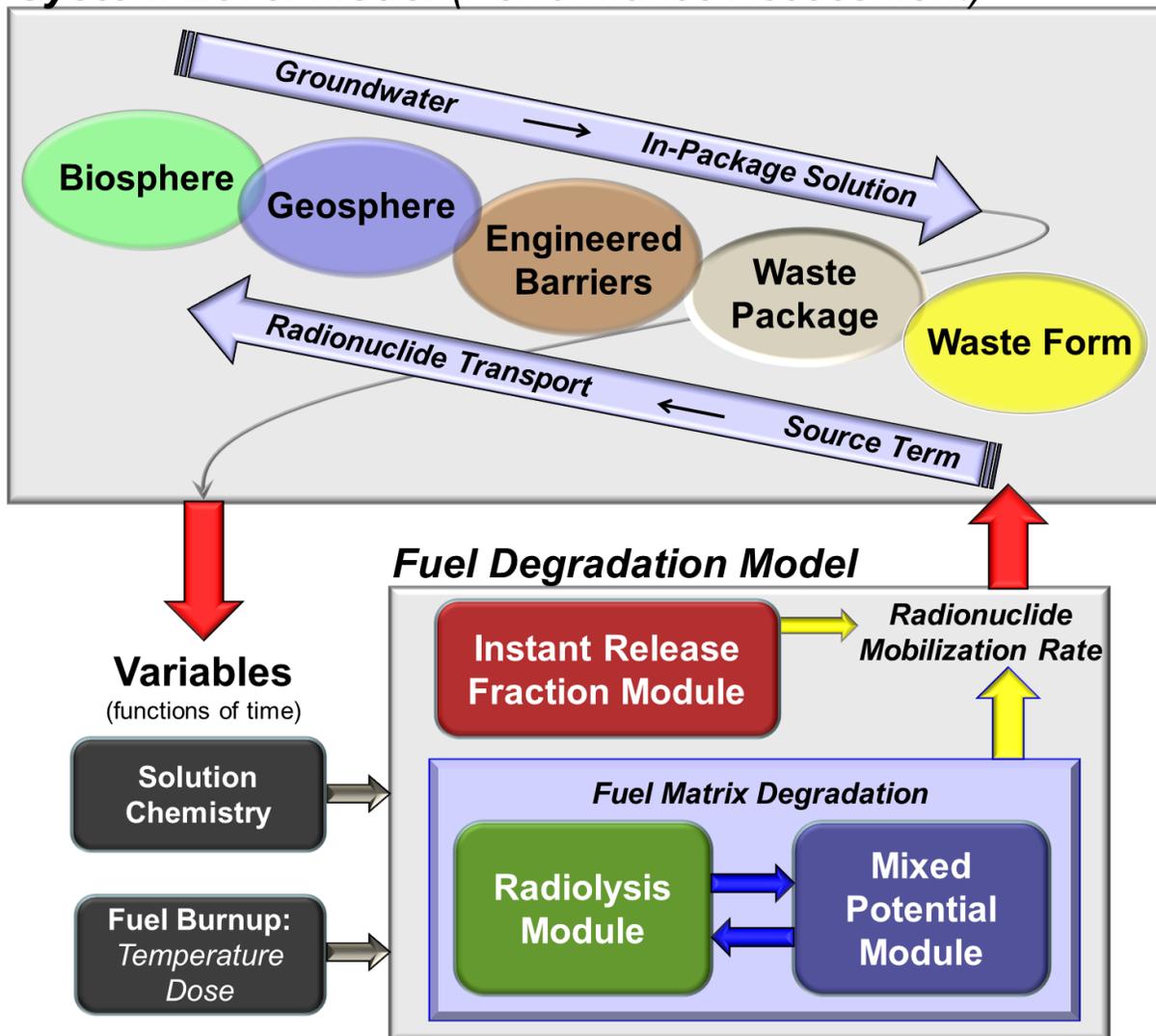
Figure 7.1. Summary information flow diagram showing the relationship of the FDM to the system-level model and sub-models (modules) comprising the FDM.

Within the context of the higher-level project goal discussed above, the two main objectives of the work presented in this report are to: (1) develop and implement a new section of code within the MPM that accounts for the catalyzed oxidation of dissolved hydrogen at the fuel surface, (2) develop a strategy for coupling the RM and MPM and (3) perform a suit of electrochemical experiments to inform and test the mixed potential module of the FDM.

7.2   Mixed Potential Module and Surface Catalysis of Redox Reactions

It has been shown experimentally that the noble metal-bearing, fission product alloy phase (epsilon metal) in used oxide fuel can catalyze redox reactions in aqueous solutions and thus

influence the rate of oxidative dissolution of the fuel matrix (e.g., Broczkowski et al., 2005, Shoesmith, 2008, Trummer, et al., 2009, Cui et al., 2010). As this process may strongly influence the degradation rate of used fuel in a geologic repository, it has been incorporated into the Mixed Potential Module (MPM) of the Fuel Degradation Model. The new module affords two important capabilities:

- Evaluation of the catalytic effects of the noble metal bearing, fission product alloy phase (Noble Metal Particles - NMP) on reactions affecting fuel matrix degradation.
- Evaluation of the long-term importance of H_2 oxidation in protecting used fuel from oxidative dissolution in disposal environments of interest.

The details of the implementation of the MPM are covered in Jerden et al., 2012 and Jerden et al., 2013, however some background is given here to provide context for the implementation of the new module.

The MPM is adapted from the Canadian-mixed potential model for UO_2 fuel dissolution (King and Kolar, 1999, King and Kolar, 2003, Shoesmith et.al., 2003) and was implemented using the numerical computing environment and programming language MATLAB (Jerden et al., 2013). The MPM is a 1-dimensional reaction-diffusion model that accounts for the following processes:

- Rate of oxidative dissolution of the fuel matrix as determined by interfacial redox reaction kinetics (quantified as a function of the corrosion potential) occurring at the multiphase fuel surface (phases include UO_2 and the noble metal fission product alloy phase (often called the epsilon phase).

- Chemical or solubility-based dissolution of the fuel matrix.

- Complexation of dissolved uranium by carbonate near the fuel surface and in the bulk solution.

- Production of hydrogen peroxide (the dominant fuel oxidant in anoxic repository environments) by alpha-radiolysis.

- Diffusion of reactants and products in the groundwater towards and away from the reacting fuel surface.

- Precipitation and dissolution of a U–bearing corrosion product layer on the fuel surface.

- Diffusion of reactants and products through the porous and tortuous corrosion product layer covering the reacting fuel surface.

- Arrhenius-type temperature dependence for all interfacial and bulk reactions.

These key processes that are accounted for in the MPM are summarized in Figure 7.2.
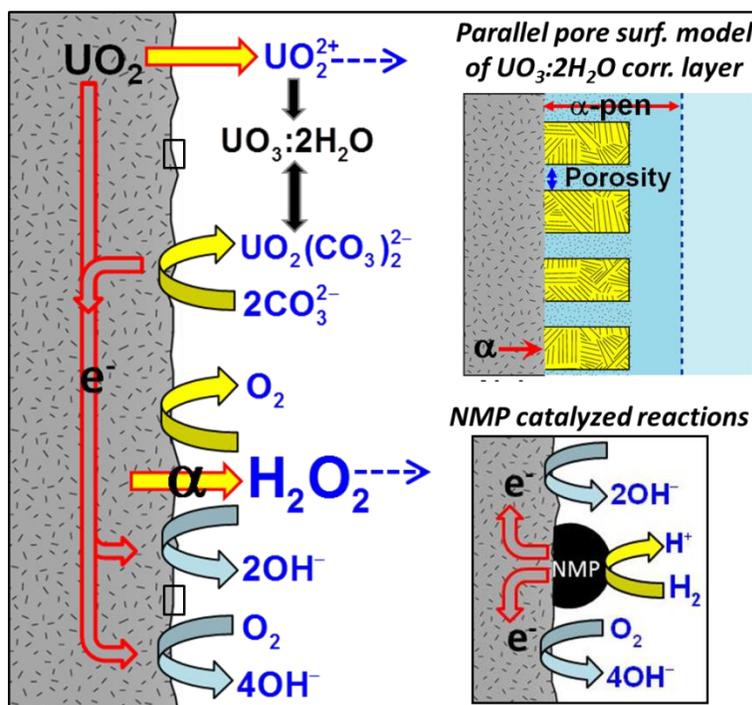
Figure 7.2. Key processes accounted for in the MPM. The corrosion layer is modeled as a set of parallel pores with fixed porosity and tortuosity. The noble metal particles (NMP) are modeled as reactive separate surface domain with its own set of surface reactions.

Calculating the alpha dose rate (and thus H_2O_2 concentration) for corroding UO_2 fuel is complicated by the effects of U(VI) corrosion products (modeled as schoepite, $UO_3 \bullet 2H_2O$ in MPM). The U(VI) corrosion product layer has three effects on the rate of fuel degradation predicted by the MPM:

- Slows rate of oxidative dissolution by decreasing the reactive surface area of the fuel (blocking or masking reaction sites).

- Slows rate of oxidative dissolution by blocking alpha-particles from interacting with water and producing radiolytic oxidants (decreases total moles H_2O_2 produced near fuel surface). The magnitude of this effect is proportional to surface coverage of corrosion layer.

- Corrosion layer can slow the rate of oxidative dissolution by slowing the rate of diffusion of oxidants to the fuel surface: U(VI) layer is a tortuous porous mass of crystals (simulated in MPM by a parallel pores with constant tortuosity).

All three of these effects are modeled in the MPM by a radiolysis "sub-routine" that was recoded from the original Canadian mixed potential model (for details see Jerden et al., 2013). As in Canadian model, alpha-particles are currently assumed to have a constant energy of 5.3 MeV and a solution penetration distance (α_{PEN}) of 35 μm in the current MPM. The modeler can set the penetration distance over the range of $\alpha_{PEN} = 45$ micrometers for ~6.0 MeV alpha-particles down to $\alpha_{PEN} = 10$ μm for ~2.3 MeV particles (King and Kolar, 1999), and the default generation value

for hydrogen peroxide produced by alpha-radiolysis is assumed to be 1.021E-4 mole/Gy/m^3 (Christensen and Sunder, 2000). Scoping work to take into account the spatial variation of dose and radiolysis has been completed and will likely be implemented in a revision of the coupled RM and MPM.

In the MPM, the fuel degradation rate is calculated using mixed potential theory to account for all relevant redox reactions at the fuel surface, including those involving oxidants produced by solution radiolysis; radiolytic processes are quantified in the RM of the FDM. Because the MPM is based on fundamental chemical and electrochemical principles, it is flexible enough to be applied to the full range of repository environments as well as shorter-term storage scenarios being considered as part of the UFD campaign. The current module was developed to model granitic systems and includes reactions tracking H_2, O_2, and H_2O_2, but reactions involving species important in other disposal systems of interest can be readily incorporated.

The process of interest for this report, and the experimental approach we have used to study it, are summarized in Figure 7.3. The process involves the catalyzed oxidation of hydrogen on the NMP surface and the transfer of electrons from NMP sites to the fuel matrix. The electrical coupling between NMP and fuel grains sets up a galvanic link that effectively protects the fuel from oxidative dissolution. That is, electrons supplied by hydrogen oxidation effectively counteract the oxidation of U(IV) to U(VI) by hydrogen peroxide or other oxidants (Figure 7.3).

The new sections of code added to the MPM (Appendix 1) to quantify reactions involving H_2 further extend the model's flexibility and versatility by accounting for the following:

- Oxidation of dissolved H_2 and H_2O_2 catalyzed by NMP at the used fuel/solution interface.

- The surface area of NMPs, which are treated as a separate electrochemical domain (phase) at the used fuel/solution interface. The "size" of the NMP domain (relative to the fuel) is specified by the user in terms of a surface coverage and is electrically linked with the UO_2 matrix by a user adjustable resistance. This will allow the effects of corrosion and sorption on the catalytic efficiency of the NMPs to be taken into account.
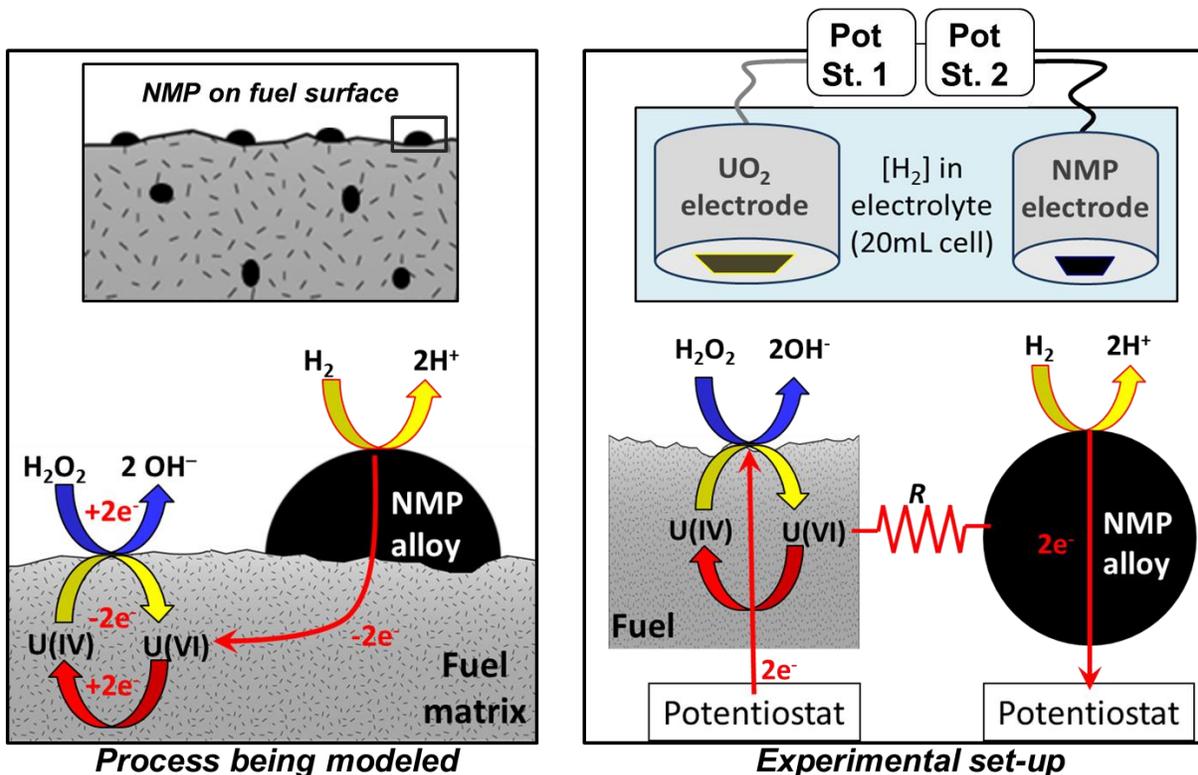
Figure 7.3. Schematic diagram showing flow of electrons for surface catalyzed oxidation of hydrogen. The diagrams on left shows the processes being implemented as part of the MPM. The diagrams on the right show a simplified conceptual view of the processes and set-up that was used to perform the electrochemical experiments (experimental results presented below).

7.3   Implementation of Noble Metal Particle Catalyzed Redox Reactions within the Mixed Potential Module

The lines of MATLAB code used to implement the surface catalysis of redox reactions are shown in Appendix 1. As stated above and shown schematically in Figure 7.3, the catalyzed reaction occur on separate NMP domains distributed across the fuel surface with the surface coverage and resistance relative to the fuel matrix set by the modeler. The key reactions accounted for in the MPM are shown in Table 3.1. This table also identifies the four surface catalyzed reactions associated with the NMP domain.

To add the reactions catalyzed on the NMP surface (top four reactions in Table 3.1) the parameter database for the MPM was expanded and updated with appropriate charge transfer coefficients, rate constants, standard potentials, diffusion coefficients and activation energies for temperature dependencies for the species/reactions of interest. The parameter values used, which are shown in Appendix 1, were estimated based on comparisons with similar redox reactions discussed in King and Kolar, 1999, King and Kolar, 2003, Shoesmith et.al., 2003. A critical review, based on up-to-date literature, of all parameters and constants used in the MPM is recommended; however, experiments are also needed to test model results and reduce parameter uncertainties.

To test the implementation of the NMP domain catalysis process, a number of new MPM runs were performed. The model inputs for these runs are listed in Table 7.1. Results are shown in Figures 7.4 – 7.7 and discussed below.

Table 7.1. Parameter and variable inputs used for MPM runs presented below.

Inputs specific to NMP domain	
Surface coverage of NMP	1% of fuel surface
Resistance between UO_2 and NMP domains	1.0E-3 V/Amp
Concentration of dissolved H_2	zero – 1 moles/L
Other user-defined inputs and parameters	
Length of model diffusion grid	5 mm
Number of calculation nodes (points) in diffusion grid	200
Duration of simulation	10,000 years
Alpha-particle penetration depth	35 micrometers
Generation value for H_2O_2	1.021E-4 mole/Gy/m^3
Porosity factor for corrosion layer	50%
tortuosity factor for corrosion layer	0.01
Variables	
Temperature	25°C (constant)
Dose rate	0.1 Gy unless otherwise noted
Environmental concentration of O_2	1.0E-9 moles/L
Environmental concentrations of carbonate and iron	Zero

Figure 7.4 shows examples of time-dependent fuel corrosion potentials and corresponding degradation rates predicted by the MPM for five different dissolved hydrogen concentrations with 1% NMP at the fuel surface. The model predicts that when hydrogen concentrations greater than 1.0E-2 moles/L are present at the reacting fuel surface the corrosion potential drops to less than -0.3 Volts relative to the saturated calomel electrode (V_{SCE}). This corresponds to a fuel degradation rate of less than 1.0E-5 g/m^2/year, which approaches the rate of non-oxidative, diffusion-driven, chemical dissolution of the fuel. Therefore, according to the MPM, concentrations around 1.0E-2 molar hydrogen can drive the surface potential of the fuel to below the threshold for oxidative dissolution. This is consistent with Shoesmith, 2008.

The bottom plot in Figure 7.4 highlights the effect that a corrosion layer has on the fuel degradation rate. For the case with no dissolved hydrogen (yellow), the corrosion layer is predicted to begin to form around 2 years into the simulation. The layer blocks half of the fuel surface from emitting alpha radiation into the near-surface solution, thus decreasing (by half) the amount of hydrogen peroxide (the dominant fuel oxidant) produced within a given time step. The alpha emission to the solution is decreased by a half because the porosity of the corrosion layer is assumed to be 50%, that is 50% of the surface is masked by the alpha blocking corrosion phase. The layer also moderates diffusion due to pore tortuosity. These two effects cause the transitory decrease in fuel degradation rate seen between 2 – 200 years of the simulation. Beyond 200 years, the layer thickness exceeds the alpha penetration depth and the generation and diffusion rates reach steady state.

The bottom plot of Figure 7.4 also shows that even at modest hydrogen concentrations higher than 1.0E-4 mole/L the corrosion potential and corresponding degradation rates are low enough to delay the onset of corrosion layer precipitation to beyond 1500 years. At 1.0E-3 moles/L dissolved hydrogen the fuel degradation rate is too slow to saturate the solution with respect to the $UO_3:2H_2O$ corrosion phase (diffusion occurs faster than generation) so no layer forms.

Figure 7.5 shows how the concentration of hydrogen peroxide produced by alpha radiolysis varies as a function of distance away from the fuel surface. Each point in the plot represents an individual model calculation in time and space. The competing processes that determine the shapes and magnitudes of these concentration profiles are:

- H_2O_2 is continuously produced within the first 35 micrometers of the fuel surface (energy deposition is presently modeled to be uniform within this zone).

- H_2O_2 diffuses towards or away from the fuel surface depending on the concentration provide, and diffusion rates near the surface will be moderated by the corrosion layer.

- H_2O_2 concentration at environmental boundary (5 mm from fuel) is zero.

- H_2O_2 is consumed (dominantly) at the fuel surface by the following coupled half-reactions:

  o $H_2O_2 + 2e^- \rightarrow 2OH^-$

  o $UO_2 \rightarrow UO_2^{2+} + 2e^-$

- H_2O_2 consumption rate at the fuel surface increases significantly when the NMP catalyzed hydrogen oxidation reaction is taken into account and $[H_2] \geq 1.0E-4$ mole/L (left side of Figure 7.5):

  o $H_2 + 2OH^- \rightarrow 2H_2O + 2e^-$

The increase in the rate of hydrogen peroxide consumption at the fuel surface when rapid (NMP-catalyzed) hydrogen oxidation is occurring is caused by the kinetic balance of the associated redox reactions (shown in bullets above). Specifically, the large anodic current associated with the hydrogen oxidation reactions drives up the rate of the dominant cathodic reaction involving hydrogen peroxide reduction. Therefore, when enough hydrogen is present at a fuel surface bearing active NMP sites, hydrogen peroxide is rapidly depleted thus decreasing the rate of oxidative dissolution. That this process of hydrogen oxidation essentially protects the fuel from degradation is evident in Figure 7.6, which shows the current densities of the key reactions for a

range of hydrogen concentrations. The anodic half-reactions are shown on the top plot of Figure 7.6, while the cathodic half-reactions are shown on the bottom plot.

As the concentration of hydrogen at the fuel surface is increased to $\geq$ 1.0E-3 mole/L the anodic current density of the hydrogen oxidation reaction increases from near zero to around 6.6E-5 Amps/m^2, while the current density of fuel oxidation reaction decreases from around 4.7E-5 Amps/m^2 down to around zero. The corresponding hydrogen peroxide reduction (cathodic) current density increases from -5.3E-5 Amps/m^2 up to -6.3E-5 Amps/m^2 at hydrogen concentrations $\geq$ 1.0E-4 mole/L. Also as shown on Figure 7.6, the roles of hydrogen peroxide oxidation (dark green, top) and oxygen reduction (light blue, bottom plot) are less important to the overall kinetic balance for the conditions under investigation.

Figure 7.7 shows how increasing the hydrogen concentration at the fuel surface influences the fuel corrosion potential and degradation rate for two typical dose rates. These plots are consistent with the observation that once the dissolved hydrogen reaches 0.01 mole/L (with 1% surface coverage of NMP) the corrosion potential of the fuel drops below the threshold for oxidative dissolution and the fuel degradation rate is determined by diffusion-driven, chemical dissolution (~1.0E-7 g/m^2/year).
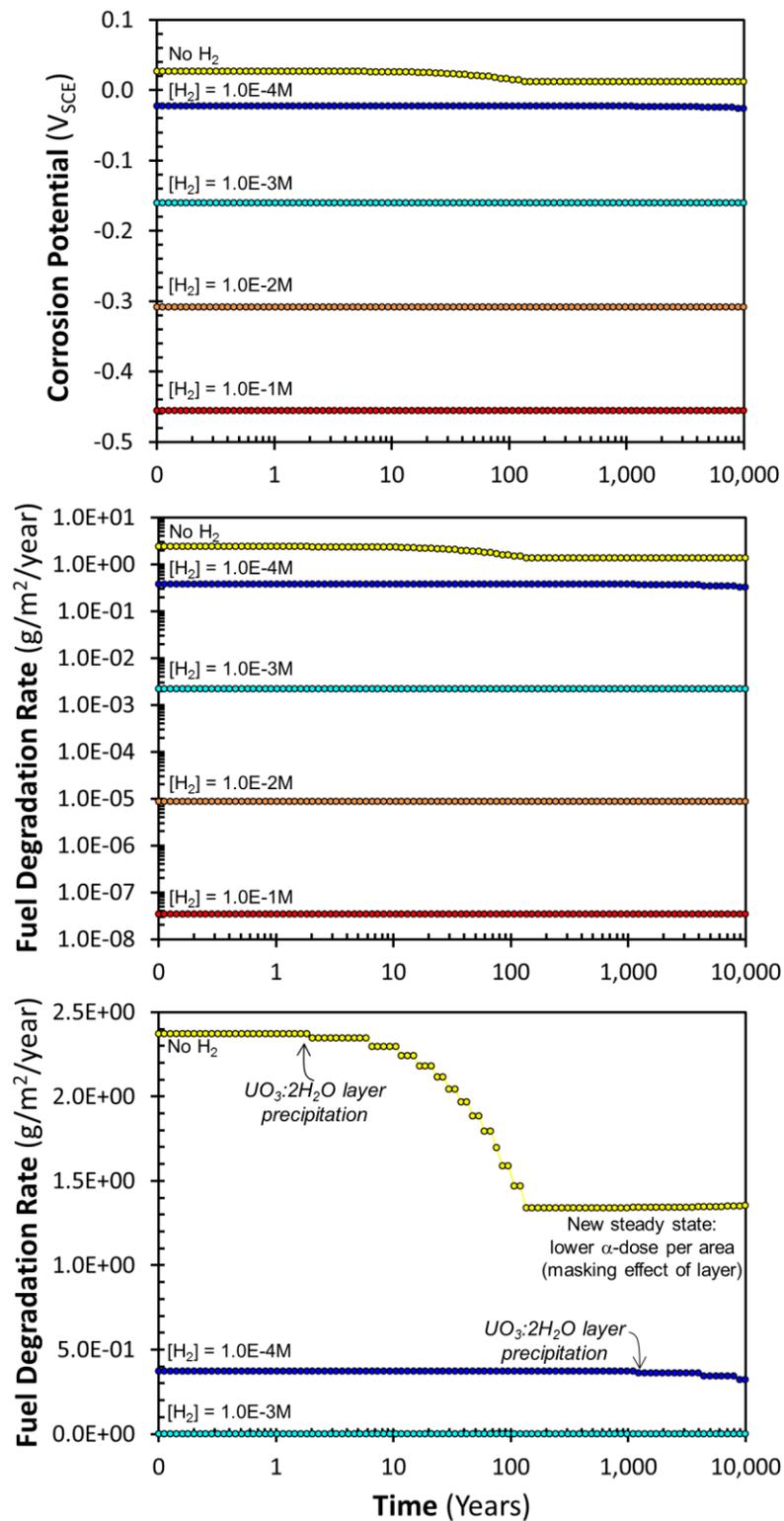
Figure 7.4. Examples of time-dependent fuel corrosion potentials and corresponding degradation rates calculated with the MPM for different dissolved hydrogen concentrations with 1% NMP at the fuel surface.
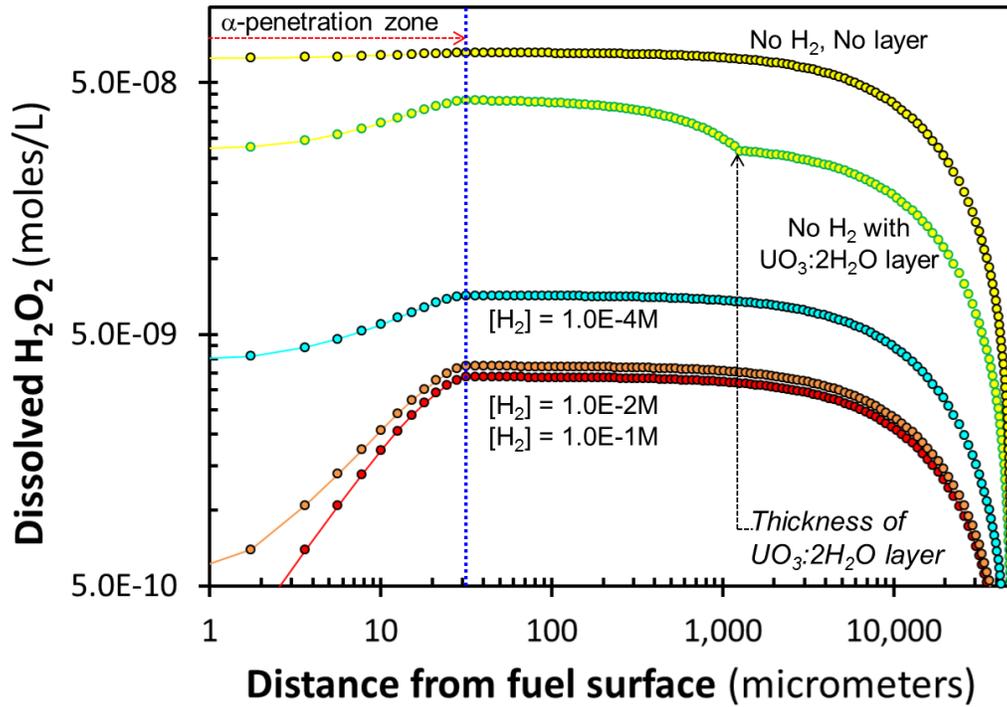
Figure 7.5. Concentration profiles of hydrogen peroxide produced by alpha radiolysis as a function of distance away from the fuel surface. Each point in the plot is an individual model realization in time and space.
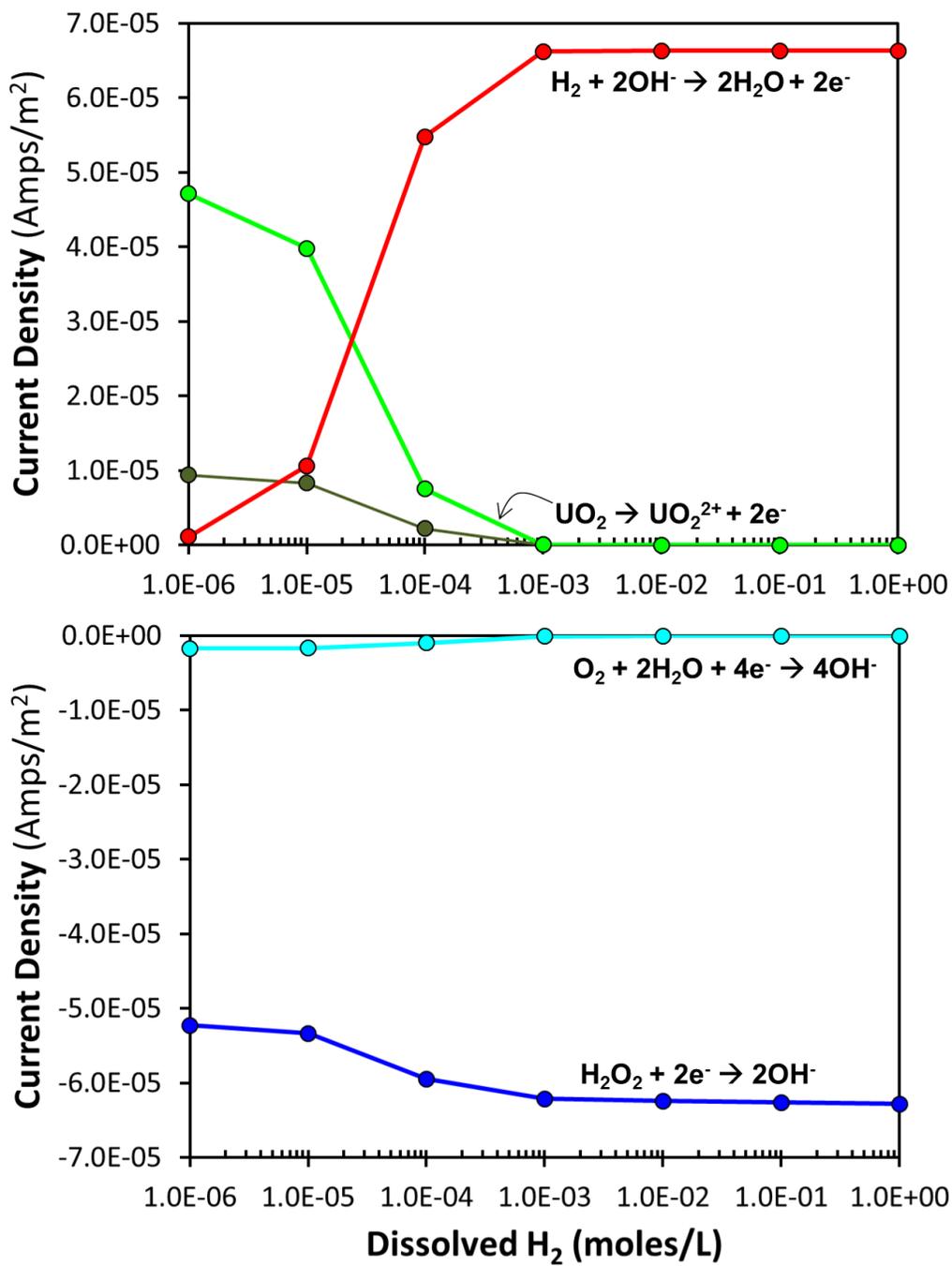
Figure 7.6. Current densities for the key reactions over a range of hydrogen concentrations. The anodic reactions are shown on the top plot, the cathodic reactions are shown on the bottom plot.
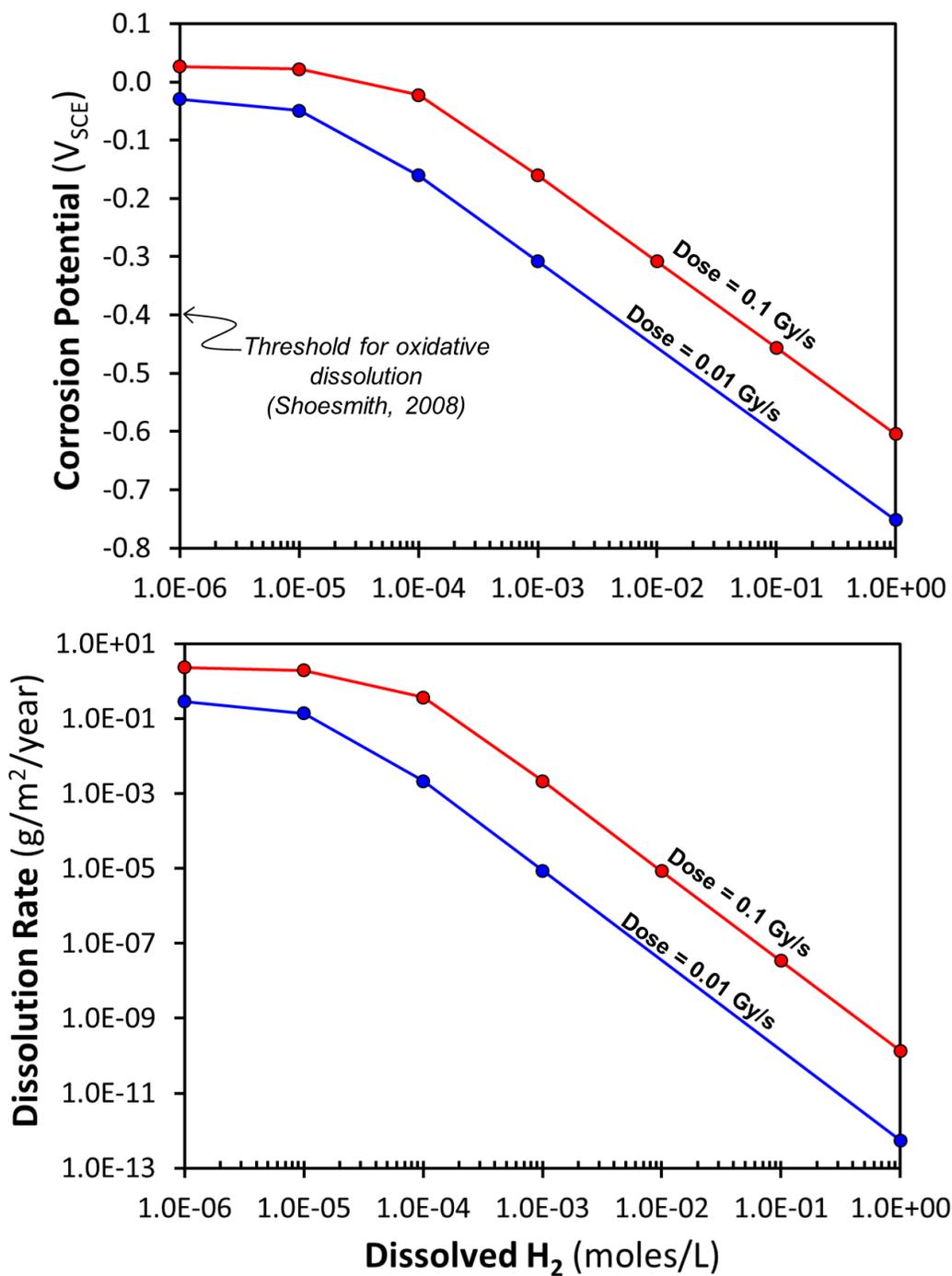
Figure 7.7. Fuel corrosion potential and dissolution rate as function of hydrogen concentration for two typical dose rates. Surface coverage of NMP is set at 1%, for other assumptions see Table 7.1 above.

8. SUMMARY OF ELECTROCHEMICAL EXPERIMENTS

Continuing the suite of tests discussed in Ebert et al., (2012), various electrochemical experiments were conducted to support the development and extension of the MPM. Experimental methods are being developed and optimized to:

- Verify the conceptual model for fuel matrix degradation that is being used.
- Identify important reactants in relevant environments.
- Quantify the effects of redox reactions on the corrosion potential at the fuel surface and the fuel matrix dissolution rate.
- Measure values for model parameters.
- Measure the effects of corrosion and poisoning on the catalytic efficiency of the NMP alloys.

An electrochemical system and testing methodology is being developed in which the dissolution of ceramic UO_2 materials representing used fuel are measured in controlled environments under floating or fixed potentials is measured directly (i.e., based on the dissolved U concentrations) and related to the measured electrochemical behavior and model parameter values used to calculate the U(IV) oxidation rate. The experimentally measured rate is based on direct measurements of the dissolved uranium concentrations and the modeled rate is a convolution of the rate of the electrochemical (charge-transfer) reaction oxidizing U(IV) to U(VI) and the dissolution rate of the U(VI)-bearing oxide that is formed.

Parallel experiments are being conducted to study the electrochemical behavior of alloys representing NMP particles under the same solution conditions that are used to characterize the UO_2 behavior. The experiments are conducted with separate electrodes fabricated from UO_2 and NMP alloy. Experiments are being conducted with the single electrodes to generate a data base with which the results of future experiments that will be conducted with electrically and chemically coupled electrodes to measure the dissolution behavior and kinetics of UO_2 in the presence of NMP alloys to quantify the catalytic efficiency of the NMP surfaces. The use of separate UO_2 and NMP electrodes provides flexibility to measure several effects likely to be important to the long-term corrosion behavior of used fuel: the effects of alloy corrosion and the presence of poisons on the catalytic efficiency of the NMP can be quantified and taken into account in the degradation model; the catalytic efficiencies of different NMP compositions (e.g., to represent different burn-ups) can be measured; and the corrosion behaviors of UO_2 doped with various lanthanides and actinides can be compared.

Experiments to-date were conducted to develop the methodology, characterize the electrochemical properties of the isolated UO_2 and NMP materials in H_2O_2-bearing solutions, and develop techniques for monitoring H_2O_2 and uranium concentrations during and after testing. A series of open circuit potential, potentiodynamic, Tafel, linear polarization, and electrochemical impedance spectroscopy measurements have been made using electrodes fabricated from pure UO_2 and NMP-W alloy materials in solutions with various amounts of H_2O_2 in air saturated 0.1 mM NaCl solutions and in the same solutions purged with argon or regeneration gas (regen), which is about 3% H_2 in Ar. These measurements provide baseline values for corrosion potentials and corrosion currents for a wide range of H_2O_2 concentrations to which the results of later tests with the combined UO_2 and various NMP alloys to quantify the catalytic effects.

The electrochemical experimental results have been compiled for use as a data base supporting the MPM as a collection of Microsoft EXCEL files. These have been entered into the document management system maintained for the DOE FCRD project at the Idaho National Laboratory under the same document number as this report. An index of the files as organized and the information contained is presented in Appendix 2. Analyses of several experiments remain in progress and will be reported in a later report.

9.   SUMMARY AND FUTURE WORK ON MPM

A process model for the surface catalysis of key redox reactions on noble metal bearing fission product alloy particles (NMP) was implemented within the Mixed Potential Module (MPM). The MPM is part of a larger integrated process level Fuel Degradation Model (FDM) which will provide information needed for radionuclide source term calculations used in the UFD generic repository performance assessment model.

The catalytic effects added to the MPM afford two important capabilities:

- Evaluation of the catalytic effects of the NMP on reactions affecting fuel matrix degradation.
- Evaluation of the long-term importance of H_2 oxidation in protecting used fuel from oxidative dissolution in disposal environments of interest.

The extension of the MPM to account for NMP catalysis successfully achieves one of the key goals for this project. However, large uncertainties remain and more experimental and modeling work is needed to fully quantify the fuel-protecting, hydrogen oxidation effect.

In support of model optimization and extension, electrochemical experiments were performed. Results from these tests are also presented in this report. The experimental work is focused on providing key model parameter values needed to improve predictive accuracy and capabilities of the MPM and thus the FDM.

The scope highlights for FY-2014 (focus of top three bullets) and out-years (all bullets):

- Implement integrated FDM consisting of the coupled MPM – Radiolysis Module (RM) and the Instant Release Fraction (IRF). This integrated model has been developed in concept (Figures 7.1 and 4.1 and Buck et al., 2013) but not yet implemented.
- Link FDM with UFD generic performance assessment models (Figures 7.1 and 4.1 above) to provide a scientific basis for radionuclide source terms.
- Tailor MPM – RM parameter database to account for solution chemistry specific to geologic repositories in argillite and crystalline rocks. This will involve extending the MPM to lower pH values and may involve adding speciation and redox reactions that account for components not currently included such as sulfate and dissolved silica.
- Develop a predictive understanding of the effects of corrosion and poisoning on the catalytic activity of the NMP. This work will emphasize the role of halides (F, Cl, Br, I), the effects of leaching Mo and Tc and the possible formation of Ru, Tc sulfides.
- Extend MPM to account for redox chemistry of key dose contributing radionuclides such as Tc, I, Np, and Pu at the fuel/solution interface.

- Extend MPM to account for effects of other alteration phases on used fuel degradation rate. This work will consider the incorporation of alpha emitters into alteration phases such as U(VI) silicates and U(VI) peroxides.

A crucial part of this work beyond FY-2014 is to continue the matrix of planned electrochemical and related experiments. Experimental results are needed to reduce uncertainties in the MPM – RM parameter database and to test model concepts. This work will improve the accuracy of source term calculations for future repository performance assessments.

10. REFERENCES (Sections 7 through 9)

Broczkowski, M. E., Noël, J. J., Shoesmith, D. W., (2005). *The inhibiting effects of hydrogen on the corrosion of uranium dioxide under nuclear waste disposal conditions*, Journal of Nuclear Materials 346, 16

Buck E., Jerden, J., Ebert, W., Wittman, R, (2013). *Coupling the Mixed Potential and Radiolysis Models for Used Fuel Degradation.* FCRD-UFD-2013-000290

Christensen, H., Sunder, S. (1996). An evaluation of water layer thickness effective in oxidation of UO$_2$ fuel due to radiolysis of water, *Journal of Nuclear Materials* 238: 70-77.

Ebert, W. L., Cruse, T. A., and Jerden J., (2012). *Electrochemical Experiments Supporting Oxide Fuel Corrosion Model*. FCRD-UFD-2012-000201

Jerden, J., Frey, K., Cruse, T., and Ebert, W. (2012). *Waste Form Degradation Model Status Report: Electrochemical Model for Used Fuel Matrix Degradation Rate*. FCRD-UFD-2012-000169.

Jerden, J., Frey, K., Cruse, T., and Ebert, W. (2013). *Waste Form Degradation Model Status Report: ANL Mixed Potential Model, Version 1. Archive*. FCRD-UFD-2013-000057.

King, F. and Kolar, M. (1999) "Mathematical Implementation of the Mixed-Potential Model of Fuel Dissolution Model Version MPM-V1.0", Ontario Hydro, Nuclear Waste Management Division Report No. 06819-REP-01200-10005 R00.

King, F. and Kolar, M. (2002) "Validation of the Mixed-Potential Model for Used Fuel Dissolution Against Experimental Data", Ontario Hydro, Nuclear Waste Management Division Report No. 06819-REP-01200-10077-R00.

King, F. and Kolar, M. (2003) "The Mixed-Potential Model for UO2 Dissolution MPM Versions V1.3 and V1.4", Ontario Hydro, Nuclear Waste Management Division Report No. 06819-REP-01200-10104 R00.

Shoesmith, D.W., M. Kolar, and F. King (2003). "A Mixed-Potential Model to Predict Fuel (Uranium Dioxide) Corrosion Within a Failed Nuclear Waste Container" *Corrosion, 59*, 802-816.

Shoesmith, D. W. (2008). *The Role of Dissolved Hydrogen on the Corrosion/Dissolution of Spent Nuclear Fuel*, NWMO TR-2008-19, November 2008 Nuclear Waste Management Organization, 22 St. Clair Avenue East, 6th Floor, Toronto, Ontario M4T 2S3, Canada

Trummer, M., Roth, O., and M. Jonsson, M., (2009), *H$_2$ Inhibition of Radiation Induced Dissolution of Spent Nuclear Fuel*, Journal of Nuclear Materials 383, 226-230

11. GENERATING STRUCTURAL AND THERMODYNAMIC DATA FOR GEOCHEMICAL AND USED FUEL DEGRADATION MODELS: A FIRST-PRINCIPLES APPROACH

11.1.1   Thermodynamic Properties of Uranyl Peroxide Hydrates Corrosion Phases on Spent Nuclear Fuel: Studtite and Metastudtite

11.1.1.1   Background

Thermodynamic parameters for corrosion phases, as well as engineered barrier systems materials and natural system minerals, are critical to assess their stability and behavior in geologic disposal environments for safety assessments. Metal-oxides constituting most of the spent nuclear fuel (SNF) are particularly prone to redox corrosion and dissolution, which is pervasive and of critical significance for environmental systems (Stumm, Sigg, and Sulzberger, 1992).

Oxidative dissolution of SNF leads to the formation of uranyl-based phases. The uranyl phases likely to form are primarily oxide hydrates, as well as a rich variety of other silicates, phosphates and carbonates, depending on the local natural system environment. Over fifty uranyl minerals/phases occur in nature and as corrosion products of SNF.

Among the corrosion phases that may form on SNF exposed to water, studtite and metastudtite, with formulas $(UO_2)O_2(H_2O)_4$ and $(UO_2)O_2(H_2O)_2$, respectively, are considered to be of particular importance (McNamara, Buck, and Hanson, 2003; Hanson, et al.,2005; McNamara, Hanson, Buck, & Soderquist, 2005). These hydrates of uranyl peroxide, which incorporate $(O_2)^{2-}$ generated by α-radiolysis of water (Draganic and Draganic, 1971; Sattonnay, et al., 2001; Amme, 2002), may play a crucial role in the degradation of nuclear fuel in the context of geological repositories – or nuclear reactor accidents (Hughes-Kubatko, Helean, Navrotsky, and Burns, 2003; Armstrong, Nyman, Shvareva, Sigmon, Burns, and Navrotsky, 2012; Burns, Ewing, and Navrotsky, 2012). Studtite and metastudtite are also the only two known minerals containing peroxide. In addition to playing a role for corrosion of SNF, studtite may retain released radionuclides through incorporation into its structure (Buck, Hanson, Friese, Douglas, and McNamara, 2004; Shuller, Ewing, and Becker, 2010).

Due in part to the unique nature of these compounds, the characterization of studtite and metastudtite evolved rather slowly. The structures of studtite and metastudtite were fully elucidated only recently (Burns and Hugues, 2003; Ostanin and Zeller, 2007; Weck, Kim, Jové-Colón, and Sassani, 2012). However, very limited information on the stability and thermodynamic properties of these compounds is currently available, due to the difficulty of the calorimetric experiments involving uranyl minerals and compounds (Shvareva, Fein, and Navrotsky, 2012).

The main objectives of this study, using first-principles methods (without the need for any experimental input), are to:

- Calculate missing thermodynamic data needed for SNF degradation models, as a fast, systematic, and early way to avoid using expensive and time-consuming real materials and to complement experiments.
- Provide an independent assessment of existing experimental thermodynamic data and resolve contradictions in existing calorimetric data.

- Validate our computational approach using high-quality calorimetric data.

Details of our computational approach are given in the next section, followed by a complete analysis and discussion of our results.

11.1.1.2   *Computational Methods*

A schematic representation of the three-step computational approach used in this report is displayed in Figure 11.1. The first step consists of a crystal structure optimization using density functional theory (DFT), followed by a calculation of phonon frequencies using density functional perturbation theory (DFPT), and, finally, a phonon analysis is carried out to derive the thermodynamics properties of the crystalline system investigated.
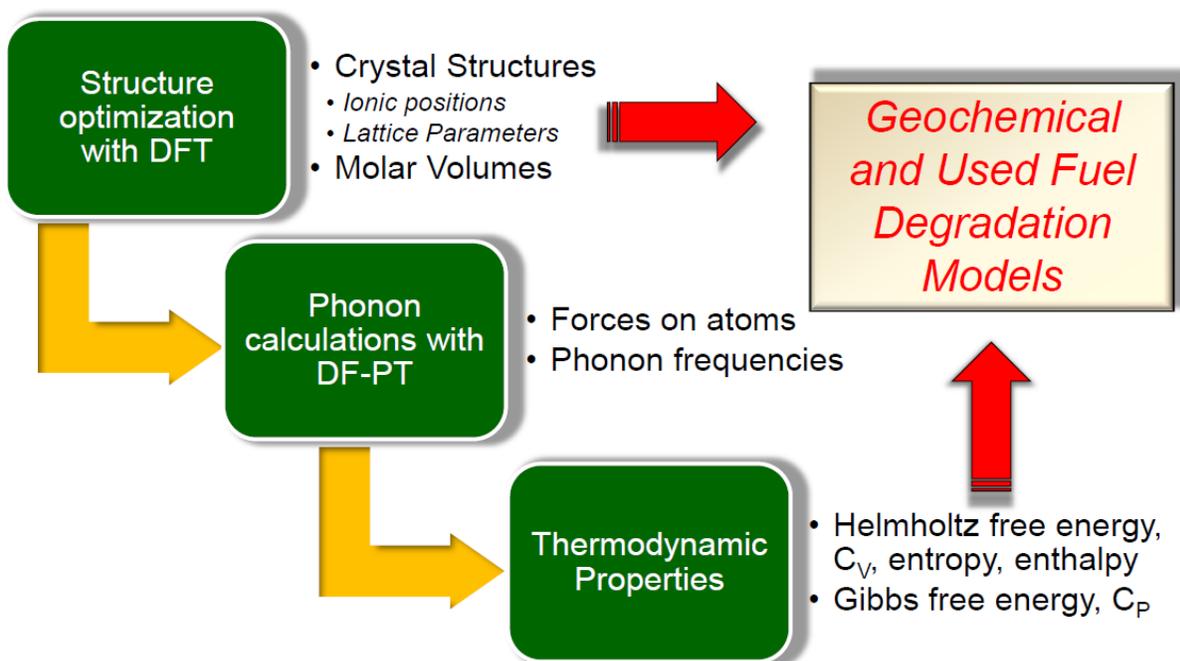
Figure 11.1. Schematic representation of the three-step computational approach used to calculate the thermal properties of crystalline systems using first-principles methods.

The equilibrium structures of studtite and metastudtite, previously optimized (cf. Figure 11.2) using the standard density functional theory (DFT) implemented in the Vienna Ab initio Simulation Package (VASP) (Kresse & Furthmüller, 1996), were used to build a set of supercells; details of the geometry optimization calculations are given in Weck, Kim, Jové-Colón, and Sassani, 2012. The forces exerted on atoms of the set of supercells were calculated using density functional perturbation theory (DFPT) with VASP at the GGA/PW91 level of theory (Perdew & Wang, 1992) and phonon frequencies were computed. Phonon analysis was performed at constant equilibrium volume in order to derive isochoric thermal properties (e.g., the phonon (Helmholtz) free energy, the entropy and the isochoric heat capacity).
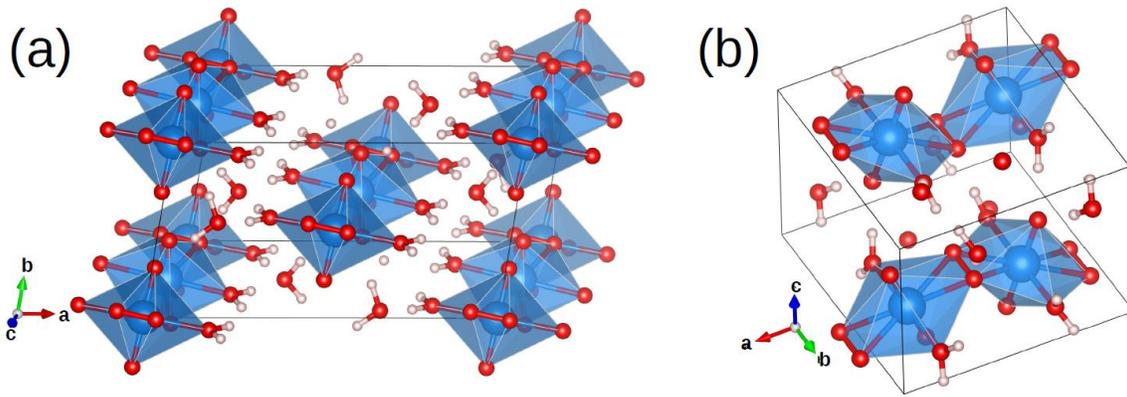
Figure 11.2. Crystal unit cells of (a) studtite, $(UO_2)O_2(H_2O)_4$ (space group $C2/c$, $Z = 4$), and (b) metastudtite, $(UO_2)O_2(H_2O)_2$ (space group $Pnma$, $Z = 4$), relaxed with DFT at the GGA/PW91 level of theory. Color legend: U, blue; O, red; H, white.

The Helmholtz free energy was calculated using the following formula:

$$F = \frac{1}{2} \sum \hbar\omega + k_B T \sum \ln\left[1 - e^{-\hbar\omega/k_B T}\right].$$

The entropy was computed using the expression:

$$S = -k_B \sum \ln\left[1 - e^{-\hbar\omega/k_B T}\right] - \frac{1}{T} \sum \frac{\hbar\omega}{e^{\hbar\omega/k_B T} - 1}.$$

The heat capacity at constant volume was calculated using the formula:

$$C_V = \sum k_B \left[\frac{\hbar\omega}{k_B T}\right]^2 \frac{e^{\hbar\omega/k_B T}}{\left[e^{\hbar\omega/k_B T} - 1\right]^2}.$$

Further analysis from a set of phonon calculations in the vicinity of each computed equilibrium crystal structure was carried out to obtain thermal properties at constant pressure (e.g., the Gibbs free energy and the isobaric heat capacity) within a quasi-harmonic approximation (QHA). The QHA mentioned here introduces volume dependence of phonon frequencies as a part of anharmonic effect. A part of temperature effect can be included into the total energy of electronic structure through the phonon (Helmholtz) free energy at constant volume, but thermal properties at constant pressure are what we want to know. Therefore, some transformation from a function of volume V to a function of pressure p is needed. The Gibbs free energy is defined at a constant pressure by the transformation:

$$G(T,p) = \min_V \left[U(V) + F_{phonon}(T;V) + pV\right],$$

where $\min_V[$ function of $V]$ means to find unique minimum value in the brackets by changing volume. Since volume dependencies of energies in electronic and phonon structures are different, volume giving the minimum value of the energy function in the square brackets shifts from the value calculated only from electronic structure even at $T = 0$ K. By increasing temperature, the volume dependence of phonon free energy changes, then the equilibrium volume at temperatures changes.

The heat capacity at constant pressure versus temperature was also derived as the second derivative of the Gibbs free energy with respect to T, i.e.:

$$C_P = -T\frac{\partial^2 G}{\partial T^2}.$$

In order to derive the enthalpy function, $(H_T - H_{298.15}).T^{-1}$, and the Gibbs energy function, $(G_T - H_{298.15}).T^{-1}$, the thermal evolutions of the isobaric heat capacity calculated from first-principles were first fitted using a nonlinear least-squares regression to a Haas-Fisher-type polynomial, i.e,

$$C_P(T) = a + bT + cT^{-2} + dT^{-0.5} + eT^2.$$

The enthalpy function was then computed by analytical integration of the fit to the isobaric heat capacity using the formula:

$$(H_T - H_{298.15}).T^{-1} = \int_{298.15}^{T} (a + bT + cT^{-2} + dT^{-0.5} + eT^2)dT.$$

The Gibbs energy function was then computed using the following expression:

$$(G_T - H_{298.15}).T^{-1} = (H_T - H_{298.15}).T^{-1} - S_T,$$

where S_T is the entropy calculated from first-principles.

11.1.1.3   Results and Discussion

The thermal properties (Helmoltz free energy, entropy, isochoric molar heat capacity and total internal energy) of bulk studtite and metastudtite calculated from phonon frequencies at constant equilibrium volume at the DFT/DFPT/PW91 level of theory are shown in Figures 11.3 and 11.4, respectively. To the best of our knowledge, no experimental data are available for the sake of comparison. The results for the thermal properties of studtite and metastudtite at standard pressure (1 bar) calculated within the quasi-harmonic approximation, i.e. the Gibbs free energy and isobaric heat capacity, are displayed in Figures 11.5 to 11.8.

As shown in Figures 11.3 and 11.4, the entropy increases steadily with temperature and with the unit-cell volume expansion occurring for studtite and metastudtite. This is consistent with the fact that a temperature or unit-cell volume increase results in a larger number of microstates in the system, W, which in turn increases logarithmically the entropy according to Boltzmann's entropy formula, $S = k_B .\log W$, where k_B is the Boltzmann constant.

The monotonically decreasing Gibbs free energy curves and their derived isobaric heat capacities C_p as a function of the temperature are show in Figures 11.5 to 11.8. The predicted Dulong-Petit asymptotic values of studtite and metastudtite, i.e. $C_p = n3R$, where n is the number of atoms per f.u. and R is the universal gas constant, are 424.0 J.K^{-1}.mol^{-1} and 274.3 J.K^{-1}.mol^{-1}, respectively. At $T = 800$ K, the highest boundary of the thermal range investigated here, the computed C_p values for studtite and metastudtite are still well below their Dulong-Petit asymptotes, i.e. by ca. 25% and 21%, respectively. As expected, $C_p[(UO_2)O_2(H_2O)_4] > C_p[(UO_2)O_2(H_2O)_2]$ over the complete temperature range investigated, which is in line with the calculated entropy for both compounds, since the variation of entropy with T corresponds to the integral of (C_p/T) over a given temperature range. This stems from the loss of H_2O molecules from studite to metastudtite.
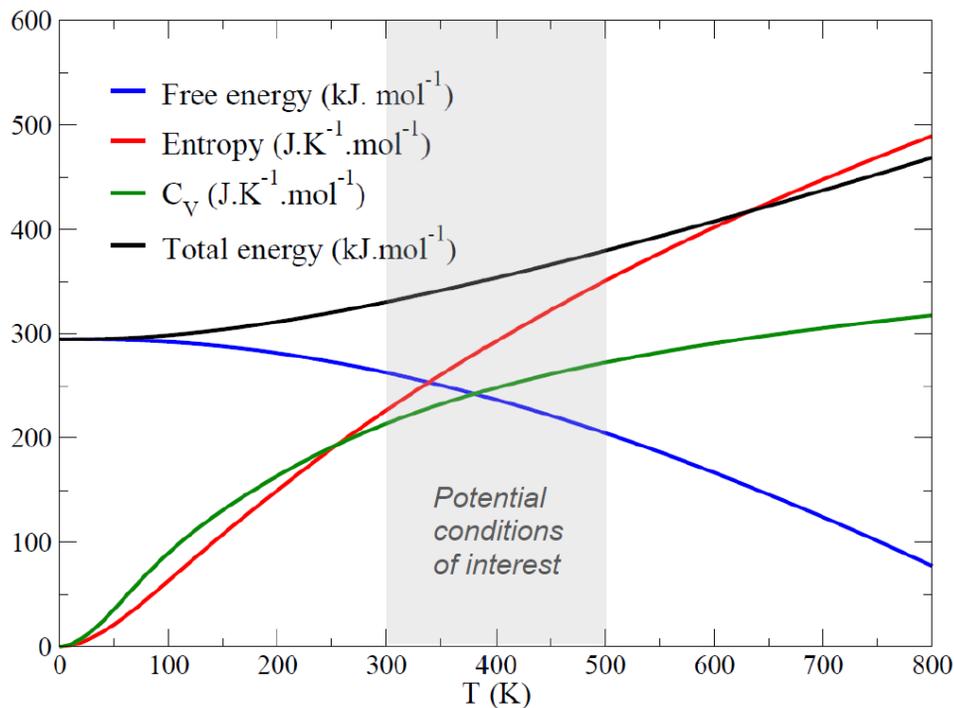
Figure 11.3. Thermal properties of studtite, $(UO_2)O_2(H_2O)_4$, calculated at constant equilibrium volume at the DFT/PW91 level of theory. Potential thermal conditions of interest for nuclear waste disposal in geological repositories are indicated as a shaded area.
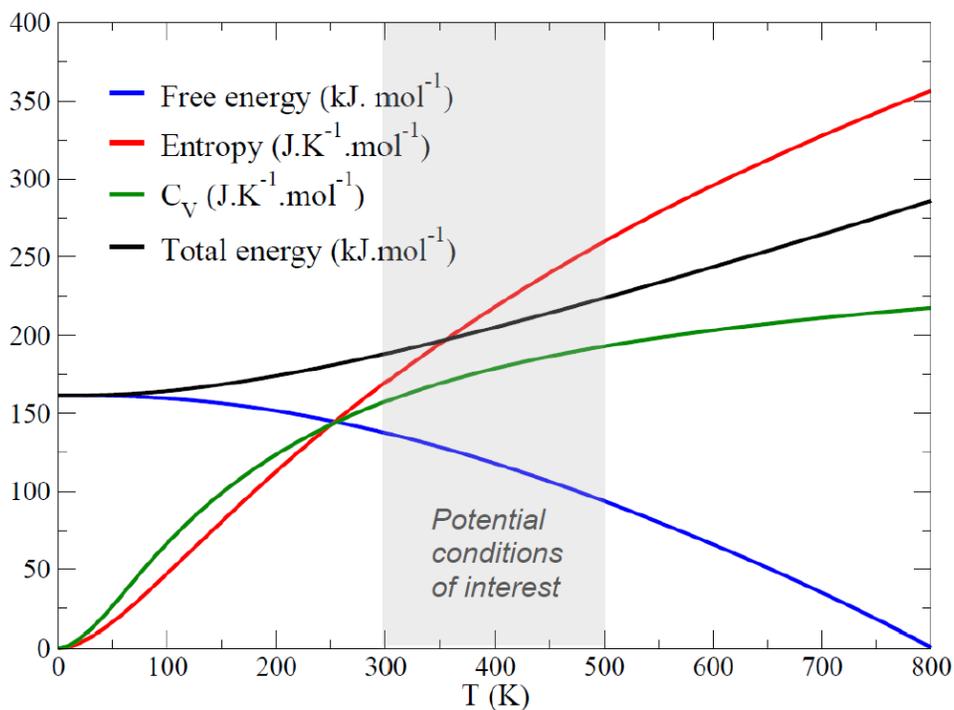
Figure 11.4. Thermal properties of metastudtite, $(UO_2)O_2(H_2O)_2$, calculated at constant equilibrium volume at the DFT/PW91 level of theory. Potential thermal conditions of interest for nuclear waste disposal in geological repositories are indicated as a shaded area.
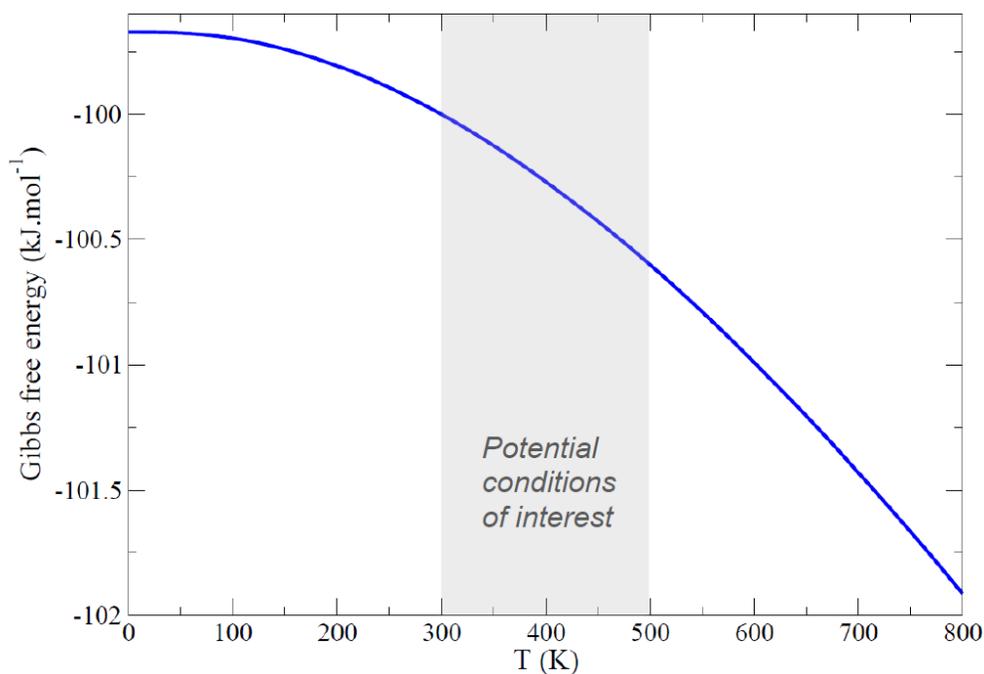
Figure 11.5. Gibbs free energy of studtite calculated at constant atmospheric pressure at the DFT/PW91 level of theory. Potential thermal conditions of interest for nuclear waste disposal in geological repositories are indicated as a shaded area.
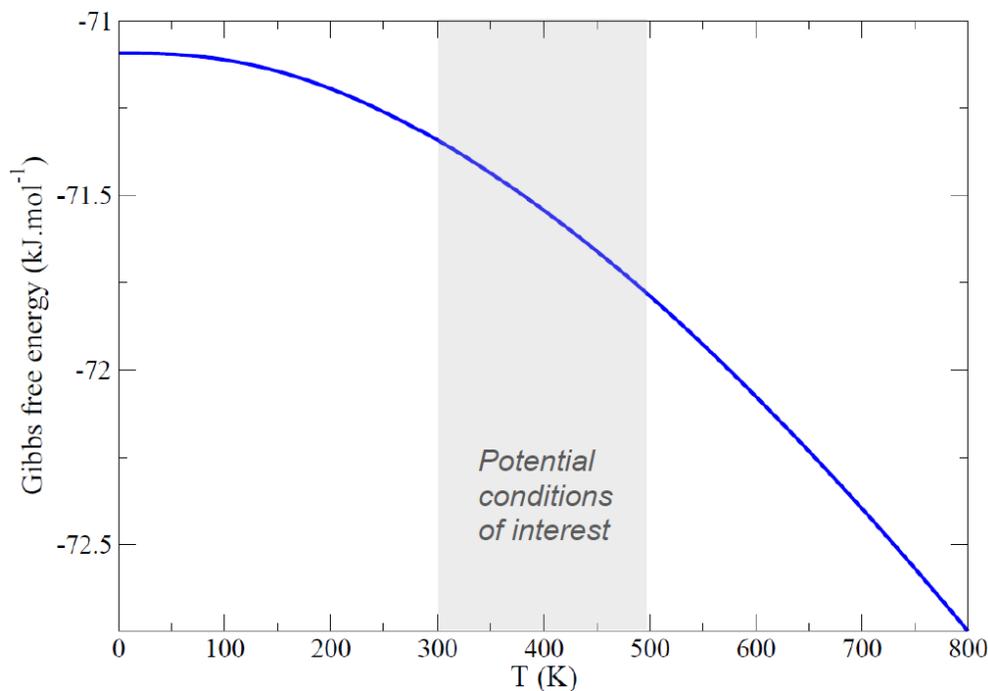
Figure 11.6. Gibbs free energy of metastudtite calculated at constant atmospheric pressure at the DFT/PW91 level of theory. Potential thermal conditions of interest for nuclear waste disposal in geological repositories are indicated as a shaded area.
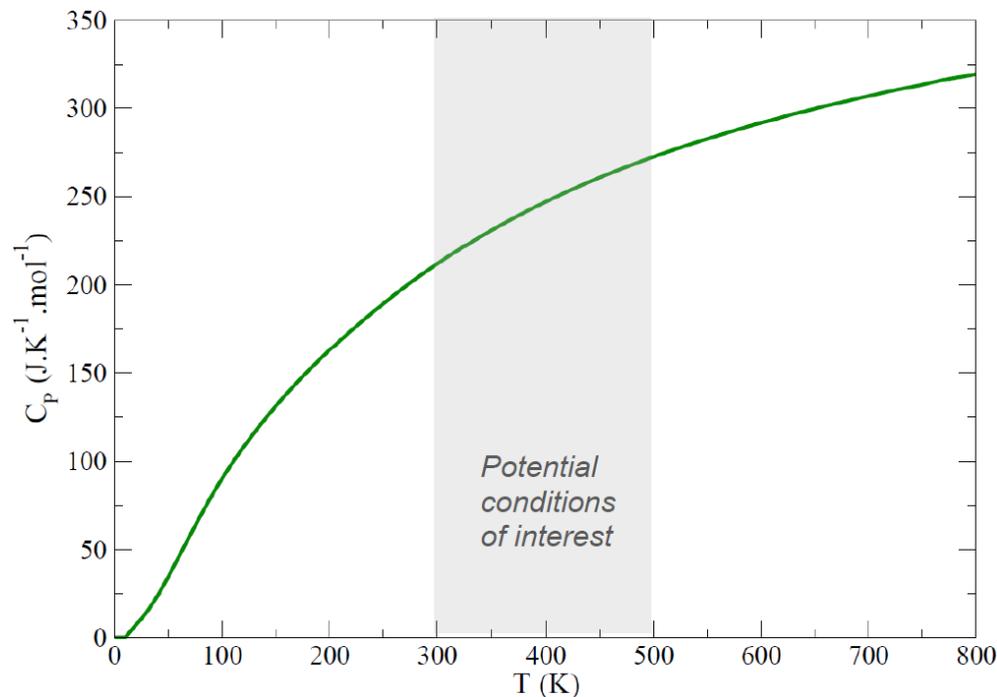
Figure 11.7. Heat capacity of studtite calculated at constant atmospheric pressure at the DFT/PW91 level of theory. Potential thermal conditions of interest for nuclear waste disposal in geological repositories are indicated as a shaded area.
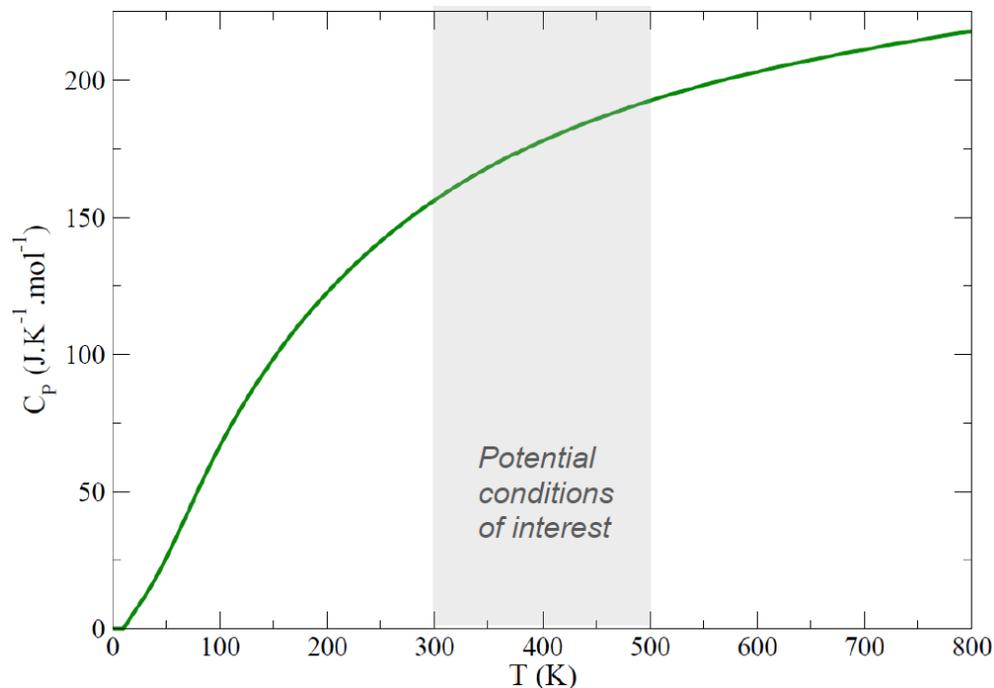
Figure 11.8. Heat capacity of metastudtite calculated at constant atmospheric pressure at the DFT/PW91 level of theory. Potential thermal conditions of interest for nuclear waste disposal in geological repositories are indicated as a shaded area.

The thermal evolutions of the isobaric heat capacity (P = 1 bar) calculated from first-principles for studtite and metastudtite (see Figures 11.7 and 11.8) were fitted over the temperature range 290–800 K using a nonlinear least-squares regression to a Haas-Fisher-type polynomial, i.e,

$$C_P(T) = a + bT + cT^{-2} + dT^{-0.5} + eT^2,$$

with the resulting optimized coefficients given in Table 11.1. The sums of the squared differences are small, 0.21 for studtite and 0.16 for metastudtite, suggesting a good correlation between the predicted data and the resulting fits.

Table 11.1. Coefficients of the Haas-Fisher heat capacity polynomial $C_p(T)$ for the studtite and metastudite compounds. The range of validity of the fit is 290–800 K.

Compound	$a \times 10^2$ (T^0)	$b \times 10^{-2}$ (T)	$c \times 10^6$ (T^{-2})	$d \times 10^3$ ($T^{-0.5}$)	$e \times 10^{-5}$ (T^2)	SSD[a]
Studtite	5.7999	-6.498	2.2373512	-6.51293	2.892	0.21
Metastudtite	3.1599	-0.405	-0.2250414	-2.70420	0.187	0.16

[a] Sum of squared differences (SSD) between calculated and fitted data.
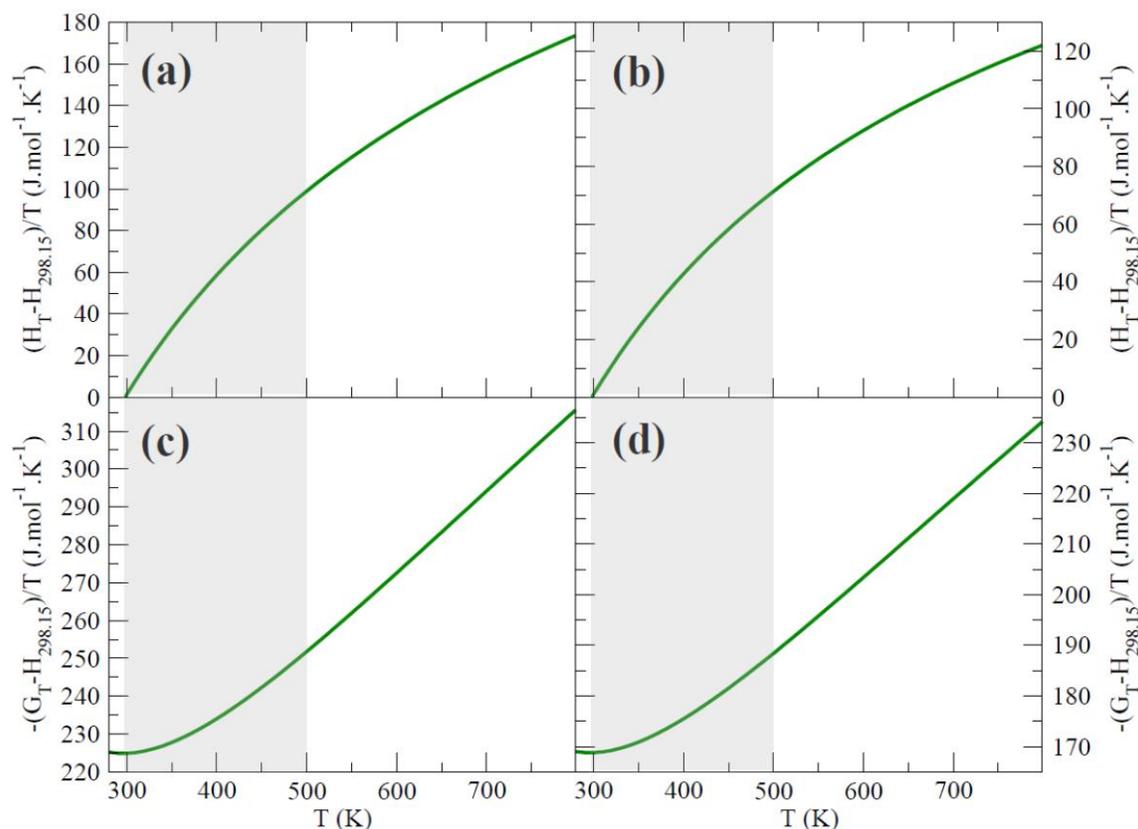
Figure 11.9. Enthalpy functions and Gibbs energy functions of studtite [(a) and (c)] and metastudtite [(b) and (d)] calculated at the DFT/PW91 level of theory. Potential thermal conditions of interest for nuclear waste disposal in geological repositories are indicated as a shaded area.

The enthalpy functions and Gibbs energy functions of studtite and metastudtite were also calculated by analytical integration of the fit to the isobaric heat capacity and using the entropy calculated from first-principles as described above; results are displayed in Figure 11.9. However, to the best of our knowledge, no experimental data are available for the sake of comparison, and these results are the first theoretical predictions of the thermal properties for these compounds using a rigorous first-principles methodology.

11.1.2   Structures and Properties of Layered Uranium(VI) Oxide Hydrates: Study of Polymorphism in Dehydrated Schoepite

11.1.2.1   *Background*

Deciphering the complex interplay between the crystal structures and properties of inorganic uranyl compounds and uranyl minerals is crucial to gain understanding of the transport and fixation of uranium in the environment, the paragenesis of uranyl minerals, and the performance of geological repositories for used nuclear fuel.

Among the known minerals containing hexavalent uranium, the uranyl oxide hydrates, represent an important subgroup. The crystal structures of most uranyl oxide hydrates are based on sheets of polyhedra of the form $[(UO_2)_x O_y(OH)_z]^{(2x-2y-z)}$. This includes four closely related uranyl oxide hydrates/hydroxides without interlayer cations that form the schoepite subgroup and the fourmarierite group: schoepite, metaschoeptite, "paraschoepite" and dehydrated schoepite.

Among these uranyl oxide hydrates/hydroxides without interlayer cations, dehydrated schoepite was found to have a composition ranging from $UO_3(H_2O)_{0.75}$ to $UO_3(H_2O)$ (Finch, Hawthrone, and Ewing, 1998) and lead to the formation of studtite in the presence of moisture and hydrogen peroxide. Assuming an ideal stoichiometry of $UO_2(OH)_2$ (or $UO_3(H_2O)$) for simplicity, the experiments conducted so far have shown that dehydrated schoepite is rapidly converted to studtite upon contact with hydrogen peroxide and moisture according to the reaction:

$$UO_2(OH)_2 + H_2O_2 + 2 H_2O \rightarrow [(UO_2)(O_2)(H_2O)_2](H_2O)_2.$$
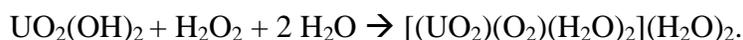
Recent experiments have shown that at low concentration of H_2O_2 (i.e. 0.001 M), a few percents of the crystalline higher hydrate metaschoepite, $UO_3(H_2O)_2$, also formed, while higher concentrations of H_2O_2 in the range 0.01–0.05 M resulted in a mixture of dehydrated schoepite and studtite or even complete conversion to studtite for concentrations in excess of 0.1 M H_2O_2 (Forbes, Horan, Devine, McInnis, and Burns, 2011). Details of such interconversions between dehydrated schoepite, metaschoepite, and schoepite have been discussed elsewhere (Finch, Hawthrone, and Ewing, 1998).

Dehydrated schoepite exists in three crystal forms, α, β and γ, which can be prepared hydrothermally from UO_3 and H_2O (Dawson, Wait, Alcock, and Chilton, 1956). Using first-principles methods, polymorphism is investigated in this layered uranium(VI) oxide hydrate. In particular, computational approaches going beyond the standard DFT framework are utilized here and include corrections for possible strong on-site Coulomb repulsion between uranium 5f electrons or for van der Waals dispersion interactions. Details of our computational approach are provided in the next section, followed by a discussion of our results and conclusions.

11.1.2.2   *Computational Methods*

First-principles total energy calculations were performed using spin-polarized density functional theory, as implemented in the Vienna Ab initio Simulation Package (VASP) (Kresse and

Furthmüller, 1996). The exchange-correlation energy was calculated within the generalized gradient approximation (GGA+U) (Perdew, et al., 1992), with the parameterization of Perdew, Burke, and Ernzerhof (PBE) (Perdew, Burke, and Ernzerhof, 1996), corrected with an effective Hubbard parameter to account for the strong on-site Coloumb repulsion between localized uranium 5f electrons. Standard functionals such as the PBE or PW91 functionals were found in previous studies to correctly describe the geometric parameters and properties of various uranium oxides and uranium containing structures observed experimentally (Weck, Kim, Balakrishnan, Poineau, Yeamans, and Czerwinski, 2007; Weck, Kim, Masci, Thuery, and Czerwinski, 2010; Weck, Gong, Kim, Thuery, and Czerwinski, 2011; Thompson and Wolverton, 2011; Weck, Kim, Jové-Colón, and Sassani, 2012).

The rotationally-invariant formalism developed by Dudarev and co-workers (Dudarev, Botton, Savrasov, Humphreys, & Sutton, 1998) was used, which consists in adding a penalty functional to the standard GGA total-energy functional, E_{GGA}, that forces the on-site occupancy matrix in the direction of idempotency, i.e.

$$E_{\text{GGA}+U} = E_{\text{GGA}} + \frac{(\bar{U}-\bar{J})}{2}\sum_\sigma [\text{Tr}(\rho^\sigma) - \text{Tr}(\rho^\sigma \rho^\sigma)],$$

where $\bar{U}$ and $\bar{J}$ are the spherically-averaged matrix elements of the screened electron-electron Coloumb and exchange interactions, respectively, and ρ^σ is the density matrix of 5f electrons with a given projection of spin σ. In Dudarev's approach only $U_{\text{eff}} = \bar{U} - \bar{J}$ is meaningfull. Therefore, only $\bar{U}$ was allowed to vary in the calculations.

The interaction between valence electrons and ionic cores was described by the projector augmented wave (PAW) method (Blöchl, 1994; Kresse and Joubert, 1999). The U($6s$,$6p$,$6d$,$5f$,$7s$) and O($2s$,$2p$) electrons were treated explicitly as valence electrons in the Kohn-Sham (KS) equations and the remaining core electrons together with the nuclei were represented by PAW pseudopotentials. The KS equation was solved using the blocked Davidson (Davidson, 1983) iterative matrix diagonalization scheme. The plane-wave cutoff energy for the electronic wavefunctions was set to 500 eV, ensuring the total energy of the system to be converged to within 1 meV/atom.

Since the structure of dehydrated schoepite consists of stacked $UO_2(OH)_2$ layers linked by O–H···O(uranyl) hydrogen bonds, it can be inferred that van der Waals dispersion interactions may play a role in the possible structures and properties of the various polymorphs of this compound. However, popular density functionals are unable to describe correctly van der Waals interactions resulting from dynamical correlations between fluctuating charge distributions. A pragmatic method to work around this problem has been given by density functional theory corrected for dispersion (DFT-D) (Wu, Vargas, Nayak, Lotrich and Scoles, 2001), which consists in adding a semi-empirical dispersion potential to the conventional Kohn-Sham GGA total-energy functional, E_{GGA} , i.e.,

$$E_{\text{GGA}-\text{DFT}-\text{D}} = E_{\text{GGA}} + E_{\text{disp}}.$$

In the DFT-D2 method of Grimme (Grimme, 2006) utilized in this study, the van der Waals interactions are described via a simple pair-wise force field, which is optimized for DFT functionals. The dispersion energy for periodic systems is defined as:

$$E_{\text{disp}} = -\frac{s_6}{2} \sum_{i=1}^{N} \sum_{j=1}^{N} \sum_{L}' \frac{C_6^{ij}}{|\vec{r}^{i,0} - \vec{r}^{j,L}|^6} f\left(|\vec{r}^{i,0} - \vec{r}^{j,L}|\right),$$

where the summation are over all atoms N and all translations of the unit cell $L = (l_1, l_2, l_3)$, with the prime sign indicating that cell $i \neq j$ for $L = 0$, s_6 is a global scaling factor, C_6^{ij} is the dispersion coefficient for the atom pair ij, $\vec{r}^{j,L}$ is a position vector of atom j after performing L translations of the unit cell along lattice vectors. In practice, terms corresponding to interactions over distances longer than a certain suitably chosen cutoff radius contribute only negligibly to the dispersion energy and can be ignored. The term $f(r^{i,j})$ is a damping function:

$$f(r^{i,j}) = \frac{1}{1+e^{-d(r^{i,j}/R_0^{ij}-1)}},$$

whose role is to scale the force field such as to minimize contributions from interactions within typical bonding distances. Combination rules for dispersion coefficients C_6^{ij} and van der Waals radii R_0^{ij} are:

$$C_6^{ij} = \sqrt{C_6^i C_6^j},$$

and

$$R_0^{ij} = R_0^i + R_0^j.$$

The global scaling parameter s_6 has been optimized for several different DFT functionals and corresponds to a value of $s_6 = 0.75$ for the PBE functional used in this study. The parameters used in the empirical force-field of Grimme (Grimme, 2006) are $R_0 = 1.001$ Å and $C_6 = 0.14$ Jnm^6.mol^{-1} for hydrogen and $R_0 = 1.342$ Å and $C_6 = 0.70$ Jnm^6.mol^{-1} for oxygen.

In this work, both the GGA+U and GGA-DFT-D methods are also used concurrently, therefore, the resulting total-energy functional can be expressed as:

$$E_{\text{GGA}+U-DFT-D} = E_{\text{GGA}} + \frac{(\bar{U}-\bar{J})}{2}\sum_\sigma[\text{Tr}(\rho^\sigma) - \text{Tr}(\rho^\sigma\rho^\sigma)] + E_{\text{disp}},$$

where all the notations used keep the same meaning as defined previously.

All structures were optimized with periodic boundary conditions applied. Ionic relaxation was carried out using the quasi-Newton method and the Hellmann-Feynman forces acting on atoms were calculated with a convergence tolerance set to 0.01 eV/Å. Structural optimizations and properties calculations were carried out using the Monkhorst-Pack special k-point scheme (Monkhorst & Pack, 1976) with 5×3×5, 5×5×3 and 5×5×5 meshes for integrations in the Brillouin zone (BZ) of the bulk α–, β–, and γ–UO$_2$(OH)$_2$ phases, respectively. The tetrahedron method with Blöchl corrections (Blöchl, Jepsen, and Andersen, 1994) was used for BZ integrations. Periodic unit cells containing 28 atoms (Z = 4) for the α and β phases and 14 atoms (Z = 2) for the γ phase were used in the calculations. Ionic and cell relaxations of the experimental bulk structures (Bannister and Taylor, 1970; Taylor and Hurst, 1971; Taylor, Kelly and Downer, 1972; Siegel, Hoekstra, and Gebert, 1972) were performed simultaneously, without symmetry constraints.

11.1.2.3 *Results and Discussion*

The crystal parameters for UO$_2$(OH)$_2$ were determined originally from XRD by Taylor and co-workers (Bannister and Taylor, 1970; Taylor and Hurst, 1971; Taylor, 1971; Taylor, Kelly and Downer, 1972) and others (Roof, Cromer and Larson, 1964; Siegel, Hoekstra, and Gebert, 1972).

For α-UO$_2$(OH)$_2$: a = 4.2455(6), b = 10.3183(16), c = 6.8648(10) Å, $\alpha = \beta = \gamma$ =90°, V = 300.7(l) Å^3, Z = 4, and space group *Cmca* (IT No. 64) or *C2cb* (IT No. 41); for β-UO$_2$(OH)$_2$: a = 5.6438(l), b = 6.2867(l), c = 9.9372(2) Å, $\alpha = \beta = \gamma$ =90°, V = 352.58(2) Å^3, Z = 4, and space group *Pbca* (IT No. 61); for γ-UO$_2$(OH)$_2$: a = 5.560(3), b = 5.522(3), c = 6.416(3) Å, $\alpha = \gamma$ =90°, β=112.71(9)°, V = 181.71 Å^3, Z = 2, and space group *P2$_1$/c* (IT No. 14).

In the α phase, the UO$_2$(OH)$_2$ layers are linked by O-H$\cdots$O (uranyl) hydrogen bonds and the uranium coordination number is eight, with a puckered hexagonal arrangement (Taylor, 1971). In the β phase, the uranium centers possess a coordination of six in with octahedral arrangement and the the stacked UO$_2$(OH)$_2$ layers are also linked by O-H$\cdots$O (uranyl) hydrogen bonds (Bannister and Taylor, 1970). The location of hydrogen atoms in the α and β phases were confirmed by the neutron powder diffraction studies of Taylor and Hurst (Taylor and Hurst, 1971). In the γ phase, the configuration about uranium atoms is a distorted octahedron with variable U-O distances and the overall structure show strong similarity to β-UO$_2$(OH)$_2$.
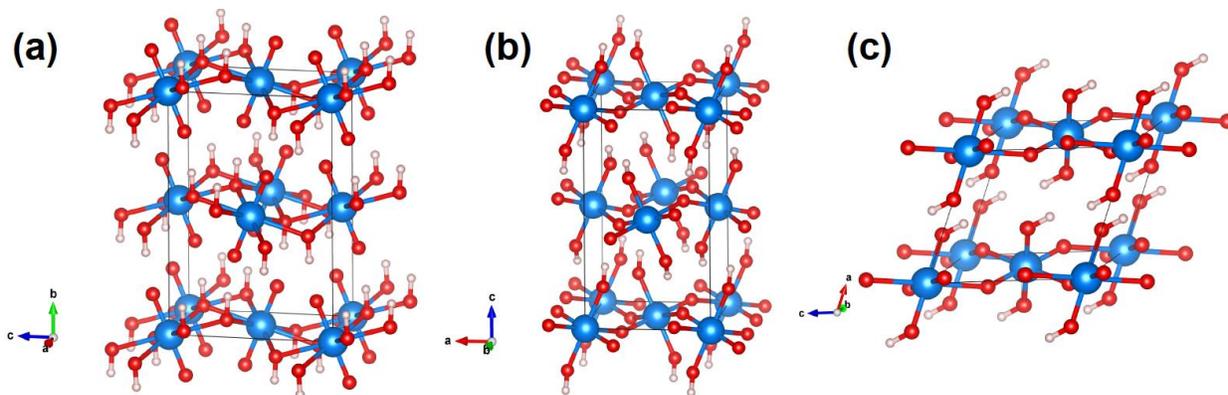
Figure 11.10. Crystal unit cells of the (a) alpha-, (b) beta- and (c) gamma phases of dehydrated schoepite, UO$_2$(OH)$_2$, relaxed with DFT at the GGA/PBE level of theory. Color legend: U, blue; O, red; H, white.

Crystal unit cells of the α, β, and γ phases of dehydrated schoepite relaxed with DFT at the GGA/PBE level of theory are depicted in Figure 11.10. The optimized structures are in overall good agreement with the three structures characterized experimentally. Using standard DFT, the following lattice parameters were obtained: 1) α-UO$_2$(OH)$_2$: a = 4.233, b = 10.344, c = 6.970 Å, $\alpha = \beta = \gamma$ =90°, V = 305.2 Å^3; 2) β-UO$_2$(OH)$_2$: a = 5.848, b = 6.204, c = 9.867 Å, $\alpha = \beta = \gamma$ =90°, V = 358.0 Å^3; 3) γ-UO$_2$(OH)$_2$: a = 5.891, b = 5.322, c = 6.369 Å, $\alpha = \gamma$ =90°, β=113.8°, V = 182.73 Å^3. Since some small discrepancies subsist between parameters computed with standard DFT and values determined with XRD the influence of possible van der Waals interactions and strong electron correlation was investigated for α-UO$_2$(OH)$_2$ using DFT-D2 and DFT+U simultaneously. The evolution of the computed volume and lattice parameters of α-UO$_2$(OH)$_2$ as functions of the effective Hubbard parameter is shown in Figure 11.11, and the corresponding evolution of the computed U-O, O-H and O$\cdots$H bond distances is displayed in Figure 11.12.
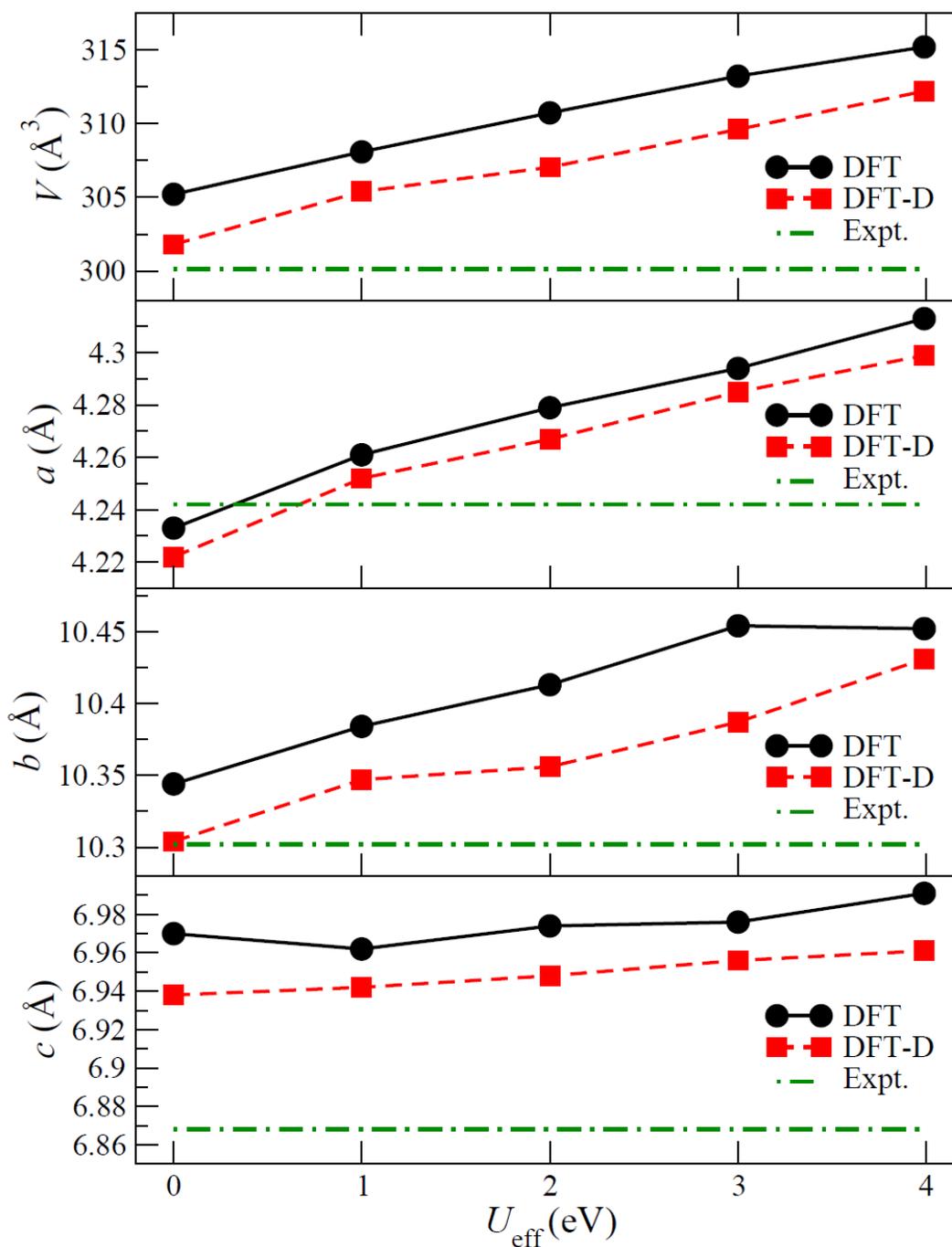
Figure 11.11. Evolution of the computed volume and lattice parameters of α-UO$_2$(OH)$_2$, as functions of the effective Hubbard parameter, U_{eff}. Calculations were carried out at the GGA+U/PBE level of theory, with (DFT-D) and without inclusion of dispersion corrections (DFT). Experimental values (Taylor and Hurst, 1971) are also reported for the sake of comparison.
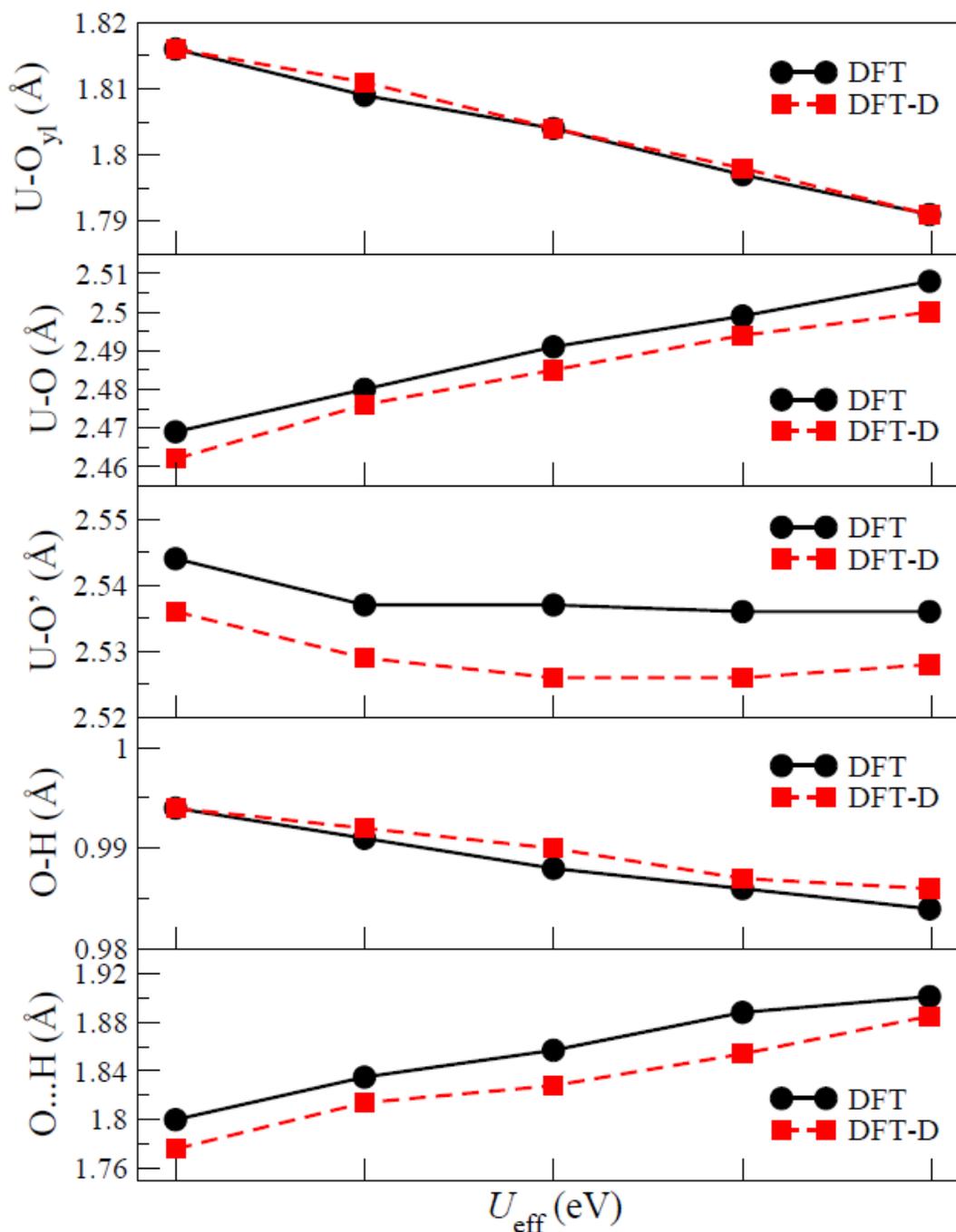
Figure 11.12. Evolution of the computed U–O, O–H and O⋯H bond distances in α-UO$_2$(OH)$_2$, as functions of the effective Hubbard parameter, U_{eff}. Calculations were carried out at the GGA+U/PBE level of theory, with (DFT-D) and without inclusion of dispersion corrections (DFT).

As shown in Figure 11.11, ramping up the +U parameter as for effect to systematically increase the in-plane lattice parameters a and b of the UO$_2$(OH)$_2$ sheets and therefore also increase the volume of the unit cell. On the other hand, including a dispersion correction term through the use of DFT-D2 slightly reduces the volume and lattice parameters relative to standard DFT results.

However, DFT-D2 calculations still overestimate the interlayer spacing along the *c* axis by about 1%, although they tend slightly improve the agreement between the computed and measured unit cell volume for $U = 0$ eV. The present DFT+U results, with or without inclusion of a dispersion correction, also suggest that no strong electron correlation term is needed and the phases of $UO_2(OH)_2$ can be investigated using standard DFT. A similar assumption was previously utilized successfully in the study of studtite and metastudtite with U(VI) metals centers (Weck, Kim, Jové-Colón, and Sassani, 2012); however, such approximation is found to be invalid for bulk UO_2 with U(IV) metal centers. As depicted in Figure 11.12, the DFT+U and DFT-D methods also have limited effect on the computed bond distances.
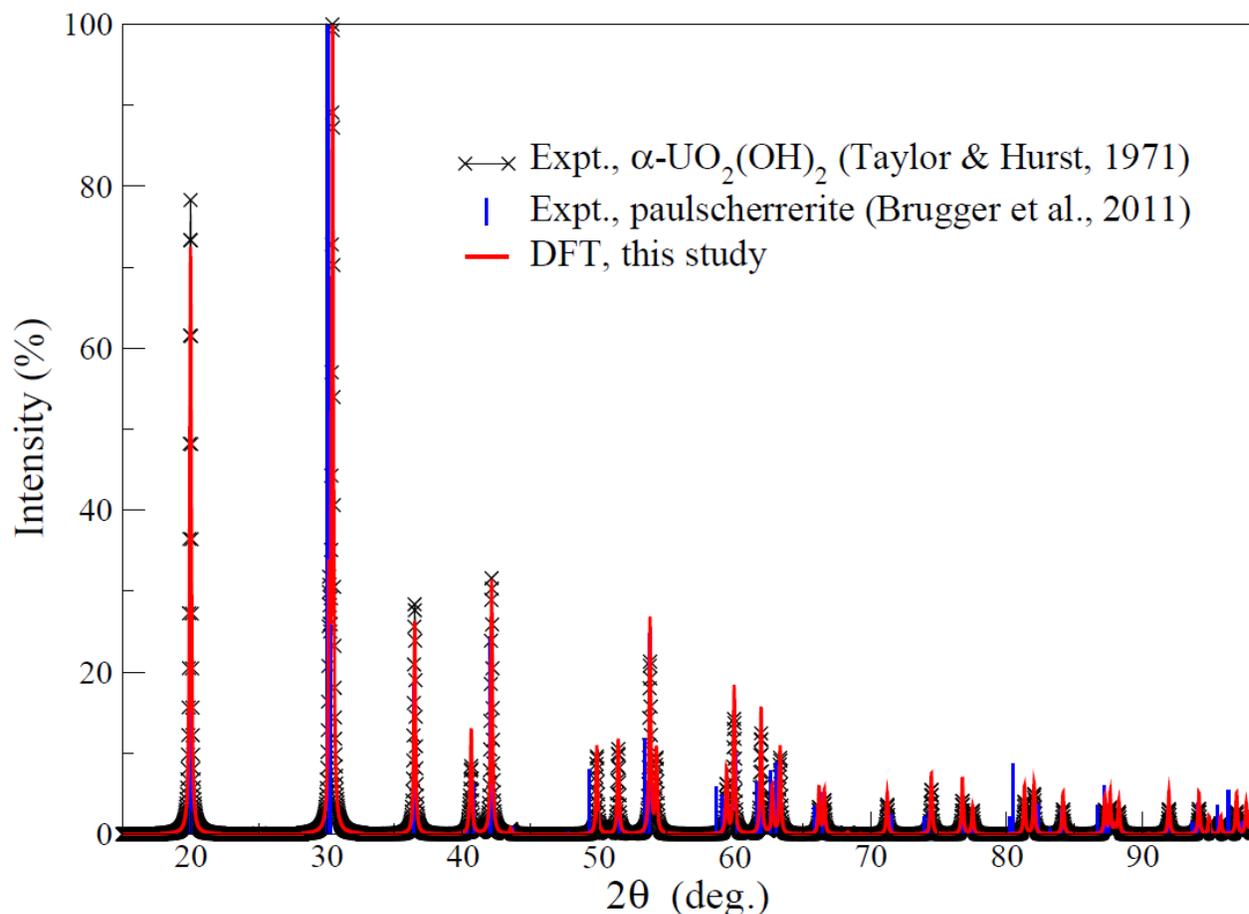
Figure 11.13. X-ray diffraction pattern of α-$UO_2(OH)_2$. The experimental powder diffraction pattern for Cu $K_{\alpha1}$ radiation (Taylor and Hurst, 1971) is represented by a black line. The diffraction pattern simulated from the structure relaxed with DFT/PBE reported in the present study is shown in red. A full-width at half-maximum (FWHM) parameter of 0.2 2θ was used in the simulation. The XRD pattern recorded for paulscherretite, the mineral form of dehydrated schoepite (Brugger et al., 2011), is also reported for the sake of comparison.

Since the DFT-D approach only slightly improves the agreement between calculated and experimental lattice parameters, without matching the interlayer spacing between α-$UO_2(OH)_2$ sheets, it was decided alternatively to use the lattice parameters determined with XRD and relax ionic positions without symmetry constraints applied. The diffraction pattern simulated from the α-$UO_2(OH)_2$ structure relaxed with DFT/PBE is shown in Figure 11.13 along with the XRD

pattern collected for Cu K$_{\alpha 1}$ radiation (Taylor and Hurst, 1971). Excellent agreement is obtained between experiment and theory. For the sake of comparison, the XRD pattern recorded for paulscherretite, the mineral form of dehydrated schoepite (Brugger et al., 2011), has also been reported. Some small peak mismatch with the results of Taylor and Hurst and our results for pure dehydrated schoepite can be seen for large 2θ angles owing to the presence of metaschoepite in the paulscherretite mineral (Brugger et al., 2011). The structures of the β, and γ phases of dehydrated schoepite have also been reoptimized using the fixed lattice parameters determined with XRD. The three resulting $UO_2(OH)_2$ phases will be used in future calculations of the thermodynamic stability and phase transitions in this compound.

12. CONCLUSIONS

Density functional theory (DFT) calculations of the thermodynamic properties of crystalline studtite, $(UO_2)O_2(H_2O)_4$, and metastudtite, $(UO_2)O_2(H_2O)_2$, were carried out within the generalized gradient approximation. Specifically, phonon analysis using density functional perturbation theory was carried out in order to derive both their isochoric and isobaric thermal properties. Further experimental work is needed to assess our theoretical predictions for these SNF corrosion phases. This methodology will be applied in a systematic way to other possible metastable corrosion phases and other NS and EBS models to expand the applicability of this data set to more realistic systems. Such an expanded data set will facilitate investigation of nuclear waste disposal in geological repositories.

In addition, polymorphism in stoichiometric dehydrated schoepite, $UO_2(OH)_2$, was investigated using computational approaches that go beyond standard DFT and include van der Waals dispersion corrections (DFT-D) and strong-electron correlation (DFT+U). As experiments conducted so far have shown, dehydrated schoepite can rapidly converted to studtite upon contact with hydrogen peroxide and moisture and might therefore play a role as a precursor to the formation of studtite on the surface of SNF. The present study shows that standard DFT is sufficient to investigate, since DFT+U and DFT-D methods have limited effect on the computed bond distances and only the DFT-D approach slightly improves the agreement between calculated and experimental lattice parameters. The three $UO_2(OH)_2$ phases optimized with standard DFT will be used in future calculations of the thermodynamic stability and phase transitions in this compound.

13. REFERENCES (Sections 11 through 12)

Amme, M. (2002). "Contrary effects of the water radiolysis product H_2O_2 upon the dissolution of nuclear fuel in natural ground water and deionized water". *Radiochimica Acta, 90*(7), 399–406.

Armstrong, C., M. Nyman, T. Shvareva, G. Sigmon, P. Burns, and A. Navrotsky (2012). "Uranyl peroxide enhanced nuclear fuel corrosion in seawater". *Proceedings of the National Academy of Sciences of the USA, 109*(6), 1874–1877.

Bannister, M. J., and J. C. Taylor (1970). "The crystal structure and anisotropic thermal expansion of β-uranyl dihydroxide, $UO_2(OH)_2$". *Acta Crystallogr., B26*, 1775–1781.

Blöchl, P. (1994). "Projector Augmented-Wave Method". *Physical Review B, 50*(24), 17953–17979.

Blöchl, P., O. Jepsen, and O. Andersen (1994). "Improved Tetrahedron Method for Brillouin-Zone Integrations". *Physical Review B, 49*(23), 16223–16233.

Brugger, J., N. Meisser, B. Etschmann, S. Ansermet, and A. Pring (2011). "Paulscherrerite from the Number 2 Workings, Mount Painter Inlier, Northern Flinders Ranges, South Australia: "Dehydrated schoepite" is a mineral after all". *American Mineralogist*, *96*, 229–240.

Buck, E., B. Hanson, J. Friese, M. Douglas, and B. McNamara (2004). "Evidence for neptunium incorporation into uranium (VI) phases". In J. Hanchar, S. Stroes Gascoyne, & L. Browning (Ed.), *28th Symposium on the Scientific Basis for Nuclear Waste Management held at the 2004 MRS Spring Meeting. 824*, pp. 133-138. San Francisco, CA: Materials Resarch Society Symposium Proceedings.

Burns, P., and K.-A. Hugues (2003). "Studtite, $[(UO_2)(O_2)(H_2O)_2](H_2O)_2$: The first structure of a peroxide mineral". *American Mineralogist, 88*(7), 1165–1168.

Burns, P., R. Ewing, and A. Navrotsky (2012). "Nuclear Fuel in a Reactor Accident". *Science, 335*(6073), 1184–1188.

Davidson, E. R. (1983). In G. Diercksen, & S. Wilson (Eds.), *Methods in Computational Molecular Physics* (Vol. 113, p. 95). New York, NY: NATO Advanced Study Institute, Series C, Plenum.

Dawson, J. K, E. Wait, K. Alcock, and D. R. Chilton (1956). "Some aspects of the system uranium trioxide-water". Journal of the Chemical Society, Sept., 3531–3540.

Draganic, I., and Z. Draganic (1971). *The Radiation Chemistry of Water.* New York, NY: Academic Press.

Dudarev, S., G. Botton, S. Savrasov, C. Humphreys, and A. Sutton (1998). "Electron-energy-loss spectra and the structural stability of nickel oxide: An LSDA+U study". *Physical Review B, 57*(3), 1505–1509.

Finch, R.J., F. C. Hawthorne, and R. C. Ewing (1998). "Structural relations among schoepite, metaschoepite, and "dehydrated schoepite". *Canadian Mineralogist*, *36*, 831–845.

Forbes, T. Z., P. Horan, T. Devine, D. McInnis, and P. C. Burns (2011). "Alteration of dehydrated schoepite and soddyite to studtite, $[(UO_2)(O_2)(H_2O)_2](H_2O)_2$". *American Mineralogist, 96,* 202–206.

Grimme, S. (2006). "Semiempirical GGA-type density functional constructed with a long-range dispersion correction", *J. Comp. Chem.*, *27*, 1787.

Hanson, B., B. McNamara, E. Buck, J. Friese, E. Jenson, K. Krupka, et al. (2005). Corrosion of commercial spent nuclear fuel. 1. Formation of studtite and metastudtite. *Radiochim. Acta, 93*(3), 159–168.

Hughes-Kubatko, K.-A., K. Helean, A. Navrotsky, and P. Burns (2003). "Stability of peroxide-containing uranyl minerals". *Science, 302*, 1191–1193.

Kresse, G., and J. Furthmüller (1996). "Efficient iterative schemes for ab initio total-energy calculations using a plane-wave basis set". *Physical Review B, 54*(16), 11169–11186.

Kresse, G., and D. Joubert (1999). "From ultrasoft pseudopotentials to the projector augmented-wave method". *Physical Review B, 59*(3), 1758–1775

McNamara, B., E. Buck, and B. Hanson (2003). Observation of studtite and metastudtite on spent fuel. In R. Finch, & D. Bullen (Ed.), *26th Symposium on the Scientific Basis for Nuclear*

Waste Management held at the 2002 MRS Fall Meeting . 757, pp. 401–406. Boston, MA : Mater. Res. Soc. Symp. Proc.

McNamara, B., B. Hanson, E. Buck, C. Soderquist (2005). Corrosion of commercial spent nuclear fuel. 2. Radiochemical analyses of metastudtite and leachates. *Radiochimica Acta, 93*(3), 169–175.

Monkhorst, H., and J. Pack (1976). "Special Points for Brillouin-Zone Integrations". *Physical Review B, 13*(12), 5188–5192

Ostanin, S., and P. Zeller, P. (2007). "Ab initio study of uranyl peroxides: Electronic factors behind the phase stability". *Physical Review B, 75*(7), 073101.

Perdew, J., and Y. Wang (1992). "Accurate and Simple Analytic Representation of the Electron-Gas Correlation-Energy". *Physical Review B, 45*(23), 13244–13249.

Perdew, J., J. Chevary, S. Vosko, K. Jackson, M. Pederson, D. Singh, et al. (1992). "Atoms, Molecules, Solids, and Surfaces - Applications of the Generalized Gradient Approximation for Exchange and Correlation". *Physical Review B, 46*(11), 6671–6687.

Perdew, J. P., K. Burke, and M. Ernzerhof (1996). "Generalized gradient approximation made simple". *Physical Review Letters*, *77*, 3865.

Roof, R. B., D. T. Cromer, and A. C. Larson (1964). "Crystal structure of uranyl dihydroxide $UO_2(OH)_2$". *Acta Crystallographica*, *17*, 710.

Sattonnay, G., C. Ardois, C. Corbel, J.-F. Lucchini, M.-F. Barthe, F. Garrido, et al. (2001). Alpha-radiolysis effects on UO2 alteration in water. *Journal of Nuclear Materials, 288*(1), 11–19.

Shuller, L., R. Ewing and U. Becker (2010). "Quantum-mechanical evaluation of Np-incorporation into studtite". *American Mineralogist, 95*(8-9), 1151–1160.

Shvareva, T. Y., J. B. Fein, and A. Navrotsky (2012). "Thermodynamic properties of uranyl minerals: constraints from calorimetry and solubility measurements". *Industrial & Engineering Chemistry Research*, *51*, 607–613

Siegel, S., H. R. Hoekstra, and E. Gebert (1972). "Structure of gamma-uranyl dihydroxide, $UO_2(OH)_2$". *Acta Crystallographica B*, *28*, 3469–3473.

Stumm, W., L. Sigg, and B. Sulzberger (1992). *Chemistry of the Solid-Water Interface: Processes at the Mineral-Water and Particle-Water Interface in Natural Systems.* New York, NY: Wiley & Sons.

Taylor, J. C. (1971). "Structure of the alpha-form of uranyl hydoxide". *Acta Crystallogr.*, *B27*, 1088.

Taylor, J. C., and H. J. Hurst (1971). "The hydrogen atom locations in the α and β forms of uranyl hydroxide". *Acta Crystallogr.*, *B27*, 2018–2022.

Taylor, J. C., J. W. Kelly and B. Downer (1972). "A Study of the β->α phase transition in $UO_2(OH)_2$ by dilatometric, microcalorimetric and X-ray diffraction techniques". *Journal of Solid State Chemistry*, *5*, 291–299.

Thompson, A., and C. Wolverton (2011). "First-principles study of noble gas impurities and defects in UO$_2$". *Physical Review B, 84*(13), 134111.

Weck, P., E. Kim, N. Balakrishnan, F. Poineau, C. Yeamans, and K. R. Czerwinski (2007). "First-principles study of single-crystal uranium mono- and dinitride". *Chemical Physics Letters, 443*(1-3), 82–86

Weck, P. F., E. Kim, C. F. Jové-Colón, and D. C. Sassani (2012). "Structures of uranyl peroxide hydrates: a first-principles study of studtite and metastudtite". *Dalton Transactions, 41*(32), 9748–9752.

Weck, P., C.-M. Gong, E. Kim, P. Thuery, and K. Czerwinski (2011). "One-dimensional uranium-organic coordination polymers: crystal and electronic structures of uranyl-diacetohydroxamate". *Dalton Transactions, 40*(22), 6007–6011.

Weck, P., E. Kim, B. Masci, P. Thuery, and K. R. Czerwinski (2010). "Density Functional Analysis of the Trigonal Uranyl Equatorial Coordination in Hexahomotrioxacalix[3]arene-based Macrocyclic Complexes". *Inorganic Chemistry, 49*(4), 1465–1470.

Wu, X., M. C. Vargas, S. Nayak, V. Lotrich, and G. Scoles (2001). "Towards extending the applicability of density functional theory to weakly bound systems". *Journal of Chemical Physics*, *115*, 8748.

14. SUMMARY AND CONCLUSIONS

The contributions presented in this report are being accomplished via a concerted effort among three different national laboratories: SNL, ANL and PNNL. This collaborative approach includes experimental work, process model development (including first-principles approaches) and model integration—both internally among developed process models and between developed process models and PA models. The main accomplishments of these activities are summarized as follows:

- Development of an idealized strategy for integrating used fuel degradation process models with PA model approaches to analyze generic disposal environments includes parametric connections/couplings needed for direct incorporation into PA models (Section 1.2.2). However, it is an ongoing task to delineate in the implementation specifics of how these process models will couple to other EBS process submodels within the PA model for generic disposal environment evaluations of the safety case. Additional more simplified coupling options are outlined that have fewer open constraints on implementation specifics and provide flexible options for incorporating additional coupling detail as needed.

- Delineation of constraints for the instant release fraction (IRF –Section 1) from the nuclear fuel implemented in two sets of distributions: (a) triangular distributions representing minimum, maximum, and mean (apex) values for LWR UF with BU at or below 50 MWd/KgU, and (b) uniform distributions as a function of BU representing instantaneous radionuclide releases for UF with BU up to 75 MWd/KgU. In future work, additional data may allow delineation of the accessible grain boundaries (and pellet fractures) from inaccessible grain boundaries (and pellet fractures) to better delineate constraints on the IRF. Currently, all grain boundaries (and pellet fractures) are considered accessible.

- Computational development and implementation of a radiolysis model (RM - Section 2) using a comprehensive set of coupled radiolysis kinetic reactions to better account for potential solution compositions to be encountered in repository environments (Wittman and Buck, 2012). Radiolytic species are generated at a rate that is based on the dose rate induced by the used fuel radiation field deposited in the water film on the fuel pellet. The current model covers the H_2O system and allows for dissolved carbonate by considering heterogeneous $CO_{2\ (aq)}$ speciation including HCO^-_3. Comparisons of modeling results are in good agreement with those reported in other studies. The model inputs are the reaction rate constants, the temperature and dose rate, the generation rates of radiolytic species, and the initial concentrations of species in the system. In these idealized systems, hydrogen peroxide is the primary oxidizing species generated in the radiolytic process. The conditional generation rate for H_2O_2 production is the primary output provided to the model for matrix degradation rate (i.e., the mixed potential model).

- Computational implementation and verification/validation of the Canadian mixed potential model for UO_2 fuel corrosion in the initial mixed potential model (MPM - Jerden et al., 2013). The objective of the MPM (Section 3) is to calculate the used fuel degradation rates for a wide range of disposal environments to provide the source term radionuclide release rates for generic repository concepts. The fuel degradation rate is

calculated for chemical and oxidative dissolution mechanisms using mixed potential theory to account for all relevant redox reactions at the fuel surface, including those involving oxidants produced by solution radiolysis. This MPM is based on the fundamental electrochemical and thermodynamic properties described by interactions at the fuel – fluid interface and captures key processes such as hydrogen oxidation and the catalysis of oxidation/reduction reactions by noble metal particles on the fuel surface (epsilon phases). If radiolytic oxidants are exhausted by reaction with hydrogen in the EBS (e.g., supplied from corrosion processes), then the degradation rate becomes controlled by UO_2 solubility constraints (chemical dissolution) and the degradation rate is affected directly by the rate of transport of uranium away from the used fuel. If oxidative dissolution is the dominant process, then the MPM directly calculates the rate of used fuel matrix degradation.

- Advanced strategies for coupling the RM and MPM into a single fuel matrix degradation (FMD) module (Section 4) for use in analyzing the matrix degradation rate (fractional and absolute) of used fuel (Section 4). Identification of parameters needed to couple the codes together are given in detail, as well as are four strategies for implementing the coupling of the two process models. Different options have advantages and disadvantages based on the extent of coding that would be required and the ease of use of the final product. The four approaches for implementing coupling are

    o   Option 1: Add radiolysis model as subroutine within mixed potential model code.

    o   Option 2: Represent radiolysis model as an analytical expression within mixed potential model code.

    o   Option 3: Provide radiolysis model results as look-up table of conditional generation values produced by running the RM over the full range of relevant conditions.

    o   Option 4: Maintain radiolysis model and mixed potential model as separate codes that call each other during a fuel degradation model run.

The last of these four options is closest to the approach to the sensitivity analyses for the MPM implemented within DAKOTA presented in Section 4.3.1. However, integration of the RM into this implementation has not been completed at this point and would require either a dynamic link library to implement, or additional coding within the DAKOTA environment to manage parameter hand-offs between the MPM and RM.

- A series of sensitivity analyses for the Mixed Potential Model (MPM) were conducted by externally-coupling the MPM Matlab code with the DAKOTA toolkit in a Microsoft Windows 7 environment. DAKOTA is an open source multilevel parallel object-oriented framework developed at Sandia National Laboratories. The DAKOTA code suite contains a large collection of algorithms to conduct optimization, uncertainty quantification (UQ), and sensitivity analysis. The external coupling uses shell scripting commands to post-process MPM output responses that are input to DAKOTA. The MPM model inputs that were varied are temperature, dose rate, and initial carbonate (CO_3^{--}) and oxygen ($O_{2\ (aq)}$) concentrations. This set of analyses contained 256 iteration calculations. The output responses that were sampled are the concentrations UO_2^{++},

UCO_3^{--}, and H_2O_2. The UO_2^{++} and UCO_3^{-} represent the total concentration of U released into the system, hence reflect the degradation rate. In these initial sensitivity analyses, the main influence in output U and H_2O_2 concentrations is the dose rate.

- A computational first-principles study of the structures of the uranyl peroxide hydrates studtite and metastudtite (Weck et al., 2012). The structures obtained from total energy calculations using density functional theory are in very good agreement with those characterized by experimental X-ray diffraction methods. Such work tests this computational tool to predict the phase stability of UO_2 corrosion products and quantify their thermodynamic properties for use with similar studies of UO_2 bulk and surface chemistry (Weck et al., 2013).

14.1 Concluding Remarks and Future Development

Our general strategy for integrating process models with each other, and within the performance assessment models, is to identify initially the major feeds among the process models (Section 4) and from the process models to performance assessment models (Section 1). For coupling into performance assessment models, our approach begins by using the existing interface connections in the PA model and progresses to adding further connections as the process models develop and become more highly coupled. The ultimate objective is to support the PA models with a single coupled process model for analyzing the fractional degradation rate of used fuel. Note that even after coupling, the radiolysis model (RM) and the mixed potential model (MPM) can still be used individually for detailed sensitivity and uncertainty analyses as well.

Currently, the MPM has been coupled with DAKOTA to perform parametric sensitivity analyses for major input variables such as radiation flux, temperature, and chemical species variability. The DAKOTA code provides one possible means of handshaking or coupling the MPM with the RM. Within any coupling implementation, identifying the essential parameters to be exchanged is the primary step. One of these is the conditional generation rate of hydrogen peroxide (G_{cond}) as a function of energy deposition in the water film on the used fuel pellet surface. The value of G_{cond} is calculated in the RM and handed off to the MPM. Within the MPM, the G_{cond} is used to calculate the spatial generation of $[H_2O_2]$ from the dose rate as affected by surface reactions with the fuel and diffusive flux of the species.

The coupling of the RM and MPM is implemented currently by running the models separately because the MPM uses time steps on the order of years, whereas the RM uses time steps on the order of seconds. An alternative to actively linking the RM and MPM (perhaps within DAKOTA) is to develop an analytic expression that determines G_{cond} for a given set of conditions. The analytic expression could be coded directly into the MPM via the MATLAB implementation, and thus run directly within the MPM. However, this simplification does not establish a true working link and the full capabilities of RM would be lost without further work. Furthermore, the determination of analytical expressions for the full ranges of environments may prove to be onerous.

Currently the only radiolytic species in the MPM is H_2O_2. Other radiolytic species will need to be added to the MPM for it to be applicable to the full range of relevant geologic and EBS environments. The radiolytic species that need to be added can be determined by sensitivity runs using the RM (which evaluates a more detailed set of compositional components) for the range

of relevant solution compositions for sites of interest. The focus of RM sensitivity runs is on radiolytically active species (for example: Cl^-, Br^-, NO_3^-, CO_3^{2-}, SO_4^{2-}) and can be used to determine concentration thresholds above which radiolytic species other than H_2O_2 significantly impact fuel oxidation.

Density functional theory (DFT) calculations of the thermodynamic properties of crystalline studtite, $(UO_2)O_2(H_2O)_4$, and metastudtite, $(UO_2)O_2(H_2O)_2$, were carried out within the generalized gradient approximation to derive both their isochoric and isobaric thermal properties. Further experimental work is needed to assess our theoretical predictions for these SNF corrosion phases. This methodology will be applied in a systematic way to other possible metastable corrosion phases and other NS and EBS models to expand the applicability of this data set to more realistic systems. In addition, polymorphism in stoichiometric dehydrated schoepite, $UO_2(OH)_2$, was investigated using computational approaches that go beyond standard DFT. The results show that standard DFT is sufficient for this system. The three $UO_2(OH)_2$ phase structures optimized with standard DFT will be used in future calculations of the thermodynamic stability and phase transitions in this compound.

For the UFD&RM process models and/or coupled modules, the primary connection into the performance assessment models is the fractional degradation rate (FDR) parameter, which is currently sampled from a distribution. This primary connection has been the focus for developing more process-based models that are able to supplant the FDR distribution by supplying that parameter directly as a result of the process model. In addition, a second connection within the PA model could be generated to represent the instant release fractions. Sampling of the IRF distributions within the PA model would be done similar to the current sampling of the FDR distribution and would describe the fast/instant release fraction radionuclides that are mobilized instantly at the time of cladding breach. The distributions for the IRF would only need to be sampled at the initiation of UF degradation for each fuel rod represented as having a breach in its cladding.

15. APPENDICES

Appendix 1

MATLAB Code for NMP Catalysis Domain Reactions

The MATLAB code for implementation of the MPM is divided into six files that must be open within the MATLAB operation folder to run the MPM. The MPM files are:

- AMP.m is a data container that holds information on simulation time steps, grid spacing, temperature, dose rate, H_2O_2 generation, species stoichiometry, saturation concentrations, diffusion coefficients, porosity, tortuosity of corrosion layer etc.
- AMP_reactSurf.m defines all surface reactions and calculates the rates of surface processes (reaction currents) and the fuel corrosion potential. This file contains all information needed for calculating rates of all surface redox reactions and is thus the heart of the MPM. It is called recursively when throughout a simulation.
- AMP_reactBulk.m defines reactions and calculates the rates of processes that occur in the space between the fuel surface and the environmental boundary at the end of the model diffusion grid (right hand boundary in Figure 6).
- AMP_main.m is a top level function that calls all the other files needed to run the MPM.
- AMP_error.m provides the status function, matrix calculations and input arguments for the MATLAB ordinary differential equation solver.
- AMP_output.m writes simulation results as space delimited text files.

The sections of code that were added to the existing MATLAB MPM to implement the NMP catalyst domain reactions are shown below. Black text is active code and green text are comments.

The following was added to the AMP.m file to allow the modeler to set the resistance between the NMP domain and the fuel matrix and to set the fractional surface coverage of NMP:

```
% Noble Metal Particle Domain Properties
    function props = NMP_prop()


% Effective resistance between fuel and NMP domains
    props.resist = 1.0e-3; % V/A   (NOT ZERO; choose something small)


% Fraction surface coverage of noble metal particles
    props.frac   = 0.01; % fraction
```

The following was added to the AMP_reactSurf file. These lines define new surface redox reactions and calculate reaction currents and the corrosion potential of the NMP domain.

```matlab
%*************************************************************************


function [rMat,dMat,oFun,dFun,eCorr,cDen] = AMP_reactSurf(T,conc,eCrG,oFlg)


% Initialize parameters
  [nCmps,~] = size(conc);
  iSS       = (AMP.valD(298)>0);
  nSS       = sum(iSS);


% Initialize current density data container
  cDen = cell(0);


% Initialize missing arguments
  if(nargin<4)
    oFlg = false;
  end
  if(nargin<3)
    eCrG = 0;
  end


% Retrieve simulation values
  F     = AMP.constF();
  R     = AMP.constR();
  datNMP = AMP.NMP_prop();


% Calculate temperature dependence factor
  dT   = (1/298-1/T)/R;


%*********************************%
% Fuel Surface Reactions         %
%*********************************%


% Initialize domain objectives
  oFun        = zeros(2,1);
```

```matlab
% Initialize reaction rates and derivatives
  rMat = zeros(nCmps,1);
  dMat = zeros(nSS,nSS);


% Initialize derivative accumulators
  dRdE1 = zeros(nSS,1);    dE1dcT1 = zeros(1,nSS);    dE1dcT2 = 1;
  dRdE2 = zeros(nSS,1);    dE2dcT1 = zeros(1,nSS);    dE2dcT2 = 1;


% Validate corrosion potentials
  if(length(eCrG)<length(oFun))
    eCorr = zeros(length(oFun),1);
  else
    eCorr = eCrG;
  end


% Calculate corrosion potential (recursive)
  if(~oFlg)
    [~,~,oFun,dFun] = AMP_reactSurf(T,conc,eCorr,true);
    dEcorr          = dFun\oFun;
    while(max(abs(oFun)) > 1e-20 && max(abs(dEcorr)) > 1e-15)
      eCorrNew        = eCorr - dEcorr;
      [~,~,oFunT,dFun] = AMP_reactSurf(T,conc,eCorrNew,true);
      if(sum(oFunT.^2) < sum(oFun.^2))
        eCorr  = eCorrNew;  oFun    = oFunT;
        dEcorr = dFun\oFun;
      else
        dEcorr = dEcorr/2;
      end
    end
  end


% Domain potentials
  eFuel = eCorr(1);
  eNMP  = eCorr(2);


% Domain surface fractions
```

```matlab
  fFrac = 1-datNMP.frac;

  pFrac =   datNMP.frac;


% Voltage difference contribution
  oFun(:)  = eNMP-eFuel;

  dFun     = [-1, 1;-1, 1];


%*********************************%
% Start NMP Domain Reactions      %
%*********************************%


% Required specifications for each surface reaction
%   kVal:  reaction rate constant (mol/m^2/s; or appropriate)
%   eNum:  number of electrons generated
%   ECTC:  electrochemical charge transfer coefficient
%   Ezro:  standard potential (Vsce)
%   sMat:  stoichiometry of reaction
%   oMat:  reaction order in concentrations


%*********************************%
% NMP 1: Reaction 7               %
% H2O2 + 2e(-) -> 2OH(-)          %
%*********************************%


% Initialize vectors
  oMat       = zeros(nCmps,1);

  sMat       = zeros(nCmps,1);


% Values unique to reaction
  kVal            =  1.2e-11*exp(6.0e4*dT); %Place holder - vary

  eNum            = -2;

  ECTC            = -0.4; %Place holder - same as UO2

  eZro            =  0.973-0.000698*(T-298); %Place holder - same as UO2


  sMat(AMP.H2O2)  = -1;


  oMat(AMP.H2O2)  =  1;
```

```matlab
% Reaction rate
  rRat  = pFrac*kVal*exp(ECTC*F/R/T.*(eNMP-eZro))*prod(conc.^oMat);


% Corrosion potential objective functions, derivatives
  if(oFlg)
    oFun(2)   = oFun(2)   - 2*datNMP.resist*F*eNum*rRat;
    dFun(2,2) = dFun(2,2) - 2*datNMP.resist*F*eNum*rRat*ECTC*F/R/T;
  end


% Current density
  cDen = [cDen,{F*eNum*rRat}];


% Reaction rates and derivatives
  if(~oFlg)
    rMat    = rMat + sMat*rRat;
    dRdc    = rRat*(oMat(iSS)./conc(iSS))';
    dRdE2   = dRdE2 + rRat*(ECTC*F/R/T)*sMat(iSS);
    dE1dcT1 = dE1dcT1 - 2*datNMP.resist*F*eNum*dRdc;
    dE1dcT2 = dE1dcT2 - 2*datNMP.resist*F*eNum*rRat*(ECTC*F/R/T);
    dMat    = dMat + sMat(iSS)*dRdc;
  end


%*********************************%
% NMP 2: Reaction 8              %
% (1/2)H2 + OH(-) -> H2O + e(-)  %
%*********************************%


% Initialize vectors
  oMat       = zeros(nCmps,1);
  sMat       = zeros(nCmps,1);


% Values unique to reaction
  kVal        =  1.0*exp(6.0e4*dT);
  eNum        =  1;
  ECTC        =  0.4;
  eZro        =  0.9-0.001900*(T-298);
```

```
  sMat(AMP.H2)  = -0.5;


  oMat(AMP.H2)  =  1;


% Reaction rate
  rRat  =  pFrac*kVal*exp(ECTC*F/R/T.*(eNMP-eZro))*prod(conc.^oMat);


% Corrosion potential objective functions, derivatives
  if(oFlg)
    oFun(2)   = oFun(2)   - 2*datNMP.resist*F*eNum*rRat;
    dFun(2,2) = dFun(2,2) - 2*datNMP.resist*F*eNum*rRat*ECTC*F/R/T;
  end


% Current density
  cDen = [cDen,{F*eNum*rRat}];


% Reaction rates and derivatives
  if(~oFlg)
    rMat     = rMat + sMat*rRat;
    dRdc     = rRat*(oMat(iSS)./conc(iSS))';
    dRdE2    = dRdE2 + rRat*(ECTC*F/R/T)*sMat(iSS);
    dE1dcT1 = dE1dcT1 - 2*datNMP.resist*F*eNum*dRdc;
    dE1dcT2 = dE1dcT2 - 2*datNMP.resist*F*eNum*rRat*(ECTC*F/R/T);
    dMat     = dMat + sMat(iSS)*dRdc;
  end


%*********************************%
% End NMP Reactions               %
%*********************************%


% Derivative cleanup
  if(~oFlg)
    dE1dc = (dE1dcT1 + dE1dcT2*dE2dcT1)/(1-dE1dcT2*dE2dcT2);
    dE2dc = (dE2dcT1 + dE2dcT2*dE1dcT1)/(1-dE2dcT2*dE1dcT2);
    dMat  = dMat + dRdE1*dE1dc;
    dMat  = dMat + dRdE2*dE2dc;
```

```
    end


%**********************************%

% End Fuel Surface Reactions      %

%**********************************%


return


%***********************************************************************
```

Definitions of MATLAB commands used in code:

classdef: begins the class definition. There are many different data types, or classes, in MATLAB. You can build matrices and arrays of floating-point and integer data, characters and strings, and logical true and false states.

static methods are associated with a class, but not with specific instances of that class. These methods do not perform operations on individual objects of a class and, therefore, do not require an instance of the class as an input argument, like ordinary methods. Static methods are useful when you do not want to first create an instance of the class before executing some code. For example, you might want to set up the MATLAB environment or use the static method to calculate data needed to create class instances.

Rvec: vector of reaction rates.

sMat: stoichiometry matrix.

oFun: objective function.

dFun: derivative function.

Ecorr: corrosion potential (Vsce)

nargin<4 returns the number of input arguments passed in the call to the currently executing function.

abs(X) returns an array Y such that each element of Y is the absolute value of the corresponding element of X.

C = min(A) returns the smallest elements along different dimensions of an array.

The ***odeset*** function lets the user adjust the integration parameters of the relevant ordinary differential equation solvers.

[tvec,Xout] = ode15s(@MPM_odefun, [0.01 tmax], X0,opts,params) integrates the system of differential equations y' = f(t,y) from time t0 to tf with initial conditions y0. Default integration parameters are replaced by property values specified in options, an argument created with the odeset function. The MATLAB ode15s solver is preferred for stiff problem types.

odefun: A MATLAB function handle that evaluates the right side of the differential equations. Provides input arguments to MATLAB ordinary differential equation solvers.

TF = isempty(A) returns logical 1 (true) if A is an empty array and logical 0 (false) otherwise. An empty array has at least one dimension of size zero.

X = reshape(A,m,n) returns the m-by-n matrix B whose elements are taken column-wise from A. An error results if A does not have m*n elements.

Appendix 2

Electrochemical Experiment Results

The results of electrochemical experiments are documented in EXCEL files in the DOE FCRD Document Management System as supporting data for the report FCRD-UFD-2013-000305. Separate files are provided for analyses conducted as a group, in most cases on the same day. The following tables summarize the electrodes and electrolytes that were used in the experiments and the analyses documented in file. Experiments were conducted using UO_2 ceramic without dopants and a representative NMP material made with Re as a surrogate for Tc referred to as NMP-W. Most experiments were conducted in electrolytes containing 1 mM NaCl that had been adjusted to a final pH of 9.5 by the addition of a dilute NaOH solution (about 1 mM NaOH); a few electrolytes were adjusted to acidic pH values using H_2SO_4. Many experiments were conducted in electrolytes with various amounts of added H_2O_2. Experiments were conducted with the as-prepared electrolytes exposed to air, or purged with argon gas or a mixture of about 3% hydrogen in helium gas referred to as regen gas.

Electrochemical analyses (Tables 2.1 through 2.7 of this appendix) included potentiodynamic (PD) sweeps, Tafel scans, linear polarization resistance (LPR) scans, electrochemical impedance spectroscopy (EIS), and cyclic voltammetry (CV) analyses. The actual data files are in VersaStudio format collected by Princeton Applied Research software and are being maintained at ANL for continued analyses. Complete results for key analyses with UO_2 and NMP alloy W are included as listed in Table 2.7 and include potentiostatic (PS) and open circuit corrosion (OC) results). Results for the individual analyses have been copied to EXCEL worksheets for convenience in storage and future use. Several experiments were commonly conducted sequentially on the same day and those data are compiled in the same EXCEL workbook. Each workbook contains a worksheet with the protocol for the suite of electrochemical experiments and information regarding the electrode and electrolyte.

Table 2.1 EXCEL files for experimental results with UO$_2$ electrodes in air

Folder and EXCEL Workbook File Name	Electrolyte				Analyses in File				
UO2/Air/Sample 1	**NaCl**	**NaOH**	**H$_2$O$_2$**	**H$_2$SO$_4$**	**LPR**	**Tafel**	**PD**	**EIS**	**CV**
UO2 1 1mM NaCl AirJuly 26 2012	1E-3 <u>M</u>	—	—	—	yes	yes	yes	yes	no
UO2 1 1mM NaCl NaOH pH 9.5 1E-4M H2O2 AirAug 15 2012	1E-3 <u>M</u>	pH 9.5	1E-4 <u>M</u>	—	yes	no	no	yes	no
UO2 1 NaOH pH 9.5 1E-2M H2O2 AirJuly 25 2012	1E-3 <u>M</u>	pH 9.5	1E-2 <u>M</u>	—	yes	yes	yes	yes	no
UO2 1 NaOH pH 9.5 1E-4M H2O2 AirJuly 21 2012	1E-3 <u>M</u>	pH 9.5	1E-4 <u>M</u>	—	yes	yes	yes	yes	no
UO2 1 NaOH pH 9.5 1E-6M H2O2 AirJuly 18 2012	1E-3 <u>M</u>	pH 9.5	1E-6 <u>M</u>	—	yes	yes	yes	yes	no
UO2 1 NaOH pH 9.5 1E-8M H2O2 AirJuly 19 2012	1E-3 <u>M</u>	pH 9.5	1E-8 <u>M</u>	—	yes	yes	yes	yes	no
UO2 1 NaOH pH 9.5 Air Oct 17 2012	1E-3 <u>M</u>	pH 9.5	—	—	yes	yes	yes	yes	no
UO2 1 NaOH pH 9.5 AirJuly 16 2012	1E-3 <u>M</u>	pH 9.5	—	—	yes	yes	yes	yes	no
UO2/Air/Sample 1/CV									
UO2 1 1mM H2O2 Air Oct 17 2012	—	—	1E-3 <u>M</u>	—	no	no	no	yes	yes
UO2 1 1mM NaCl Air Oct 9 2012	1E-3 <u>M</u>	—	—	—	no	no	no	yes	yes
UO2 1 1mM NaCl Air Oct 18 2012	1E-3 <u>M</u>	—	—	—	no	no	no	yes	yes
UO2 1 1mM NaCl NaOH pH 9.5 1E-2M H2O2 Air Oct 12 2012	1E-3 <u>M</u>	pH 9.5	1E-2 <u>M</u>	—	no	no	no	yes	yes
UO2 1 1mM NaCl NaOH pH 9.5 1E-6M H2O2 Air Oct 11 2012	1E-3 <u>M</u>	pH 9.5	1E-6 <u>M</u>	—	no	no	no	yes	yes
UO2 1 1mM NaCl NaOH pH 9.5 1E-6M H2O2 Air Oct 23 2012	1E-3 <u>M</u>	pH 9.5	1E-6 <u>M</u>	—	no	no	no	yes	yes
UO2 1 1mM NaCl NaOH pH 9.5 1E-8M H2O2 Air Oct 11 2012	1E-3 <u>M</u>	pH 9.5	1E-8 <u>M</u>	—	no	no	no	yes	yes
UO2 1 1mM NaCl NaOH pH 9.5 1E-8M H2O2 Air Oct 19 2012	1E-3 <u>M</u>	pH 9.5	1E-8 <u>M</u>	—	no	no	no	yes	yes
UO2 1 1mM NaCl NaOH pH 9.5 Air Oct 10 2012	1E-3 <u>M</u>	pH 9.5	—	—	no	no	no	yes	yes
UO2 1 1mM NaCl NaOH pH 9.5 Air Oct 18 2012	1E-3 <u>M</u>	pH 9.5	—	—	no	no	no	yes	yes
UO2 1 NaOH pH 9.5 Air Oct 17 2012	—	pH 9.5	—	—	no	no	no	yes	yes

UO2/Air//Sample 2/CV	NaCl	NaOH	H2O2	H2SO4	LPR	Tafel	PD	EIS	CV
UO2 2 1mM H2O2 Air Oct 17 2012	—	—	1E-2 M	—	no	no	no	yes	yes
UO2 2 1mM NaCl Air Oct 18 2012	1E-3 M	—		—	no	no	no	yes	yes
UO2 2 1mM NaCl NaOH pH 9.5 1E-2M H2O2 Air Oct 12 2012	1E-3 M	pH 9.5	1E-2 M	—	no	no	no	yes	yes
UO2 2 1mM NaCl NaOH pH 9.5 1E-4M H2O2 Air Oct 12 2012	1E-3 M	pH 9.5	1E-4 M	—	no	no	no	yes	yes
UO2 2 1mM NaCl NaOH pH 9.5 1E-6M H2O2 Air Oct 11 2012	1E-3 M	pH 9.5	1E-6 M	—	no	no	no	yes	yes
UO2 2 1mM NaCl NaOH pH 9.5 1E-8M H2O2 Air Oct 11 2012	1E-3 M	pH 9.5	1E-8 M	—	no	no	no	yes	yes
UO2 2 1mM NaCl NaOH pH 9.5 1E-8M H2O2 Air Oct 19 2012	1E-3 M	pH 9.5	1E-8 M	—	no	no	no	yes	yes
UO2 2 1mM NaCl NaOH pH 9.5 Air Oct 10 2012	1E-3 M	pH 9.5	—	—	no	no	no	yes	yes
UO2 2 1mM NaCl NaOH pH 9.5 Air Oct 18 2012	1E-3 M	pH 9.5	—	—	no	no	no	yes	yes
UO2 2 NaOH pH 9.5 Air Oct 17 2012	—	pH 9.5		—	no	no	no	yes	yes
UO2/Air/Sample 3/CV	NaCl	NaOH	H2O2	H2SO4	LPR	Tafel	PD	EIS	CV
UO2 3 NaOH pH 9.5 Air Oct 17 2012	—	pH 9.5		—	no	no	no	yes	yes
UO2 3 1mM H2O2 Air Oct 17 2012	—	—	1E-3 M	—	no	no	no	yes	yes
UO2 3 1mM NaCl Air Oct 18 2012	1E-3 M	—	—	—	no	no	no	yes	yes
UO2 3 1mM NaCl NaOH pH 9.5 1E-2M H2O2 Air Oct 12 2012	1E-3 M	pH 9.5	1E-2 M	—	no	no	no	yes	yes
UO2 3 1mM NaCl NaOH pH 9.5 1E-4M H2O2 Air Oct 12 2012	1E-3 M	pH 9.5	1E-4 M	—	no	no	no	yes	yes
UO2 3 1mM NaCl NaOH pH 9.5 1E-6M H2O2 Air Oct 11 2012	1E-3 M	pH 9.5	1E-6 M	—	no	no	no	yes	yes
UO2 3 1mM NaCl NaOH pH 9.5 1E-8M H2O2 Air Oct 11 2012	1E-3 M	pH 9.5	1E-8 M	—	no	no	no	yes	yes
UO2 3 1mM NaCl NaOH pH 9.5 1E-8M H2O2 Air Oct 19 2012	1E-3 M	pH 9.5	1E-8 M	—	no	no	no	yes	yes
UO2 3 1mM NaCl NaOH pH 9.5 Air Oct 10 2012	1E-3 M	pH 9.5	—	—	no	no	no	yes	yes
UO2 3 1mM NaCl NaOH pH 9.5 Air Oct 18 2012	1E-3 M	pH 9.5	—	—	no	no	no	yes	yes

Table 2.2 EXCEL files for experimental results with UO$_2$ electrodes in electrolyte purged with argon gas

UO2/Argon	NaCl	NaOH	H2O2	H2SO4	LPR	Tafel	PD	EIS	CV
UO2 1 1mM NaCl Argon July 31 2012	1E-3 M	—	—	—	yes	yes	yes	yes	no
UO2#1 NaOH pH 9.5 1E-2M H2O2 Argon June 28 2012	1E-3 M	pH 9.5	1E-2 M	—	yes	yes	yes	yes	no
UO2#1 NaOH pH 9.5 1E-4M H2O2 Argon July 11 2012	1E-3 M	pH 9.5	1E-4 M	—	yes	yes	yes	yes	no
UO2#1 NaOH pH 9.5 1E-6M H2O2 Argon June 26 2012	1E-3 M	pH 9.5	1E-6 M	—	yes	yes	yes	yes	no
UO2#1 NaOH pH 9.5 1E-8M H2O2 Argon July 25 2012	1E-3 M	pH 9.5	1E-8 M	—	yes	yes	yes	yes	no
UO2#1 NaOH pH 9.5 Argon July 13 2012	1E-3 M	pH 9.5	—	—	yes	yes	yes	yes	no
UO2/Argon/CV	**NaCl**	**NaOH**	**H2O2**	**H2SO4**	**LPR**	**Tafel**	**PD**	**EIS**	**CV**
UO2 1 1mM H2O2 Argon Oct 25 2012	—	—	1E-3 M	—	no	no	no	yes	yes
UO2 1 1mM NaCl Argon Oct 23 2012	1E-3 M	—	—	—	no	no	no	yes	yes
UO2 1 1mM NaCl NaOH pH 9.5 1E-2M H2O2 Argon Oct 30 2012	1E-3 M	pH 9.5	1E-2 M	—	no	no	no	yes	yes
UO2 1 1mM NaCl NaOH pH 9.5 1E-4M H2O2 Argon Oct 29 2012	1E-3 M	pH 9.5	1E-4 M	—	no	no	no	yes	yes
UO2 1 1mM NaCl NaOH pH 9.5 1E-6M H2O2 Argon Oct 29 2012	1E-3 M	pH 9.5	1E-6 M	—	no	no	no	yes	yes
UO2 1 1mM NaCl NaOH pH 9.5 1E-8M H2O2 Argon Oct 25 2012	1E-3 M	pH 9.5	1E-8 M	—	no	no	no	yes	yes
UO2 1 1mM NaCl NaOH pH 9.5 Argon Oct 24 2012	1E-3 M	pH 9.5	—	—	no	no	no	yes	yes
UO2 1 NaOH pH 9.5 Argon Oct 24 2012	—	pH 9.5	—	—	no	no	no	yes	yes

Table 2.3 EXCEL files for experimental results with UO$_2$ electrodes in electrolyte purged with regen gas

UO2/Regen	NaCl	NaOH	H2O2	H2SO4	LPR	Tafel	PD	EIS	CV
UO2#1 1mM NaCl Regen July 27 2012	1E-3 M	—	—	—	yes	yes	yes	yes	no
UO2#1 NaOH pH 9.5 1E-2M H2O2 Regen July 12 2012	1E-3 M	pH 9.5	1E-2 M	—	yes	yes	yes	yes	no
UO2#1 NaOH pH 9.5 1E-4M H2O2 Regen July 5 2012	1E-3 M	pH 9.5	1E-4 M	—	yes	yes	yes	yes	no
UO2#1 NaOH pH 9.5 1E-6M H2O2 Regen July 2 2012	1E-3 M	pH 9.5	1E-6 M	—	yes	yes	yes	yes	no
UO2#1 NaOH pH 9.5 1E-8M H2O2 Regen July 20 2012	1E-3 M	pH 9.5	1E-8 M	—	yes	yes	yes	yes	no
UO2#1 NaOH pH 9.5 Regen July 17 2012	1E-3 M	pH 9.5	—	—	yes	yes	yes	yes	no
UO2/Regen/CV	**NaCl**	**NaOH**	**H2O2**	**H2SO4**	**LPR**	**Tafel**	**PD**	**EIS**	**CV**
UO2# NaOH pH 9.5 Regen Nov 1 2012	—	pH 9.5	—	—	no	no	no	yes	yes
UO2#1 1mM H2O2 Regen Nov 5 2012	—	—	1E-3 M	—	no	no	no	yes	yes
UO2#1 1mM NaCl NaOH pH 9.5 Regen Nov 2 2012	1E-3 M	pH 9.5	—	—	no	no	no	yes	yes
UO2#1 1mM NaCl NaOH pH 9.5 1E-2M H2O2 Regen Nov 9 2012	1E-3 M	pH 9.5	1E-2 M	—	no	no	no	yes	yes
UO2#1 1mM NaCl NaOH pH 9.5 1E-4M H2O2 Regen Nov 8 2012	1E-3 M	pH 9.5	1E-4 M	—	no	no	no	yes	yes
UO2#1 1mM NaCl NaOH pH 9.5 1E-6M H2O2 Regen Nov 7 2012	1E-3 M	pH 9.5	1E-6 M	—	no	no	no	yes	yes
UO2#1 1mM NaCl NaOH pH 9.5 1E-8M H2O2 Regen Nov 6 2012	1E-3 M	pH 9.5	1E-8 M	—	no	no	no	yes	yes
UO2#1 1mM NaCl Regen Oct 31 2012	1E-3 M	—	—	—	no	no	no	yes	yes

Table 2.4 EXCEL files for experimental results with NMP-W electrode in air

NMPW Alloy/Air	NaCl	NaOH	H2O2	H2SO4	LPR	Tafel	PD	EIS	CV
NMP-W 1mM H2O2 Air Mar 16 2012	—	—	1E-3 M	—	yes	yes	yes	yes	no
NMP-W 1mM NaCl 0.025M H2SO4 Air May 14 2012	1E-3 M	pH 9.5	1E-2 M	—	yes	yes	yes	yes	no
NMP-W 1mM NaCl Air Apr 22 2012	1E-3 M	—	—	—	yes	yes	yes	yes	no
NMP-W 1mM NaCl Air July 17 2012	1E-3 M	—	—	—	yes	yes	yes	yes	no
NMP-W 1mM NaCl NaOH pH 9.5 1E-2M H2O2 Air July 26 2012	1E-3 M	pH 9.5	1E-2 M	—	yes	yes	yes	yes	no
NMP-W 1mM NaCl NaOH pH 9.5 1E-2M H2O2 Air May 4 2012	1E-3 M	pH 9.5	1E-2 M	—	yes	yes	yes	yes	no
NMP-W 1mM NaCl NaOH pH 9.5 1E-2M H2O2 Air May 18 2012	1E-3 M	pH 9.5	1E-2 M	—	yes	yes	yes	yes	no
NMP-W 1mM NaCl NaOH pH 9.5 1E-4M H2O2 Air July 20 2012	1E-3 M	pH 9.5	1E-4 M	—	yes	yes	yes	yes	no
NMP-W 1mM NaCl NaOH pH 9.5 1E-4M H2O2 Air May 2 2012	1E-3 M	pH 9.5	1E-4 M	—	yes	yes	yes	yes	no
NMP-W 1mM NaCl NaOH pH 9.5 1E-4M H2O2 H2SO4 pH 3 Air May 9 2012	1E-3 M	pH 9.5	1E-4 M	1E-4 M	yes	yes	yes	yes	no
NMP-W 1mM NaCl NaOH pH 9.5 1E-6M H2O2 Air Apr 25 2012	1E-3 M	pH 9.5	1E-6 M	—	yes	yes	yes	yes	no
NMP-W 1mM NaCl NaOH pH 9.5 1E-6M H2O2 Air July 19 2012	1E-3 M	pH 9.5	1E-6 M	—	yes	yes	yes	yes	no
NMP-W 1mM NaCl NaOH pH 9.5 1E-8M H2O2 Air July 27 2012	1E-3 M	pH 9.5	1E-8 M	—	yes	yes	yes	yes	no
NMP-W 1mM NaCl NaOH pH 9.5 Air Apr 24 2012	1E-3 M	pH 9.5	—	—	yes	yes	yes	yes	no
NMP-W 1mM NaCl NaOH pH 9.5Air July 18 2012	1E-3 M	pH 9.5	—	—	yes	yes	yes	yes	no
NMPW Alloy/Air/CV									
NMP-W 1mM H2O2 Air May 16 2012	—	—	1E-3 M	—	no	no	no	yes	yes
NMP-W 1mM NaCl Air April 17 2012	1E-3 M	—	—	—	no	no	no	yes	yes
NMP-W 1mM NaCl Air Oct 18 2012	1E-3 M	—	—	—	no	no	no	yes	yes
NMP-W 1mM NaCl NaOH pH 9.5 1E-2M H2O2 Air Oct 12 2012	1E-3 M	pH 9.5	1E-2 M	—	no	no	no	yes	yes
NMP-W 1mM NaCl NaOH pH 9.5 1E-4M H2O2 then H2SO4 pH 3 Air May 11 2012	1E-3 M	pH 9.5	1E-4 M	1E-4 M	no	no	no	yes	yes

NMP-W 1mM NaCl NaOH pH 9.5 1E-6M H2O2 Air Oct 11 2012	1E-3 M	pH 9.5	1E-6 M	—	no	no	no	yes	yes
NMP-W 1mM NaCl NaOH pH 9.5 1E-6M H2O2 Air Oct 23 2012	1E-3 M	pH 9.5	1E-6 M	—	no	no	no	yes	yes
NMP-W 1mM NaCl NaOH pH 9.5 1E-8M H2O2 Air Oct 19 2012	1E-3 M	pH 9.5	1E-8 M	—	no	no	no	yes	yes
NMP-W 1mM NaCl NaOH pH 9.5 Air Oct 18 2012	1E-3 M	pH 9.5	—	—	no	no	no	yes	yes
NMP-W NaOH pH 9.5 1E-2M H2O2 Air May 18 2012	—	pH 9.5	1E-2 M	—	no	no	no	yes	yes
NMP-W NaOH pH 9.5 Air Oct 17 2012	—	pH 9.5	—	—	no	no	no	yes	yes
NMP-W 1mM NaCl NaOH pH 9.5 1E-4M H2O2 Air Oct 12 2012	1E-3 M	pH 9.5	1E-4 M	—	no	no	no	yes	yes
NMP-W 1mM H2O2 0.025M H2SO4 Air May 14 2012	—	—	1E-3 M	2.5E-2 M	no	no	no	yes	yes

Table 2.5 EXCEL files for experimental results with NMP-W electrode in electrolyte purged with argon gas

NMPW Alloy/Argon/CV	NaCl	NaOH	H2O2	H2SO4	LPR	Tafel	PD	EIS	CV
NMP-W 1mM H2O2 Argon Oct 25 2012	1E-3 M	—	—	—	no	no	no	yes	yes
NMP-W 1mM NaCl NaOH pH 9.5 Argon Oct 24 2012	—	pH 9.5	1E-2 M	—	no	no	no	yes	yes
NMP-W 1mM NaCl NaOH pH 9.5 1E-2M H2O2 Argon Oct 30 2012	1E-3 M	pH 9.5	1E-2 M	—	no	no	no	yes	yes
NMP-W 1mM NaCl NaOH pH 9.5 1E-4M H2O2 Argon Oct 29 2012	1E-3 M	pH 9.5	1E-4 M	—	no	no	no	yes	yes
NMP-W 1mM NaCl NaOH pH 9.5 1E-6M H2O2 Argon Oct 29 2012	1E-3 M	pH 9.5	1E-6 M	—	no	no	no	yes	yes
NMP-W 1mM NaCl NaOH pH 9.5 1E-8M H2O2 Argon Oct 25 2012	1E-3 M	pH 9.5	1E-8 M	—	no	no	no	yes	yes

Table 2.6 EXCEL files for experimental results with NMP-W electrode in electrolyte purged with regen gas

NMPW Alloy/Regen	NaCl	NaOH	H2O2	H2SO4	LPR	Tafel	PD	EIS	CV
NMP-W 0.025M H2SO4 1mM H2O2 Regen Mar 15 2012	1E-3 <u>M</u>	—	—	2.5E-2 <u>M</u>	yes	yes	yes	yes	no
NMP-W 1mM H2O2 Regen Mar 17 2012	—	—	1E-2 <u>M</u>	—	yes	yes	yes	yes	no
NMP-W 1mM NaCl NaOH pH 9.5 1E-6M H2O2 Regen Aug 1 2012	1E-3 <u>M</u>	pH 9.5	1E-6 <u>M</u>	—	yes	yes	yes	yes	no
NMP-W 1mM NaCl NaOH pH 9.5 1E-8M H2O2 Regen Aug 3 2012	1E-3 <u>M</u>	pH 9.5	1E-8 <u>M</u>	—	yes	yes	yes	yes	no
NMP-W 1mM NaCl NaOH pH 9.5l Regen Apr 2 2012	1E-3 <u>M</u>	pH 9.5	—	—	yes	yes	yes	yes	no
NMP-W 1mM NaCl NaOH pH 9.5 1E-2M H2O2 Regen Aug 6 2012	1E-3 <u>M</u>	pH 9.5	1E-2 <u>M</u>	—	yes	yes	yes	yes	no
NMP-W 1mM NaCl NaOH pH 9.5 1E-2M H2O2 Regen May 7 2012	1E-3 <u>M</u>	pH 9.5	1E-2 <u>M</u>	—	yes	yes	yes	yes	no
NMP-W 1mM NaCl NaOH pH 9.5 1E-2M H2O2 Regen May 20 2012	1E-3 <u>M</u>	pH 9.5	1E-2 <u>M</u>	—	yes	yes	yes	yes	no
NMP-W 1mM NaCl NaOH pH 9.5 1E-4M H2O2 Regen Aug 2 2012	1E-3 <u>M</u>	pH 9.5	1E-4 <u>M</u>	—	yes	yes	yes	yes	no
NMP-W 1mM NaCl NaOH pH 9.5 1E-4M H2O2 Regen May 3 2012	1E-3 <u>M</u>	pH 9.5	1E-4 <u>M</u>	—	yes	yes	yes	yes	no
NMP-W 1mM NaCl NaOH pH 9.5 1E-4M H2O2H2SO4 pH 3 Regen May 10 2012	1E-3 <u>M</u>	pH 9.5	1E-4 <u>M</u>	—	yes	yes	yes	yes	no
NMP-W 1mM NaCl NaOH pH 9.5 1E-6M H2O2 Regen Apr 30 2012	1E-3 <u>M</u>	pH 9.5	1E-6 <u>M</u>	—	yes	yes	yes	yes	no
NMP-W 1mM NaCl NaOH pH 9.5 Regen July 25 2012	1E-3 <u>M</u>	pH 9.5	—	—	yes	yes	yes	yes	no
NMP-W 1mM NaCl NaOH pH 9.5 Regen Mar16 2012	1E-3 <u>M</u>	pH 9.5	—	—	yes	yes	yes	yes	no
NMP-W 1mM NaCl Regen Apr 23 2012	1E-3 <u>M</u>	—	—	—	yes	yes	yes	yes	no
NMP-W 1mM NaCl Regen July 31 2012	1E-3 <u>M</u>	—	—	—	yes	yes	yes	yes	no
NMPW Alloy/Regen/CV	NaCl	NaOH	H2O2	H2SO4	LPR	Tafel	PD	EIS	CV
NMP-W 1mM H2O2 Regen Nov 5 2012	—	—	1E-3 <u>M</u>	—	no	no	no	yes	yes
NMP-W 1mM NaCl NaOH pH 9.5 1E-2M H2O2 Regen Nov 9 2012	—	pH 9.5	1E-2 <u>M</u>	—	no	no	no	yes	yes
NMP-W 1mM NaCl NaOH pH 9.5 1E-4M H2O2 Regen Nov 8 2012	1E-3 <u>M</u>	pH 9.5	1E-4 <u>M</u>	—	no	no	no	yes	yes

NMP-W 1mM NaCl NaOH pH 9.5 1E-6M H2O2 Regen Nov 7 2012	1E-3 M	pH 9.5	1E-6 M	—	no	no	no	yes	yes
NMP-W 1mM NaCl NaOH pH 9.5 1E-8M H2O2 Regen Nov 6 2012	1E-3 M	pH 9.5	1E-8 M	—	no	no	no	yes	yes
NMP-W 1mM NaCl NaOH pH 9.5 Regen Nov 2 2012	1E-3 M	pH 9.5	—	—	no	no	no	yes	yes
NMP-W Alloy 0.025M H2SO4 1mM H2O2 Regen May 15 2012	—	—	1E-3 M	—	no	no	no	yes	yes
NMP-W Alloy 1mM H2O2 Regen May 16 2012	—	—	1E-3 M	—	no	no	no	yes	yes
NMP-W Alloy 1mM NaCl Regen Apr 17 2012	1E-3 M	—		—	no	no	no	yes	yes
NMP-W Alloy 1mM NaCl NaOH pH 9.5 1E-2M H2O2 Regen Apr 6 2012	1E-3 M	pH 9.5	1E-2 M	—	no	no	no	yes	yes
NMP-W Alloy 1mM NaCl NaOH pH 9.5 1E-2M H2O2 Regen May 22 2012	1E-3 M	pH 9.5	1E-2 M	—	no	no	no	yes	yes
NMP-W Alloy 1mM NaCl NaOH pH 9.5 H2SO4 pH3 1E-4M H2O2 Regen May 11 2012	1E-3 M	pH 9.5	1E-4 M	1E-3 M	no	no	no	yes	yes
NMP-W Alloy 1mM NaCl NaOH pH 9.5 Regen Apr 18 2012	1E-3 M	pH 9.5	—	—	no	no	no	yes	yes

Table 2.7 EXCEL files with collection data

UO2/UO2 VersaStudio	NaCl	NaOH	H2O2	OC	LPR	Tafel	PD	PS	EIS
PS UO2 E-2	1E-3 M	pH 9.5	1E-2 M	yes	no	no	no	yes	yes
UO2 H2O2	1E-3 M	pH 9.5	various	yes	yes	yes	yes	yes	yes
UO2 NaCl NaOH	1E-3 M	pH 9.5	No	yes	yes	yes	yes	yes	yes
W H2O2	1E-3 M	pH 9.5	various	yes	yes	yes	yes	yes	yes
W NaCl NaOH	1E-3 M	pH 9.5	No	yes	yes	yes	yes	yes	yes